Characterization and application of 3D silicon microdosimeters

Andreas Tefre Samnøy

Thesis for the degree of Philosophiae Doctor (PhD)
University of Bergen, Norway
2020

UNIVERSITY OF BERGEN

Characterization and application of 3D silicon microdosimeters

Andreas Tefre Samnøy

Thesis for the degree of Philosophiae Doctor (PhD)
at the University of Bergen

Date of defense: 11.12.2020

Year: 2020

Title: Characterization and application of 3D silicon microdosimeters

Name: Andreas Tefre Samnøy

Print: Skipnes Kommunikasjon / University of Bergen

Scientific environment

The work presented here was funded by the University of Bergen and supervised by Professor Dieter Röhrich and co-supervisor Kristian Ytre-Hauge. The research project has been a collaboration with the Centre for Medical Radiation Physics (CMRP) at the University of Wollongong in Australia, directed by Distinguished Professor Anatoly Rosenfeld who proposed and patented the microdosimeters used in this thesis. The project also collaborated with SINTE in Oslo, Norway, who developed and produced the microdosimeters, and were funded by the Research Council of Norway via the NANO2021 program.

The work was aided by the Biophysics and Medical Physics group at the University of Oslo, and the staff at the ion beam at the Australian Nuclear Science and Technology Organisation (ANSTO).

Acknowledgements

This thesis could not have been written without the help and support of the people around me for the last years. I would first like to thank my supervisors Professor Dieter Röhrich and Kristian Ytre-Hauge for giving me the opportunity to come back to the university and start PhD in medical physics. Dieter supervised me through a master’s degree 10 years ago, and although I did not immediately want to start a PhD, he welcomed me back after a few years in the oil industry. Dieters great understanding in radiation and detector physics has been invaluable to me during my work.

I would like to thank Kristian for always questioning my thoughts and pushing me forwards. This was instrumental for my understanding and for me to finish up my work. I am also grateful that your door was always open for discussing everything from physics to hunting and complaints I might have had at the moment. I would also like to say that I am sorry for all the times I did not knock before I barged in your door.

Thanks to Professor Anatoly Rosenfeld and Linh Tran, who are the true experts in silicon microdosimetry, for helping me understanding the field and for welcoming me during my stay at Wollongong in Australia. A special thanks to Linh for organizing the beamtime at ANSTO. I am also very grateful to the staff at ANSTO who worked overtime to produce the parts necessary for fitting our equipment in the beamline. Thanks to Zeljko Pastuovic for the warm welcome at ANSTO and your never-ending enthusiasm for all the questions I had while I was there.

Thanks to Marco Povoli and Angela Kok for welcoming me during my stay at SINTEF and for your patients with my questions. Your insights and suggestions were invaluable, and my only regret is that I did involve you more than I did.

Thanks to Professor Eirik Malinen for the help during the experiments at OCL and for all the support while writing our article.

To all my colleagues at the nuclear and medical physics group who made it enjoyable to come to work every day, thank you. I have enjoyed all our pointless discussions during our hour-long lunches. Thanks to my roommate Lukas for your open mind and in humoring me in all my complaints and strange topics of conversation.

To my family who supported me through this work. Thanks to my parents, Kari and Steinar, and Sigrid's parents, Anne and Johan, for the support and for helping with the care of our children when I was traveling. I would also like to thank my children, Eivind and Vårin, for reminding me that there are more important things in life than work. And most importantly, I would like to thank my loving wife, Sigrid, for all the support and patients you have given me through these years. I could not have done this without you by my side.

Abstract

The effect of ionizing radiation on biological matter differs significantly between the various types of radiation. For the same amount of absorbed energy, some forms of radiation are much more effective in inducing biological response than others, having a higher *radiation quality*. Not only does the radiation quality differ between the particle species, but it also depends on the particles' energy. Microdosimetry is an experimental and theoretical scientific field where the energy deposition in micrometric volumes is used to quantify the radiation quality. The strength of microdosimetry is that although the underlying physics is complex, the radiation quality is defined in principally simple terms which are quantifiable and measurable and can provide input to radiobiological models

At the heart of the microdosimetry is the detector, or *microdosimeter*, which is used to measure energy depositions. For 75 years the tissue equivalent proportional counter (TEPC) has been the gold standard for microdosimetry, but over the last two decades silicon detectors have been developed as an alternative. The main objective of this work has been to characterize and test a new generation of silicon microdosimeters with five slightly different designs.

Electrical characteristics were measured and the microdosimeters have been tested with several soft photon sources and an ^{241}Am alpha source. The charge collection efficiency (CCE) was determined by comparing the results to that of a commercial PIN diode for spectroscopy. One of the microdosimeters was investigated in a microbeam with the ion beam induced charge collection (IBICC) technique with ^{12}C ions, revealing the sensitivity of the different parts of the microdosimeter and produced radiation damage effects. A microdosimeter was also used to measure the energy deposition at all depth of an absorber in a 15 MeV proton beamline used for radiobiological experiments. The results were compared to both a MC simulation and the dose measurements from a commercial ionization chamber (IC). The measurements in the proton beam were conducted to further characterize the microdosimeter and was used as a microdosimetric characterization of the beamline.

Since the silicon microdosimeters are not tissue equivalent (TE) the measurements from the 15 MeV beamline were corrected with a novel tissue correction function presented here and compared to a previously used method from literature.

The measurements showed that the silicon microdosimeters are fully depleted at 5 V with a dark current of approximately 0.1 nA and capacitance below 80 pF. Photon sources between 8 and 60 keV showed 100% CCE for all microdosimeters. The alpha particles produced spectra with a peak at 1445 keV, which were in line with MC simulation. The spectra also had a very large fraction of events below 100 keV and a low amplitude constant band of events between 100 and 1200 keV not visible in the simulations. The IBICC experiment showed homogeneous charge collection at the centre of the SVs but they had a clear sensitivity gradient at the edges giving rise to lower energy events from the monoenergetic beam. The high LET ^{12}C microbeam produced surface damage, where charge in the oxide layer made the volume between the SVs sensitive. The effects from the surface damage were reduced effectively by increasing the bias voltage from 5 to 15 V. In the 15 MeV proton beamline, the energy deposition spectra at all depths of the polyamide absorber matched well with the MC simulations apart from a slight shift towards higher energy depositions at the entrance. MC simulations of the proton beam showed that the tissue correction function had a maximum error of 1.1% while previously used methods gave up to 15% error. The comparison with the IC indicated that the tissue corrected microdosimeter reproduced the relative depth dose profile well, although the comparison suffered from slightly different measurement positions with respect to the absorbers. The measured tissue corrected dose-mean lineal energy, $\overline{y_D}$, was between 8 and 35 keV/µm and matched well with simulations of a tissue composed microdosimeter except for a 12% difference at the entrance.

An alternative type of microdosimeter is also presented and discussed, where a stack of high granularity pixel sensors can be used to track all the particles entering and generated within the microdosimeter. The specifications from the ALPIDE detector with a 5 µm resolution along the two dimensions of the sensor plane are used in the discussion. 12 µm resolution can be achieved in the depth direction by stacking the sensors densely but would be reduced by inserting tissue equivalent material between the sensors to make the detector more biological relevant. The ALPIDE can coarsely measure the energy deposition in each layer by allowing clusters of pixels to fire when struck by a particle. A design with the current ALPIDE detector should be able track primary particles entering the detector well but would have issues with tracking most of the secondary electrons as they would need at least 50 keV to be separable from the primary particle. Further studies of such a microdosimeter should be conducted through MC simulations to determine the necessary specifications for such a tracking microdosimeter.

In summary, the measurements with the microdosimeters agrees well with simulations and can be an alternative to TEPCs. The microdosimeters small size makes them excellent for measurements at various depths in therapeutic beamlines such that the *relative biological effectiveness* (RBE) can be assessed. The microdosimeters are inexpensive to mass produce and they are easy to operate, this makes them readily available for use in conjunction with research, radiation therapy and radiation protection. The work presented here can support other users of the microdosimeter when planning, measuring and analysing results. This work also aids in the development of new and better microdosimeters.

List of abbreviations

ALICE	A Large Ion Collider Experiment (CERN experiment)
ATLAS	A Toroidal LHC ApparatuS (CERN experiment)
ALPIDE	ALice Pixel DEtector
BNCT	Boron Neutron Capture Therapy
BP	Bragg Peak
CoG	Center of Gravity
CPU	Central Processing Unit
CMRP	Centre of Medical Radiation Physics
CCE	Charge Collection Efficiency
CSP	Charge Sensitive Preamplifier
CT	Computer Tomography
CAD	Computer-Aided Design
CERN	Conseil Européen pour la Recherche Nucléaire (European Organization for Nuclear Research)
CSDA	Continuous slowing down approximation
DAQ	Data acquisition
DICOM	Digital Imaging and Communications in Medicine
DDF	Distal Dose Fall off
DSB	Double Strand Breaks
EM	Electromagnetic
GATE	Geant4 Application for Emission Tomography
Geant	GEometry ANd Tracking (MC simulation toolkit)
GR	Guard Ring
HSG	human salivary grand
HVL	Høgskulen på Vestlandet (Western Norway University of Applied Sciences)
ITS	Inner Tracking System
IAEA	International Atomic Energy Agency
ICRU	International Commission on Radiation Units and Measurements
IC	Ionization Chamber
LET	Linear Energy Transfer
LQ	Linear Quadratic
MK(M)	Microdosimetric-Kinetic (Model)
MIP	Minimum Ionizing Particle
MAPS	Monolithic Active Pixel Sensor
MC	Monte Carlo
NIST	National Institute of Standards and Technology
OCL	Oslo Cyclotron Laboratory

PMMA	Poly(methyl methacrylate)
PCB	Printed Circuit Board
QA	Quality Assurance
RBE	Relative Biological Effectiveness
SEM	Scanning Electron Microscope
SV	Sensitive Volume
SNR	Signal to Noise Ratio
SOI	Silicon On Insulator
SSB	Single Strand Breaks
SOBP	Spread out Bragg peak
TDRA	Theory of Dual Radiation Action
TE	Tissue Equivalent
TEPC	Tissue Equivalent Proportional Counter
UoW	University of Wollongong
WER	Water Equivalent Ratio
WET	Water Equivalent Thickness

Contents

Scientific environment i

Acknowledgements ii

Abstract iv

List of abbreviations vii

Contents ix

1. Introduction 1

1.1 Objectives and outline 3

2. Microdosimetry 5

2.1 Radiation interaction with matter 7

2.2 Regional microdosimetry 12

2.3 Microdosimetric quantities 13

2.4 Microdosimeter design criteria 16

2.5 Relative variance in single event distributions 19

2.6 Tissue Equvalent Proportional Counter (TEPC) 22

2.7 Biological models 29
2.7.1 Linear Quadratic model 29
2.7.2 Theory of dual radiation action (TDRA) 32
2.7.3 Microdosimetric-kinetic model (MKM) 34
2.7.4 Local Effect Model (LEM) 37

3. Silicon detectors 39

3.1 Properties of silicon detectors 39
3.1.1 Doping 41
3.1.2 PN-junction 41

3.2 Read out electronics 44

3.3 Silicon detectors for microdosimetry 46
3.3.1 Signal formation 46
3.3.2 Tissue Equivalence 47

3.3.3 Definition of the sensitive volume (SV) 50

3.3.4 The 3D SOI "mushroom" microdosimeter 53

3.4 ALPIDE *57*

4. Monte Carlo simulation 59

4.1 GATE and Geant4 simulations tools *59*

4.2 GATE model of the 3D SOI "mushroom" microdosimeter *61*

5. Basic characterization of microdosimeters 65

5.1 Setup & Method *66*

5.1.1 I-V and C-V 66

5.1.2 Readout electronics for measurements of single event energy deposition 66

5.1.3 Soft photon measurements 67

5.1.4 Alpha measurements 70

5.2 Results *72*

5.2.1 I-V and C-V characteristics 72

5.2.2 Soft Photons 74

5.2.3 Alpha measurements 81

5.3 Discussion *89*

5.4 Summary *91*

6. Ion beam induced charge collection for 3D microdosimeter 93

6.1 Setup & Method *94*

6.2 Results *95*

6.2.1 Large area scan 95

6.2.2 Medium area scan 98

6.2.3 Small area scan 101

6.2.4 Radiation damage 104

6.2.5 Single Sensitive Volune 107

6.3 Discussion *110*

6.4 Summary *112*

7. Tissue correction function 113

7.1 Method *113*

7.2 Results *114*

7.3 Discussion 116

7.4 Summary 119

8. Measurements in a low energy proton beamline 121

8.1 Setup & method 122

8.1.1 Simulation setup 124

8.1.2 Depth dose and beam energy estimation 125

8.2 Results 126

8.2.1 OCL Beam energy estimation 126

8.2.2 Energy deposition comparison with simulation 127

8.2.3 Tissue conversion functions, simulation comparison 130

8.2.4 Depth dose distribution from IC and microdosimeter 131

8.2.5 Lineal energy 133

8.2.6 Significance of SV size 136

8.3 Discussion 138

8.4 Summary 140

9. Tracking “sandwich” microdosimeter 143

9.1 Energy resolution 144

9.2 Spatial Resolution 149

9.3 Tissue equivalence 153

9.4 Alternative setup for measuring secondaries in tissue 154

9.5 Development in MAPS technology 155

9.6 Summary and future work 156

10. Conclusions and outlook 159

References 163

Appendix A 171

1. Introduction

It is well known that radiation is damaging to living organisms and that the harm increases as more radiation energy is absorbed. The different biological effects, or endpoints, of radiation are studied in radiobiological experiments and include the probability to induce different forms of cancer, shutting down specific functions of cells or organs, and to examine the likelihood of killing cells. The aim of these experiments is to predict the effects radiation has on living matter based on both biological and radiation field properties. This is necessary in radiation protection to assess the danger of a radiation field in a human environment, or to predict the outcome and side effects of radiation therapy.

In traditional radiotherapy, where photons and electrons are used, the biological effect is predicted by parameters such as cell type, oxygen levels, fractionation regime and dose. The spatial and temporal dose distribution is thereby the only property of the radiation field that is of major interest. This changes for other types of radiation, as it is well known that heavier particles such as protons, neutrons and ions are much more effective at cell killing than photons and electrons. The biological effectiveness of heavier particles does not only depend on the particle's species, it also depends on their energy that constantly changes as the particles slow down. As these heavy particles also produce many types of secondary particles that also have a wide energy range, the biological effectiveness of heavy particles is more complex than that of photons and electrons, and the spatial dose distribution is not sufficient to describe the biological effects.

The concept of relative biological effectiveness (RBE) was created to compare the biological effects from different kinds of radiation, and is defined as (IAEA, 2005, p. 500)

$$RBE = \frac{D_{ref}}{D_{test}}, \qquad (1.1)$$

where the D_{ref} is the absorbed dose of a standardized radiation to obtain a specific biological effect, while D_{test} is the absorbed dose of the test radiation necessary to obtain the effect. While the RBE depends on several biological properties, it also depends on the radiation field and the quantities describing the radiation field should be biologically relevant and few, as a complete description would complicate the measurements and the radiobiological theory. Thus, the term radiation or beam *quality* was introduced, where the absorbed dose and quality were used to predict the biological effects.

Microdosimetry is a scientific field where the radiobiological effects are assumed to be due to energy deposition in micrometric volumes. It is thus principally simple and measurable. For the last 75 years a gas detector called the Tissue Equivalent Proportional Counter (TEPC) has been used for microdosimetric measurement (Harald H. Rossi & Rosenzweig, 1955) and it is regarded as the gold standard of microdosimetric measurements. However, the TEPC has its drawbacks, such as demanding a gas supply and high voltage. The devices are also quite large and bulky which gives poor spatial resolution and makes them susceptible to pile-up in high intensity beams as encountered in particle therapy. A detailed description of the TEPC is given in chapter 2.6. Silicon microdosimeters are developed as an alternative to the TEPC, as they do not require gas, can be operated at a few volts, and are cheap to mass produce. Their small size also makes them easy to handle, gives good spatial resolution and makes it possible to use them in high intensity beams. However, the silicon microdosimeters also have their drawbacks, as they are not tissue equivalent and the electronic noise of the current devices prevents manufacturing of sensitive volumes (SV) of 1 μm and below. A detailed description of the silicon microdosimeters is given in section 3.3. Thus, the silicon microdosimeters are currently not a replacement of the TEPCs, but an additional tool that can be used whenever the TEPC is not fit for a particular purpose or simply because it is cheaper or easier to use.

The Centre of Medical Radiation Physics (CMRP), University of Wollongong, Australia, has developed and tested several generations of silicon microdosimeters (Rosenfeld, 2016). The microdosimeters are silicon chips where an array of micrometer sized SVs are embedded at the surface. In this work, the 5th generation of silicon on insulator (SOI) microdosimeters developed by CMRP and fabricated by SINTEF in Norway was characterized and applied in a proton beamline used for radiobiological experiments.

1.1 Objectives and outline

The main goal of this work was to characterize the latest generation of silicon microdosimeters by testing their response in a variety of radiation fields and comparing them to the more ideal response from Monte Carlo (MC) simulations. This kind of work is necessary to conduct before the microdosimeters are put to use to know if the characteristics of the measured energy deposition spectra are due to the characteristics of the radiation field or the detector. It is also necessary to understand the operational limits of the microdosimeters, and to identify further improvements in future designs. In chapter 5, electrical characteristics of the microdosimeters were examined, and the microdosimeters response to soft photons and alpha particles from sources were investigated and compared to MC simulations.

In microdosimetry it is vital that the SV of any microdosimeter is clearly defined, with little or no charge collection outside the SV and a homogeneous charge collection within the SVs. In chapter 6, one of the microdosimeters were investigated with the ion beam induced charge collection (IBICC) technique to examine if the boarders of the SVs where clearly defined, and if the charge collection is homogeneous within the SVs. The IBICC technique was conducted with a C-12 beam that deposited a large dose such that radiation damage effects also were characterized.

One of the main disadvantages silicon microdosimeters is that the mean energy loss in silicon differs significantly from that in tissue (Lindborg & Waker, 2017, pp. 64-65). This difference changes quickly near the end of the particle tracks, making it difficult to relate the measurements in silicon to that in tissue. A novel tissue correction function for protons is presented and discussed in chapter 7 which aims to minimize the error when measurements from a silicon microdosimeter is tissue corrected.

In chapter 8 the microdosimeter was used to measure energy depositions and microdosimetric spectra of a low energy proton beamline. The measurements were conducted with several thicknesses of a polyamide absorber in front of the microdosimeter. The measurements were compared to both a MC simulation of the setup and the relative dose measurement from a commercial ionization chamber (IC) to investigate the performance of the microdosimeter. The simulation setup was also used to evaluate the tissue correction function from chapter 7 for low energy protons. The main objective was to perform a microdosimetric characterization of the beamline which is used of radiobiological experiments. This is done such that the result of the radiobiological experiments can be coupled to the microdosimetric measurements.

Chapter 9 discusses the possibility of using a stack of Monolithic Active Pixel Sensors (MAPS) as an alternative type of microdosimeter. With a stack of high granularity MAPS, it might be possible to track all particles entering and generated within the detector with micrometric resolution. Such a detector can give a very detailed image of any radiation field which might be used to create more detailed and exact models on radiation effects in biological matter.

2. Microdosimetry

In the 1940s and 50s it was understood that the radiation quality depended on the spatial density of energy depositions from charged particles (ICRU, 1983, pp. 1-2). The simplest way to quantify this was to use the average energy loss of the particles, dE/dx, also known as the *unrestricted linear energy transferal* (LET). Figure 2.1 shows that the RBE is almost constant below an LET of 5 keV/µm and increases sharply above 10 keV/µm up to a maximum at approximately 100 keV/µm, where it starts to decrease due to the so-called overkill effect (IAEA, 2005, pp. 500-501).

The LET is thus a simple quantity that also represents the radiation quality well. However, LET might be too simplistic as it is assumed that it is the energy deposition and not the energy loss of a particle that leads to a biological effect. This is important, since the energy loss of a particle often results in a secondary charged particle (usually delta electrons) that deposits its energy elsewhere. Thus, the position of the energy loss is not identical to the position of the energy deposit.

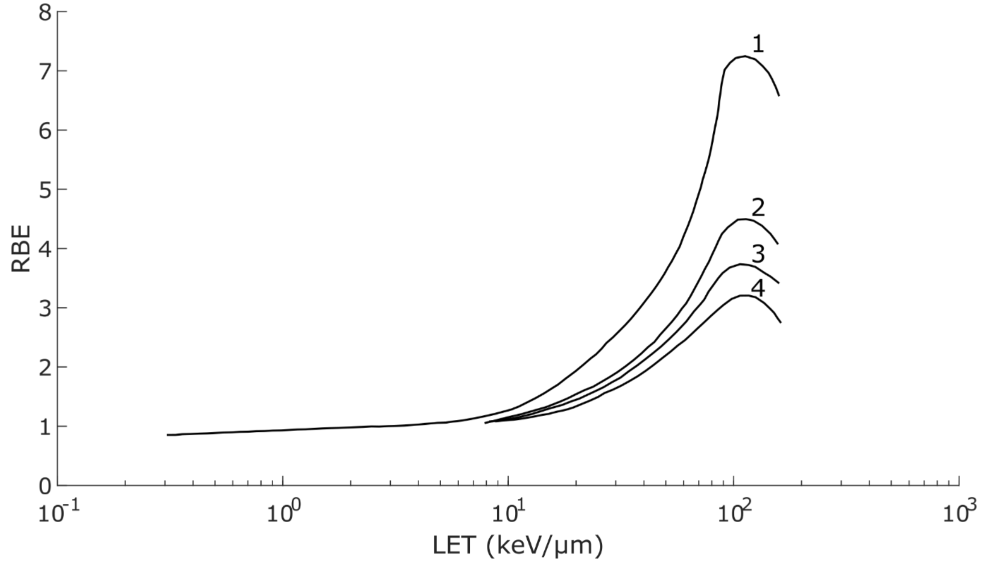

Figure 2.1: Measured RBE as a function of LET for survival of human cells from alpha, deuterons, beta and x-ray radiation. The curves 1-4 refers to a cell survival fraction of 80%, 20%, 5% and 0.5% respectively. Reproduced from (Barendsen, Walter, Fowler, & Bewley, 1963).

In order to improve the LET, the concept of *restricted LET* was conceived (ICRU, 1970),

$$\mathrm{LET}_\Delta = \left(\frac{dE}{dx}\right)_\Delta, \tag{2.1}$$

where the average energy loss is calculated for collisions with energy transferals below a specific value Δ. By lowering Δ, the distance between the position of the energy loss and the position of the energy deposits is also reduced.

The LET is also an average, a deterministic quantity, that depend on properties of the particle and the matter it traverses, whereas energy deposition along a particle path is stochastic. The LET also becomes very complex in mixed radiation fields, as it is normally calculated for each particle from properties of the particle and the material it traverses. Furthermore, the LET is difficult to measure which makes it impractical when assessing the quality of an unknown mixed radiation field, as is often the case in radiation protection and ion therapy.

Microdosimetry was developed to overcome the shortcomings of the LET as a quantity for radiation quality. Microdosimetry studies the distribution of the single energy depositions in space and time. It assumes that the biological effects stem from this pattern of energy depositions, and that it is irrelevant what particles produced the pattern. This method captures the stochastic nature of radiation energy deposition and should therefore in principle be able to predict the biological effects more precisely compared to the LET. It is also well suited for experimentation, as microdosimetric quantities are measurable. Thus, the mixed radiation fields in medical particle therapy and the hazards of unknown radiation fields in radiation protection can be measured and assessed.

In microdosimetry, there are two approaches that are closely related, regional and structural microdosimetry (H. H. Rossi & Zaider, 1996, p. 2). Regional microdosimetry considers the energy deposited for each event within a well-defined volume called a *site*. The track structure or the distribution of energy depositions within the site is not considered. This makes regional microdosimetry well suited for experimentation, where the site is the sensitive volume (SV) of a detector (microdosimeter). Information regarding the site should always follow the results obtained in regional microdosimetry, as the results depend on the site's size, shape, and material.

Structural microdosimetry is a more theoretical approach that does not utilize the concept of sites. Instead, it studies the microscopic patterns of energy deposition along the particle tracks. It is therefore a more exact description of how charged particles deposits energy and may offer better radiobiological predictions. As these microscopic patterns are difficult to measure, structural microdosimetry is mainly a theoretical approach. However, the results from experimental (regional) microdosimetry is used to further develop and test theories and hypotheses within structural microdosimetry.

2.1 Radiation interaction with matter

To understand the mechanisms of how radiation damages living organisms, it is vital to understand how radiation interacts with matter in general. For microdosimetry, it is most important to understand how energetic charged particles, such as electrons, protons and ions interact with matter. Neutral particles generally lose their energy by producing charged particles and thus virtually all radiation energy is eventually lost through the interactions of charged particles.

Charged particles predominantly interact with matter through the Coulomb force, where they interact with the atom's electrons and nucleus. The energy loss of charged particles happens mainly through interaction with atomic electrons, where they transfer energy to the electrons, leading to the ionization and excitation of the target atoms. This is known as inelastic scattering of the atom. If enough energy is transferred to an atomic electron, it can also become ionizing, and the resulting electron is known as a delta electron or delta ray. Delta rays can also be created through emittance of auger electrons after the ionization or excitation of an atom. Through conservation of momentum, an energetic electron can at maximum transfer half of its kinetic energy to another atomic electron, while protons and ions, which are orders of magnitude heavier than electrons, can at maximum transfer enough energy to the electrons such that its velocity is approximately double that of the incoming hadron. Thus, a highly energetic charged particle generates a large amount of delta rays along its path.

The nature of energy loss is a stochastic process, where the distance between two energy transferals and the amount of energy transferred in each collision is Poisson distributed. However, from a macroscopic viewpoint it is often useful to establish the mean energy loss due to electron collisions from a charged particle per unit of path length, i.e. the stopping power which is equal to the unrestricted LET. Proton stopping power in water can be seen in Figure 2.2. The stopping power can be calculated from the Bethe's formula with corrections, and for particles heavier than electrons it is given as (Leo, 1994, p. 24)

$$\frac{dE}{dx} = 2\pi N_A r_e^2 m_e c^2 \rho \frac{Z}{A}\frac{z^2}{\beta}\left[ln\left(\frac{2m_e\gamma^2 v^2 W_{max}}{I^2}\right) - 2\beta^2 - \delta - 2\frac{C}{Z}\right], \tag{2.2}$$

where

$r_e = 2.817 * 10^{-13}$ cm is the classical electron radius

$m_e = 0.511\ \mathrm{MeV/c^2}$

$N_A = 6.022 * 10^{23}$ $\mathrm{mol^{-1}}$is Avogadros number

I is the mean excitation potential

Z is the atomic number of the absorbing material

A is the atomic weight of the absorbing material

ρ is the density of the absorbing material

z is the charge number of the incident particle

β = v/c of the incident particle

$\gamma = \frac{1}{\sqrt{1-\beta^2}}$

δ is the density correction

C is the shell correction

W_{max} is the maximum energy transfer in a single collision

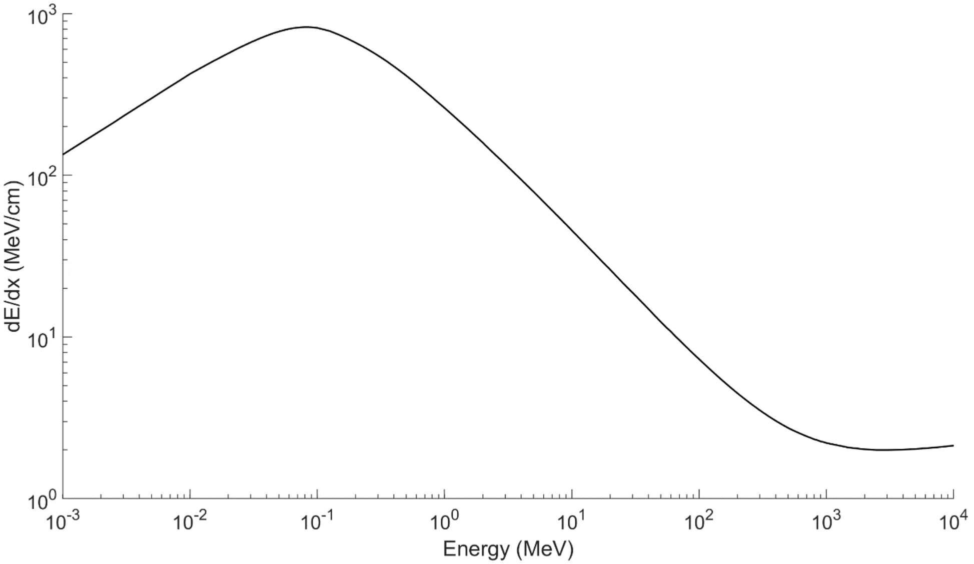

Figure 2.2: Electronic stopping power (dE/dx) for protons in water, made from PSTAR data from the National Institute of Standards and Technology (NIST) (Berger et al., 2017). PSTAR data is based on the Bethe's formula with corrections.

Thus, the stopping power depends on the particle's charge, velocity, and the properties of the material it traverses. While the stopping power of identical particles with equal energies is the same, they will not necessarily deposit the same amount of energy in a detector volume. This is because energy deposition is a stochastic process where the number of electron collisions and the amount of energy transferred in each collision varies. The single event energy deposition distribution in a detector generally becomes wider as the detector becomes thinner. This is because the relative number of collisions increases as the detector becomes thinner and due to the large range of possible energy transferals in a single collision. The energy deposition distribution in a thin detector therefore has a long tail towards higher energy deposition, known as a Landau distribution. This variance in energy deposition from identical monoenergetic particles is known as *energy straggling*. Due to the presence of energy straggling, the particles in a monoenergetic beam traversing the same material will have different ranges, which is known as *range straggling*.

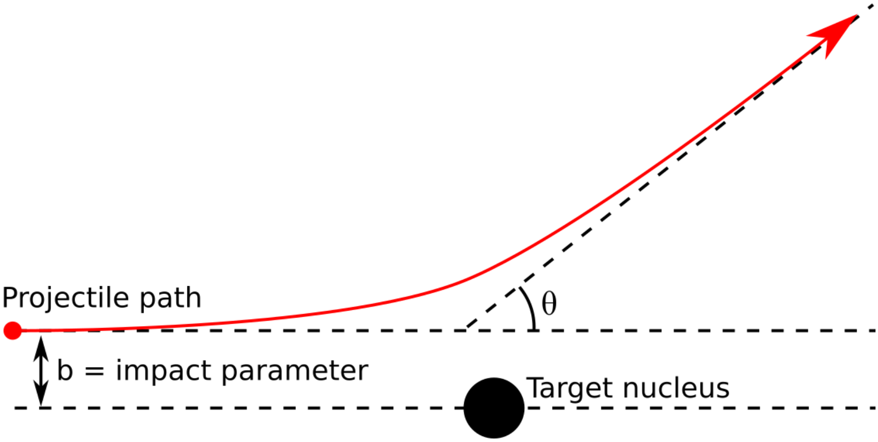

Figure 2.3: Schematic of a charged particle scattering off a target nucleus, showing the impact parameter, b, and the scattering angle, θ.

Ions can also interact with the atomic nuclei through the Coulomb force. The most common scenario is that the traversing particle has a relatively large impact parameter (Figure 2.3) such that the energy transferal is small. As the nucleus is normally heavier than the traversing particle, very little energy is transferred to the nucleus and the result is a minor elastic deflection from the traversing particles original path. The cross section for elastic scattering is modelled by the Rutherford formula, and it is proportional to $1/\sin^4(\theta/2)$, where θ is the scattering angle, shown in Figure 2.3 (Leo, 1994, p. 44). This shows that high angle scatters are unlikely, and thus charged ions mainly goes through several low angle deflections that gives a zigzag like pattern, known as Multiple Coulomb scattering.

Large angle deflection also occurs as ions scatter elastically off a nucleus with low impact parameter, although the cross section is low. As the deflection angle becomes higher in an elastic scattering, more momentum is transferred to the target nucleus. For high momentum hadrons scattering off light nuclei, this momentum transfer can be large, and the target nucleus can become ionizing itself.

High momentum ions with low impact parameter can also overcome the Coulomb barrier such that the ion and target nucleus interact through the nuclear force. These are inelastic collisions where the momentum is not conserved, as some energy is expended in exciting the nucleus and possibly the incoming ion, increasing their Q-value. This energy is released by the emission of radiation, such as gamma, beta, alpha, protons or neutrons, and the nucleus can also fission. Such inelastic scattering also produces a very high scattering angle and a large transferal of kinetic energy to the target nucleus if it is not considerably heavier than the incoming ion.

Electrons are also charged and thus interact through the Coulomb force, leading to collision energy loss that results in ionizations and excitations. As such, the mechanisms leading to the Bethe's formula (equation 2.2) is almost the same. As the incoming electron has equal mass as the atomic electrons, they will deflect when transferring energy, which is not the case for heavier charged particles. Furthermore, these particles are also indistinguishable, and the maximum energy transferal in a single collision is half of its energy (Leo, 1994, p. 37). However, the biggest difference from charged hadrons is that electrons radiate (bremsstrahlung) at relatively low kinetic energies when traversing matter. This is due to the sharp curvature that electrons experience due to the Coulomb force in the vicinity of a nucleus. The energy loss of electrons is thus due to collisions and bremsstrahlung, where collisions dominate the energy loss when the electron has energy below a few MeV (Leo, 1994, p. 37). As the electrons easily deflect, they generally have a much more erratic path than heavier charged particles.

Energetic neutral particles such as photons and neutrons generally interact with matter and lose energy via scattering, absorption, and conversion processes. However, they do produce ionizing charged particles that generates dense tracks of ionization and excitation and are thus denoted indirectly ionizing particles. Photons produce ionizing electrons through the photoelectric effect, Compton scattering and pair production (in addition to positrons). Most of the ionization occurring from a photon beam is thus from energetic secondary electrons and not the primary photons. Neutrons interact with the nuclei of the matter and as the distance between the nuclei in matter is relatively large compared to the range of the strong nuclear force, neutrons have a long mean free path between interactions, typically in the order of cm (Knoll, 2010, p. 57). The most important modes of energy loss for fast neutrons are through elastic and inelastic scattering with light nuclei since more energy can be transferred to light nuclei due to momentum conservation. In human tissue, proton (hydrogen) scattering is the main mode of energy loss, but recoil of heavier nuclei becomes important for higher neutron energies (ICRU, 1983, p. 8). For slow moving neutrons, neutron capture becomes more important which generally results in the emission of different forms of radiation such as gamma, beta, alpha, proton, deuteron, tritium, etc. (Leo, 1994, pp. 63-64).

2.2 Regional microdosimetry

In microdosimetry it is assumed that the biological effects due to radiation is best described by the spatial and temporal distribution of single energy deposition from radiation to matter. That is, if it were possible to perfectly know the exact position, time, and magnitude of every energy deposition, this would be the best measure of the following biological effect. Such single energy transferals are known as *transfer points* in microdosimetry and can be any of the energy loss processes by radiation described in the previous section. The energy absorbed by matter at a transfer point, i, is defined by (ICRU, 1983, p. 2; H. H. Rossi & Zaider, 1996, p. 4)

$$\epsilon_i = E_{in} - E_{out} + Q, \tag{2.3}$$

where E_{in} is the energy (excluding rest energy) of the particle arriving at the transfer point and E_{out} is the sum of energies (excluding rest energy) of all particles leaving the transfer point. Q is any change in rest energy, where a positive Q is a reduction of rest mass. Change in rest mass is particularly important when dealing with thermal neutrons, and less important when dealing with photons, electrons, and protons.

In experimental regional microdosimetry it is the total amount of energy deposition from a single event in the detector SV (site) that is of interest, equal to the sum of transfer points within the SV:

$$\epsilon = \sum_i \epsilon_i . \tag{2.4}$$

Most of the energy lost by radiation is through excitation and ionization, and thus they are deemed the most important energy loss processes in microdosimetry. However, detectors need a minimum amount of energy transferal in a single collision for it to be detected. In gas detectors this minimum threshold is equal to the minimum ionization potential of the gas molecules. For solid state detector this threshold is equal to the energy band gap, which is the minimum energy necessary to excite a valence electron into the conductive band. The transfer points that are below this threshold are not possible to measure. Transfer points with an energy magnitude above the detectable threshold is known as *relevant transfer points* (H. H. Rossi & Zaider, 1996, p. 5), and it is the sum of relevant transfer points that make up the measured energy deposition in experimental microdosimetry.

There is also an uncertainty of which types of transfer points are relative for biological change and damage. There is good reason to believe that only ionization, and not excitation, produces change in biological matter, as it is ionization that breaks up chemical bonds and makes atoms and molecules more chemically reactive. However, as the amount of energy lost due to ionization and excitation are similar for different forms of radiation (A. M. Kellerer, 1985, p. 80), these uncertainties are limited. These uncertainties have been lowered by using gas detectors for microdosimetry, where the atomic gas composition is like that in tissue.

2.3 Microdosimetric quantities

The microdosimetric quantities are defined by ICRU (1983), and in experimental (regional) microdosimetry they are based on the measured energy imparted, ϵ, to a well-defined SV from a single event.

The specific energy, z, is the quotient of all the energy imparted to a site by the mass of the site, m:

$$z = \frac{\epsilon}{m}. \tag{2.5}$$

The specific energy is recorded in a microscopic volume and has the same unit as the absorbed dose, Gy = J/kg. Unlike the absorbed dose, the specific energy is a stochastic quantity, as two identical and neighbouring sites will receive different specific energies when the radiation field is homogenous across both sites. By taking the mean of a specific energy distribution of several sites in a region one attains the absorbed dose, D, for this region, which is a deterministic value:

$$\bar{z} = D. \tag{2.6}$$

The lineal energy, y, is defined as the quotient of the energy imparted by a single event to a volume, ε, and the mean chord length through the volume, $\bar{l}$:

$$y = \frac{\epsilon}{\bar{l}}. \tag{2.7}$$

The lineal energy has the units of keV/μm, which describes the energy transferred to the volume per unit distance in a single event, similar to the LET. The mean chord length in a convex body when it is intersected by randomly distributed isotropic chords is given by (Sjöstrand, 2002)

$$\bar{l} = \frac{4V}{S}, \tag{2.8}$$

where S is the surface area of the volume V. The formula is thus valid for every convex SV shape in isotropic radiation fields, and for spherical volumes in both isotropic and directional radiation fields. The two most common SV shapes in microdosimeters are spheres and cylinders, where the mean chord lengths are

$$\bar{l}_{sphere} = \frac{4r}{3} \quad \text{and} \quad \bar{l}_{cylinder} = \frac{2rh}{r+h}, \tag{2.9}$$

where r is the radius of the sphere or cylinder, and h is the height of the cylinder.

When measuring or calculating the lineal energy it is useful to represent the distribution of the lineal energies in a probability density function, $f(y)$, usually called the *lineal energy distribution*. The expected value in the distribution is called the *frequency-mean lineal energy*, $\overline{y_F}$, and is the first moment of the distribution $f(y)$:

$$\overline{y_F} = \int_0^{\infty} y f(y) dy. \tag{2.10}$$

While the lineal energy is stochastic, the frequency-mean lineal energy is a deterministic quantity. It is often useful to see how the different lineal energies contribute to the absorbed dose. The lineal energy distributions simply show the frequency of how often the different lineal energy events occur and does not say how important the individual events are in establishing the absorbed dose. Since the high lineal energy events contributes more to the dose than the low linear energy events, the high linear energy events are more important when considering the dose. This gives rise to the dose probability density function

$$d(y) = \frac{y}{\overline{y_F}} f(y), \tag{2.11}$$

where $d(y)$ is often called the *dose-weighted lineal energy distribution*. The area under $d(y)$ gives the fraction of the total dose from the range of lineal energies that delineates the area. As an example, if the following is true for a lineal energy distribution:

$$\int_{1\frac{keV}{\mu m}}^{10\frac{keV}{\mu m}} f(y) = 0.1 \qquad \text{and} \qquad \int_{1\frac{keV}{\mu m}}^{10\frac{keV}{\mu m}} d(y) = 0.3, \tag{2.12}$$

then 10% of all lineal energies observed in the site is in the range of 1 and 10 keV/μm, which is found through $f(y)$, while 30% of the dose in the same volume comes from lineal energies in the same range, and this is found through $d(y)$. The expected value from $d(y)$ is called the *dose-mean lineal energy,* which is also the second moment of the distribution $f(y)$:

$$\overline{y_D} = \frac{1}{\overline{y_F}} \int_0^{\infty} y^2 f(y) dy. \tag{2.13}$$

Since the spread in linear energy is often over several orders of magnitude, a semi logarithmic plot is used to display $f(y)$ and $d(y)$, where the x-axis is log(y) and the y axis is $yf(y)$ or $yd(y)$. The basis for multiplying the distributions $f(y)$ and $d(y)$ with y is when using a logarithmic axis for y is the following:

$$\int_a^b f(y)dy = \int_a^b [yf(y)]\, d\log(y). \tag{2.14}$$

This means that the semi logarithmic plot retains the property that an area under the distribution will give the fraction of events from the range of lineal energies that delineates the area.

The calculations of the first and second moments of the specific energy distributions $f(z)$ are analogous to that of $f(y)$ shown above. However, it is important to note that while the specific energy, z, normally considers all energy imparted to the volume by several events, the lineal energy only considers the energy imparted from single events. If the single event specific energy is considered, it is denoted z_1 and its single event distribution is denoted $f_1(z)$.

2.4 Microdosimeter design criteria

In microdosimetry it is assumed that the biological effects from radiation stems from energy depositions in sensitive targets within tissue. The most studied “effect” is the likelihood of cell inactivation. For the microdosimetric measurements to be relevant, the SV of the microdosimeters must approximate the sensitive targets, which specifies the shape, size, and materials of the microdosimeters.

The atomic composition of the microdosimeter’s materials should be as similar as possible as the composition of tissue, such that the interaction cross section in tissue and microdosimeter are similar. Both the materials surrounding the SV and the SV itself should be tissue equivalent such that the secondary radiation field is like that in tissue, and the amount of energy deposition within the SV is equal to that of a site in tissue. ICRU (1989) gives and excellent overview of the atomic composition of human tissue and of tissue equivalent building materials. It is less important that the density is equal, as this is a simple scaling factor between density and volume size and will be elaborated in the following section.

The optimal size and shape of microdosimetric sites is a more difficult question than that of atomic composition. Throughout the history of microdosimetry, the postulated site sizes have varied from a few nm to above 10 µm in nominal diameter, from the thickness of the double DNA helix to cell sizes. In a review article on microdosimetric target size, Goodhead (2007) suggest that there are several critical targets that can lead to cell inactivation, and the most important is likely double strand breaks or more complex damage of the 2 nm wide DNA helix. Thus, the number of ionizations in 3-10 nm diameter sites is likely the best predictor for cell inactivation. However, there are other important radiobiological targets seen by the deformation of chromosomes (100-500 nm), and so-called non-targeted effects where hits trigger effects in other parts of a cell or in neighbouring cells, that might have effective sites of 10 µm and upwards. Several biological models have been created to predict biological effects from microdosimetric measurements and the site size has been determined by finding the best fit to survival data from cell experiments. Some of these models are presented in section 2.7.

No matter what site size is used, information on the geometry of the SV should always follow the measurement results as they depend on geometry. As an example, Figure 2.4 shows the lineal energy distribution from a Monte Carlo (MC) simulation of a 50 MeV proton beam impinging on a 1 and 10 µm diameter spherical site. The results show that the lineal energy distribution is significantly wider for the 1 µm dimeter site compared to the 10 µm site. While the frequency mean lineal energy was 1.12 keV/µm for both sites, the dose mean lineal energy was 1.53 keV/µm for the 10 µm site and 2.37 keV/µm for the 1 µm site, a 55% increase.

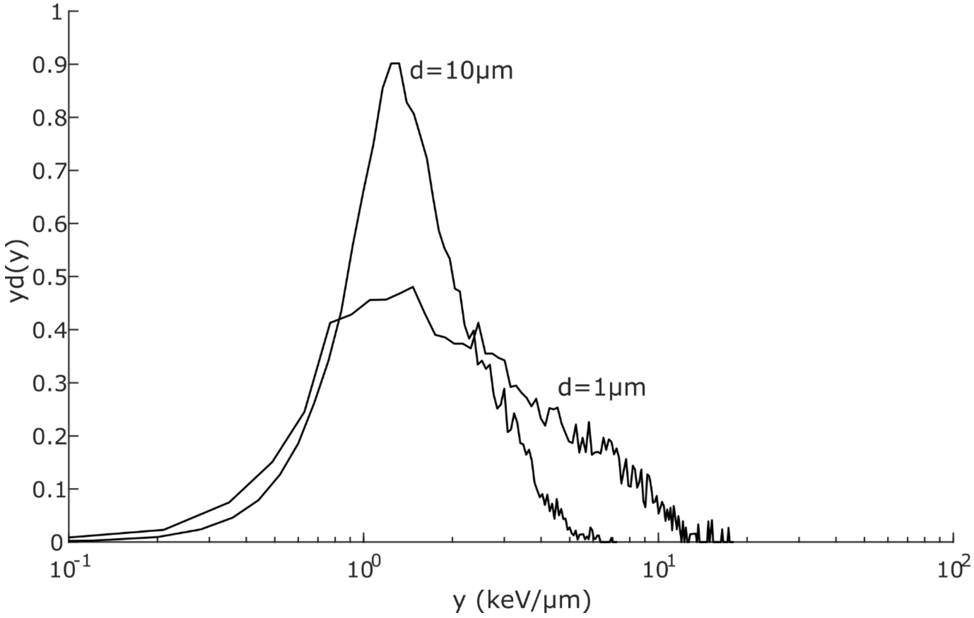

Figure 2.4: MC simulation results of the lineal energy in a 10 μm and 1 μm diameter spherical site composed of water from a 50 MeV proton beam using the Gate simulation toolkit. The spherical sites were positioned in the middle of a 400 x 400 μm^2 wide water box at 200 μm depths, with a circular 200 μm radius beam profile centred on the site. The size of the water box and the beam profile was chosen from the delta electrons' maximum path lengths from 50 MeV protons, which is approximately 200 μm in water (Berger et al., 2017).

The biological structures such as the DNA helix, chromosome, cell nucleus and cell differ significantly in shape and orientation within the body. It is therefore difficult to find an optimal shape and orientation with respect to radiation direction, and the microdosimeter shape has been designed by other criteria. The energy deposition from a charged particle will depend on track length through the SV, this leads to less energy deposition variance for a volume with a narrow chord length distribution. Although unproven it is assumed that spheres is the geometric shape that has the lowest chord length variance (Albrecht M. Kellerer, 1971), and since it is the only volume that is insensitive to the radiation field direction (isotropic response) it has been the favoured shape for microdosimeter (H. H. Rossi & Zaider, 1996, pp. 79-80). However, spherical SVs can be difficult to produce, and thus other geometries are used. Cylinders are a favoured alternative to spheres, but as the two have different chord length distributions, they will produce different single event spectra in identical radiation fields. The results from cylindrical SVs, and other shapes, can still be compared to that from spheres through appropriate scaling, demonstrated by (A. M. Kellerer, 1981). For solid state detectors it is currently impossible to manufacture well defined spherical SVs, but it is possible to produce cylinders and parallelograms, such as cubes. For an excellent overview of chord length distributions for different geometries and the resulting differences in microdosimetric spectra, see Bradley (2000).

2.5 Relative variance in single event distributions

In the standard mode of operation, the microdosimeters measures the energy from single events, and the results are often shown as a single event distribution, $f(y)$ or $f_1(z)$, or their weighted averages. The measured single event distribution is usually relatively wide as seen in Figure 2.4, and it can be useful to see which factors contribute to this width. The width of the distribution $f(x)$ can be quantified by the *relative variance,* V, and is defined as (A. M. Kellerer, 1985, p. 97):

$$V = \frac{\sigma^2}{m_1^2} = \frac{m_2}{m_1} - 1, \qquad (2.15)$$

where σ^2 is the variance (the square of the standard deviation), while m_1 and m_2 are the first and second moments of the distribution $f(x)$. If the single event distribution is represented in terms of lineal energy, $f(y)$, then $m_1 = \overline{y_F}$ and $m_2 = \overline{y_D}$. By applying the formula to the spectra in Figure 2.4, the relative variance is found to be 0.37 and 1.12 for the 10 and 1 µm diameter sites respectively.

The relative variance is a unitless index that expresses the width of any distribution, and the total relative variance, V_T, for a measured single event distribution is simply the sum of the variances of all the contributing random processes. For sites that are relatively small compared to the remaining track length of the charged particles, any changes to LET across the volume can be disregarded.

For such events, the relative variance is

$$V_T = V_L + V_t + V_L V_t + V_C + V_\epsilon + V_\delta + V_F + V_M, \tag{2.16}$$

where

V_L: The LET distribution of the particles traversing the site

V_t: The chord length or particles' path length distribution in the SV/site

V_C: The number of collisions distribution

V_ϵ: The amount of energy imparted in single collisions distribution

V_δ: The distribution of fraction of energy retained in the SV/site, which does not escape as delta radiation

V_F: Fano fluctuation, the distribution of charge carriers generated for the same energy imparted in the SV

V_M: The distribution of electronics noise and other measurement phenomena

The distribution due to LET (V_L) varies significantly and depends on the type of radiation. For a mono-energetic beam the LET variance is zero. For medical charged particle beamlines where the beam's energy is high and the spread is small out of the nozzle, the LET variance will be close to zero. As the beam penetrates a patient or water phantom, the beam energy is lowered and the energy spread becomes larger due to straggling, which leads to larger LET variance with increasing depth. The LET variance will be at maximum in the distal dose fall off (DDF), shortly after the Bragg peak (BP). Higher initial beam energy will position the BP further into the irradiated medium, and it will increase the LET variance at the BP due to more straggling. Rossi & Zaider (1996, p. 79) reports that the LET variance for ^{60}Co gamma radiation is 0.3, while it is 0.8 for 2 MeV neutron radiation.

The chord length distribution (V_t) is believed to be the smallest in spherical volumes, although this is unproven (Albrecht M. Kellerer, 1971; H. H. Rossi & Zaider, 1996,

p. 79). For spherical volumes $V_{t,sphere} = 0.125$, and the response is the same for directed beams as well as isotropic radiation fields. A detailed presentation of chord length distributions and variance for various geometries can be found in Bradley (2000). For cylindrical SVs, as used in this thesis, the variance in an isotropic field depends on the ratio of height over diameter, with a minimum of 0.25 when the height and diameter is equal. However, for directional beams along the cylinder core the variance is 0, and for beams perpendicular to the core it is 0.081 (H. H. Rossi & Zaider, 1996, p. 81) irrespective of height and diameter. Although the chord length distribution for cylinders is generally larger than for spheres, they tend to be much smaller than the total variance in microdosimetric spectra, V_T.

V_C, V_ϵ and V_δ are all aspects of energy and range straggling. They depend on particle weight, velocity, charge, and site size, and thus their variance is difficult to establish theoretically. The variance can be established through Monte Carlo simulations or experimentally using mono energetic radiation where the other contributions to the total variance is small.

The number of produced charge carriers for the same deposited energy, ϵ, fluctuates. This is known as Fano fluctuations, and the relative variance is

$$V_F = \frac{F}{n}, \tag{2.17}$$

where F is the Fano factor and n is the number of charge carriers produced. For silicon detectors F is approximately 0.1 (Spieler, 2005, p. 54), while it is approximately 0.3 for tissue equivalent (TE) gas (H. H. Rossi & Zaider, 1996, p. 89) used in gas detectors. In typical silicon pad detectors, the minimum detectable signal is usually above 600 electron-hole pairs, and thus the Fano fluctuations is negligible in these detectors.

The electronics noise in a solid-state detector system is mainly dependent on the preamplifier and the detector capacitance, and it is gaussian. The relative variance for energy deposition ϵ is

$$V_M = \frac{\sigma_{pa}^2}{\epsilon^2}, \qquad (2.18)$$

where σ_{pa} is the RMS noise from the preamplifier with the detector connected and voltage bias applied. When using discrete preamplifiers connected to a silicon detector for spectroscopy, σ_{pa} is typically 2-5 keV and the minimum detectable threshold it typically above 10 keV, thus the total relative variance depends little on the electronics noise. However, the electronics noise is important as it determines the lowest possible signal that can be detected i.e. the detection threshold (see section 3.2).

The formula for the relative variance (2.16) can thus be shorted to

$$V_T \approx V_L + V_t + V_S, \qquad (2.19)$$

where $V_S = V_C + V_\epsilon + V_\delta$ is the relative variance due to straggling effects.

The spectra in Figure 2.4 were created from a 50 MeV monoenergetic proton beam at a depth of 200 μm in water. The total relative variances were 0.37 and 1.12 for the 10 and 1 μm diameter sites, respectively. The LET variance (V_L) is close to zero due to the small amounts of straggling after 200 μm of water, and since proton LET changes relatively slowly with energy at 50 MeV. The variance due to the chord length distribution (V_t) is 0.125 since the site is spherical. There is no variance due to experimental measurement uncertainties since this is a simulation, such that V_M and V_F are both zero. Thus, the total variance is made up of straggling effects (V_S) and chord length distribution (V_t), and V_S is approximately 0.25 and 1.00 for the 10 and 1 μm diameter sites respectively.

2.6 Tissue Equvalent Proportional Counter (TEPC)

The tissue equivalent proportional counters (TEPC) is generally regarded as the gold standard for experimental microdosimetry. The TEPC is often also referred to as just proportional counter or Rossi counters after the inventor Harald Rossi, who is also considered the father of microdosimetry (M. Kellerer 2002).

The TEPC is usually a spherical or cylindrical gas detector that measures the number of ionizations in a tissue equivalent gas, where the diameter of the gas volume (the SV) is typically from 10 to 150 mm, although smaller has been developed (Lindborg & Waker, 2017, p. 48). The TEPC simulates smaller volumes by lowering the pressure of the gas. This is valid if the energy loss of a charged particle in a tissue volume with diameter d_t is equal to the energy loss in a gas volume with diameter d_g (ICRU, 1983, p. 27):

$$\mathit{\Delta} E_t = (S/\rho)_t \rho_t d_t = (S/\rho)_g \rho_g d_g = \mathit{\Delta} E_g, \tag{2.20}$$

where ΔE_t and ΔE_g is the average energy deposition in the tissue and gas volume respectively, while $(S/\rho)_t$ and $(S/\rho)_g$ is the mass stopping power, and ρ_t and ρ_d are the densities. The diameters in the equation can be exchanged with any trajectory through the volume if they are equivalent, and the equation holds for any shape as long as they are equal. If the atomic composition of tissue and the gas are the same, the mass stopping powers are independent of density and the tissue density is set to unity, then

$$\rho_g = \frac{1}{d_g/d_t} = \frac{1}{k_{gt}}. \tag{2.21}$$

The formula gives the necessary gas density to simulate a tissue volume of equal shape where the track length through the tissue volume is k_{gt} times smaller. However, the stopping power is not independent of density, as seen by the density correction factor, δ, in the Bethe’s formula (equation 2.2). The error from this is small for particles with energy below GeV/u, and can thus be ignored in typical radiation protection and medical applications (Leo, 1994, pp. 25-26).

The TEPC is built on the working principles of classical proportional counters where a thin anode wire runs along the centre of the gas volume (Figure 2.5). When the gas molecules are ionized by passing radiation, the electrons will drift towards the central anode and be collected, while the ions drift towards the cathode walls.

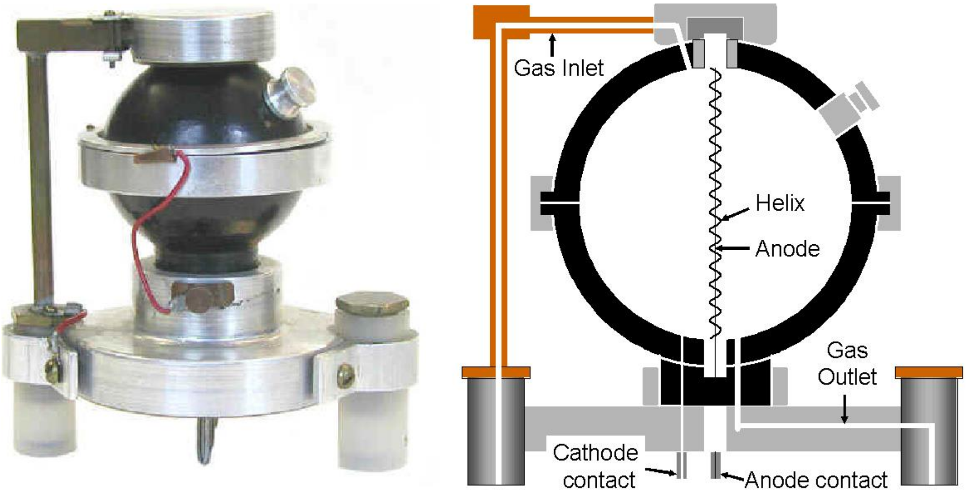

Figure 2.5: Photo and principle sketch of TEPC used by Harald Rossi at Columbia University. Taken with permission from ("Rossi Tissue Equivalent Proportional Counter (ca. 1960)," 2011)

To increase the signal, the anode is kept at such a high potential that the electric field near the anode wire accelerates the electrons enough to further ionize new gas molecules. As the new electrons are also accelerated enough to further ionize the gas, an avalanche of ionization takes place for every primary ionization from the radiation.

Since the electric field strength falls of as 1/r, the avalanche is restricted to the volume near the anode wire such that the overwhelming number of primary ionizations take place outside the avalanche volume. However, in spherical TEPCs the distance between the anode wire and cathode wall varies, and as a result the electrical field strength also varies yielding different gain along the wire. By having a wired helix surrounding the central anode and keeping it a potential between that of the anode and cathode, the avalanche is contained within the helix with a constant gain along the anode wire (Lindborg & Waker, 2017, p. 50). The *gas gain* due to the avalanche effect is typically between 100 and 1000. This yields a signal strength that is proportional to the number of primary ionizations in the gas.

When the gas pressure is lowered the electrons' mean free path between collisions is increased, allowing them to accelerate longer and gaining more energy. This effect extends the volume where the avalanche takes place. When a primary ionization takes place within the avalanche volume it will only receive a partial gain from the avalanche effect, and the energy deposition is recorded as smaller than it should be. Thus there is a threshold of how low the gas pressure can become, resulting in a lower limit of the simulated site of a few hundred nm (Lindborg & Waker, 2017, p. 49).

The TEPC walls and gas mix are designed to be tissue equivalent. Table 2-1 shows the atomic composition of the most common building materials (Lindborg & Waker, 2017, p. 46) along with the composition of soft tissue according to ICRU (ICRU, 1989, p. 22). A-150 is a plastic designed for the TEPC wall that is also conductive due to its large fraction of carbon, making it function as the detector's cathode. The TE gases are mostly based on methane or propane, which are mixed with CO_2 and N_2 to become more tissue equivalent. The large fraction of oxygen in tissue is partially substituted by carbon in the materials in Table 2-1, especially for A-150. However, an overview in Appendix C in ICRU (1983, pp. 75-79) shows that for the energies relevant in medical application the mass energy transfer coefficient for photons, the kerma for neutrons, and mass stopping power for electrons, protons and alpha particles there is little difference between the building materials in Table 2-1 and that of tissue. This means, that for most of the particles and energies relevant for medical and radiation protection, there is little difference in energy deposition between tissue and the building materials listed in Table 2-1.

Table 2-1: Elemental composition in percent by weight of soft tissue (ICRU) and the most common TEPC building materials (ICRU, 1989, pp. 22, 37-38; Lindborg & Waker, 2017, p. 46)

	H	**C**	**N**	**O**	**F**	**Ca**
Soft tissue (ICRU)	10.1	11.1	2.6	76.2		
A-150	10.1	77.7	3.5	5.2	1.7	1.8
Methane based TE gas	10.2	45.6	3.5	40.7		
Propane based TE gas	10.3	56.9	3.5	29.6		
Propane	18.2	81.8				

The TEPC must be kept at constant pressure for the simulated site size to be stable and for the gas multiplication to be constant. In addition, the most common wall material, A-150, absorbs moisture which is slowly released as water vapor when the pressure is lowered (Lindborg & Waker, 2017, p. 46). In a sealed TEPC this can lead to a slow increase in pressure and the gas becomes less tissue equivalent as an increasing portion of the gas becomes water vapor. The most common solution is to have a gas system, where there is a continuous flow of TE gas with pressure gauges and valves at the gas input and output line that regulates the flow and pressure. This keeps the pressure and atomic composition of the gas stable (Lindborg & Waker, 2017, pp. 99-101). However, in a recent study a sealed mini TEPC was used to measure the microdosimetric spectra along a the spread out Bragg peak (SOBP) of a proton beam twice with 4 month apart without gas refilling (Conte et al., 2019). The results showed that the measured $\overline{y_D}$ changed by less than 3% and the spectra were within the statistical uncertainty.

The large difference in density of the gas volume and the surrounding walls results in a few energy deposition events that would not have taken place if the SV and the surroundings were the same density. These effects occur because the radiation does not always follow straight lines due to scattering and is known as wall effects (ICRU, 1983, pp. 28-30), and the four types of wall effects are shown in Figure 2.6.

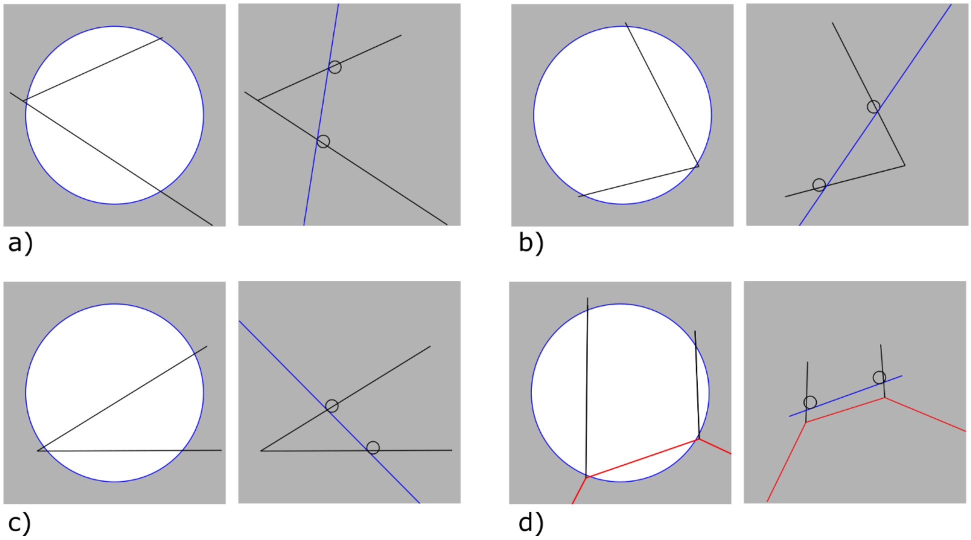

Figure 2.6: Illustrations of the four types of wall effects: a) delta ray effect, b) re-entry effect, c) V-effect, and d) scattering effect. The illustrations show four events and how they would cross a gas cavity (left) and a true micrometric sized volume with homogenic density (right). The blue line represents the border of the white gas cavity (left figures) and the position of this border in a volume with homogenic density (right figures).

Delta ray effect (Figure 2.6 a) occurs when a charge particle produces a delta ray just prior to entering the gas cavity, where both the primary particle and the delta ray passes the cavity. In a true micrometric site, it is much more unlikely that both events would be recorded. The delta ray effect is most important for high velocity charged particles since they produce the longest reaching delta rays.

Re-entry effect (Figure 2.6 b) occurs when an electron enters the same gas cavity a second time. The two entry points might be so far from each other that they would not enter the same micrometric volume twice. This effect only applies to electrons due to their tortuous path.

V-effect (Figure 2.6 c) is due to nonelastic nuclear collisions where several energetic particles are produced. Like the delta ray effect, it is much more likely that the tracks of the secondaries pass through a large cavity than through a true micrometric volume.

Scattering effect (Figure 2.6 d) occurs when a neutral particle produce two or more charged particles and the distance between the collisions is such that the charged particles cross the same cavity, but not cross the same micrometric volume. This effect applies to neutrons and photons that undergo multiple scatterings.

The wall effects have been reduced significantly by wall-less counters, where the "wall" is replaced by a grid of TE plastic (Lindborg & Waker, 2017, pp. 53-55; H. H. Rossi & Zaider, 1996, p. 105).

Due to the relatively large cross section of traditional TEPCs, single event spectra cannot be recoded in high intensity beams, such as medical beamlines with cyclotrons. A miniature TEPC with a cylindrical SV with diameter and height of only 0.9 mm has been developed to handle the high flux of medical beamlines (De Nardo, Cesari, et al., 2004). The Mini TEPC has been used to successfully measure the microdosimetric spectra along the SOBP of a medical proton beamline (De Nardo, Moro, et al., 2004) and in Boron Neutron Capture Therapy (BNCT) (Moro et al., 2009). Another benefit of the mini TEPCs it that they can simulate even smaller volumes since it is the pressure that sets the minimum simulated site (Lindborg & Waker, 2017, pp. 93-94).

2.7 Biological models

In radiation therapy there is often a tight gap between good tumour control probability and high probability of normal tissue complications. Thus, it is essential that the uncertainty in the dose and RBE be as small as possible, and one standard deviation uncertainty in dose delivery should not exceed 3-5% (IAEA, 2010). When heavier ions such as ^{12}C are used, an RBE of 3-4 is typical in the spread-out Bragg peak such that it is imperative that the uncertainty in RBE is as low as possible. This demands accurate biological models that can predict the effects of various radiations.

Several biological models have been created over the last decades, and four models are presented here. The linear quadratic (LQ) model is the most used. It is based on the survival curves of cell experiments and has been very successful within photon therapy. The theory of dual radiation action (TDRA) was the first model based on microdosimetry and thus has historical value and was also instrumental in the development of the microdosimetric-kinetic model (MKM). The MKM is also based on microdosimetric measurements and is used in the treatment planning for heavy ion therapy in Japan. The local effect model (LEM) is not directly based on microdosimetric measurements, rather it is based on *amorphous* track structure models that predict the local dose deposition around an ion track. However, the amorphous track structure models can be tested through microdosimetric experiments.

2.7.1 Linear Quadratic model

The cell survival fraction, SF, in radiobiological experiments is generally well described by the linear quadratic (LQ) relationship

$$SF(D) = e^{-(\alpha D+\beta D^2)}, \qquad (2.22)$$

where α is the linear term that describes the initial slope of the cell survival curve, while β is a smaller quadratic term that becomes increasingly important for higher doses D. Typical cell survival curves are shown in Figure 2.7 for low LET radiation, such as photons and electrons, and for high LET radiation, such as low energy heavy ions.

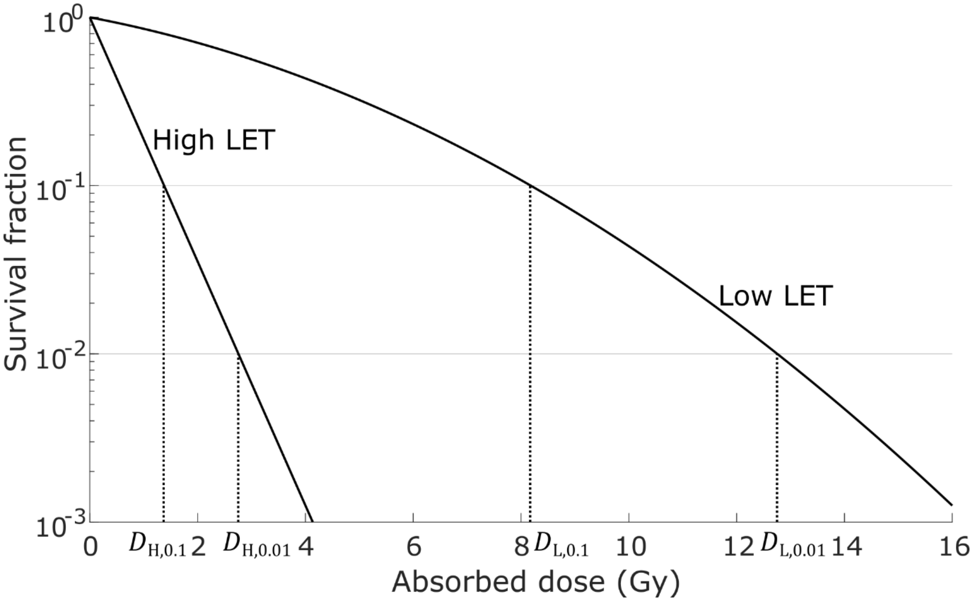

Figure 2.7: Typical cell survival curve for high and low LET radiation. The doses that yield 0.1 and 0.01 survival fraction for the high LET radiation ($D_{H,0.1}$ & $D_{H,0.01}$) and low LET radiation ($D_{L,0.1}$ & $D_{L,0.01}$) is marked along the x-axis. The figure is reproduced from (IAEA, 2005, p. 494).

The RBE can be calculated from the survival curves in Figure 2.7, where the doses that results in 0.1 and 0.01 survival fraction are marked for the high LET radiation ($D_{H,0.1}$ & $D_{H,0.01}$) and for the low LET radiation ($D_{L,0.1}$ & $D_{L,0.01}$). The RBE is calculated from equation (1.1) for 0.1 and 0.01 survival fraction:

$$RBE_{0.1} = \frac{D_{L,0.1}}{D_{H,0.1}} = \frac{8.17}{1.38} = 5.9 \qquad RBE_{0.01} = \frac{D_{L,0.01}}{D_{H,0.01}} = \frac{12.75}{2.75} = 4.6. \tag{2.23}$$

This shows the same trend as in Figure 2.1, where the RBE fall as the survival fraction falls.

It is believed that the effect from a single dose, d, in radiotherapy is described by the logarithm of the cell survival function (Mayles, Nahum, & Rosenwald, 2007, p. 167), such that

$$E = -\ln(\mathrm{SF}) = \alpha d + \beta d^2. \tag{2.24}$$

For n fractionations, where the total dose is $D = nd$, the effect becomes

$$E = n(\alpha d + \beta d^2) = \alpha D + \beta d D, \tag{2.25}$$

which can be rewritten as

$$E = \alpha D \left(1 + \frac{d}{\alpha/\beta}\right). \tag{2.26}$$

The formula predicts the biological effect based on the fractionation dose, d, and total dose, D, while the α and β values are specific for the cell line being irradiated. The formula is much used in radiotherapy to predict the effects when altering the fractionation dose and total dose when radiating various tissue and cancer types. As the cancer cells and the surrounding healthy tissue usually have different α and β values, the formula can be used to find a fractionation regime that give optimal biological effect for cancer cells, while minimizing the effect in healthy tissue (Mayles et al., 2007, pp. 168-170). The formula for the biological effect (2.26) is expected to be valid for fractionation doses between 2 and 10 Gy (Brenner, 2008).

Since the fractionation regime has little effect on the first term in equation 2.26, it is assumed that the α parameter is due to single event energy deposition.

The biological effect predicted by equation 2.26 can also be used to estimate the RBE for different radiations if the α and β are known for those radiations. By rewriting the equation in terms of total absorbed dose, D, and demanding that the effect, E, is the same for the two radiations with doses D_γ and D_b, the RBE or the weighting factor which is used by IAEA (IAEA, 2008) becomes

$$W_b = \frac{D_\gamma}{D_b} = \frac{\alpha_b \left(1 + \frac{d_b}{(\alpha/\beta)_b}\right)}{\alpha_\gamma \left(1 + \frac{d_\gamma}{(\alpha/\beta)_\gamma}\right)}, \tag{2.27}$$

where d_b and d_γ are the fractionations doses used to achieve the total dose of D_b and D_γ respectively.

Although the equation for the cell survival (2.22) and the biological effect (2.24 - 2.26) are similar, and α and β appear in both, they are not necessarily the same (Lindborg & Waker, 2017, p. 108). However, α is still assumed to be due to single energy deposition events in both the cell survival curve and in the biological effect equation. Thus, it is assumed that α is strongly correlated to the beam quality.

2.7.2 Theory of dual radiation action (TDRA)

The theory of dual radiation action was an early biological model based on microdosimetry created by Kellerer and Rossi (1972). The theory was developed through three models: the site model, the distance model, and the model of compound dual radiation action. A brief presentation of the models is given here with emphasis on the site model which has similarities with the MK-model. A detailed description of the TDRA is given in (H. H. Rossi & Zaider, 1996, pp. 229-250).

TDRA assumes that radiation effects are the product of lesions that form from combined pairs of sublesions, and that the number of sublesions are proportional to the dose. Furthermore, it is assumed that the number for lesions formed from pairs of sublesions mostly stem from single events in high LET radiation, while they mostly come from two separate events in low LET radiation. It was also assumed that the geometric distribution and the distances between the sublesions were not important if they were within a sensitive volume of a certain size. In the site model the biological effect, E, is the number of formed lesions and depends on the dose, D, and the dose mean specific energy, $\bar{z}_D$, and is given by

$$E = c(\bar{z}_D D + D^2), \tag{2.28}$$

where $\sqrt{c}$ is the average number of combining sublesions produced per unit of z. The RBE for a radiation with high LET (H) compared to one with low LET (L) is found by demanding that the effect of two radiations be equal

$$c_H\left(\bar{z}_{D,H} D_H + D_H^2\right) = c_L\left(\bar{z}_{D,L} D_L + D_L^2\right) \tag{2.29}$$

By assuming that $c_H = c_L$, the RBE becomes

$$RBE = \frac{D_L}{D_H} = \frac{1}{2D_H}\left[\sqrt{\bar{z}_{D,L}^2 + 4D_H\left(\bar{z}_{D,H} + D_H\right)} - \bar{z}_{D,L}\right]. \tag{2.30}$$

For low doses, $\bar{z}_D \gg D$, the D^2 in equation (2.29) can be disregarded, and by still assuming that $c_H = c_L$, the RBE can be simplified to

$$RBE = \frac{D_L}{D_H} \approx \frac{\bar{z}_{D,H}}{\bar{z}_{D,L}} = \frac{\bar{y}_{D,H}}{\bar{y}_{D,L}}, \tag{2.31}$$

Due to the saturation effect where the RBE drops as the LET goes beyond 100 to 150 keV/µm, a corrected lineal energy, $y^{\star}$, is used instead of $\bar{y}_D$ (A. M. Kellerer & Rossi, 1972) and is defined as

$$y^{\star} = \frac{y_0^2 \displaystyle\int_0^{\infty}\left[1 - e^{-\left(\frac{y}{y_0}\right)^2}\right] f(y)\, dy}{\int_0^{\infty} y f(y) dy}, \tag{2.32}$$

where y_0 is typically in the range 125 to 150 keV/µm. A site with diameter from 1-3 µm was found to predict the RBE for several neutron beam experiments. However, experiments with very low energy x-rays of 0.3 keV where the photoelectrons have a range of approximately 7 nm showed much higher RBE than the site model could predict (Goodhead, Thacker, Cox, & Wilkinson, 1979). This indicated a target size in the order of 10 nm and not 1-3 µm. This led to the development of the distance model that considers the distance between the sublesions and the structure of where they are formed. In the distance model, the number of lesions is

$$E = K\left[D\int_0^{\infty} t(x)\gamma(x)dx + D\right], \tag{2.33}$$

where $\gamma(x)$ is the probability that two sublesions forms a lesion where x is the distance between them, and $t(x)$ is the proximity function that describes the distance between the energy depositions of a single event and is thus related to the quality of the beam. A detailed description on proximity functions is found in (H. H. Rossi & Zaider, 1996, pp. 176-201).

In the model of compound dual radiation action, the sublesions and lesions are exchanged with single strand breaks (SSB) and double strand breaks (DSB) of the DNA helix. It is assumed that SSB are usually not lethal as they are easily repaired, and that DSB have a much higher probability of being lethal, although they can be repaired as well. Since DSB occurs from two SSBs only a few nm apart, it is considered unlikely that they can occur from two separate events even from high doses of low LET radiation (Lindborg & Waker, 2017, p. 110). Like the site model, compound dual radiation action assumes that there is a volume where the geometric distributions of energy depositions are unimportant. Within this volume the pairwise combinations of SSBs forms DSBs. However, this volume has the size of approximately 10 nm instead of 1-3 μm.

2.7.3 Microdosimetric-kinetic model (MKM)

The microdosimetric-kinetic model (MKM) builds on the principles of the TDRA site model, and was created and developed by Hawkins in (1994, 1996, 1998, 2003, 2006). Hawkins' MKM was later modified by Kase et al. (2006), and is now used for calculating the biological effective dose for carbon ion therapy at the National Institute of Radiological Sciences (NIRS) in Japan (Inaniwa et al., 2015).

The MKM assumes that there is a sensitive nucleus volume within each cell that contains the DNA (Hawkins, 1994). Furthermore, the model divides the nucleus volume into spherical sub volumes of equal size called domains, which are equivalent to sites in microdosimetry. The domains have equal probability of forming lesions for the same deposited dose. The size and shape of the nucleus volume in MKM is not well known and it is not the same as the cell nucleus as defined in microbiology. The domain are assumed to be typically 0.5 to 1 μm in diameter, and the nucleus is assumed to have several hundred domains (Hawkins, 2003).

The MKM assumes that two forms of lesions can occur within the domains of the nucleus, type I and type II (Hawkins, 1996). Type I lesions are always lethal to the cell and cannot be repaired and are thought to be complex DSB in the DNA. Type II lesions can undergo 4 different processes with different probabilities of lethality and repair. If two or more type II lesions such as SSB that are separately repairable occur in the same domain, they can combine and become lethal. However, type II lesion cannot combine if they are formed in neighbouring domains within the same cell nucleus.

By using low LET radiation the number of lethal lesions in a cell nucleus are assumed to be Poisson distributed among the domains of the nucleus. It is assumed that the number of lethal lesions in a domain are proportional to the dose deposited in it, and the average number of lethal lesions in a cell nucleus is then given by (Hawkins, 1998)

$$\bar{w}_n = \left[\alpha_0 + \beta\left(\bar{z}_{1,D}\right)_d\right] D + \beta D^2 = \alpha_P D + \beta D^2, \qquad (2.34)$$

where $\left(\bar{z}_{1,D}\right)_d$ is the single event dose-mean specific energy of domain d that can be exchanged with the lineal energy through $\bar{z}_{1,D} = \frac{\bar{l}}{m} y_D$. The coefficients α_0 and β describe the kinematics of forming lesions and are assumed to be independent of radiation quality. In the limit of zero dose, where the survival fraction is one, RBE is proportional to $\left(\bar{z}_{1,D}\right)_d$ and is given by (Hawkins, 1998)

$$\mathrm{RBE}_1 = \frac{\alpha_0 + \beta(\bar{z}_D)_d}{\alpha_R} = \frac{\alpha_P}{\alpha_R}, \qquad (2.35)$$

where α_R is the initial slope of the survival curve for the low LET reference curve, usually ^{60}Co gamma or 250 kV x-rays.

This predicts a linear growth of RBE with LET, which is not in agreement with the experiments. Since high LET particles deposits their energy near their track, the domains in the vicinity of the tracks receive a higher number of lesions than the domains further away, even for domains within the same cell nucleus. Thus, the number of lethal lesions in the domains of a cell nucleus is not Poisson distributed for high LET particles. This led to the development of a saturation correction factor, $\alpha^\star$, which is valid for low enough doses that the probability for cells traversed by more than one track can be ignored. The new MKM for the average number of lesions in the cell was (Hawkins, 2003)

$$\bar{w}_n = \alpha^{\star} D \approx \left(\frac{1 - e^{\alpha_P \left(\bar{z}_{D,s}\right)_n}}{\alpha_P \left(\bar{z}_{D,s}\right)_n} \right) [\alpha_0 + \beta (\bar{z}_D)_d] D = \alpha_P D + \beta D^2, \qquad (2.36)$$

where $\left(\bar{z}_{D,s}\right)_n$ is the dose-mean specific energy to the cell nucleus volume. Thus, the new formula for the number of lesions in a cell depends on the specific energy in both the cell nucleus $\left(\bar{z}_{D,s}\right)_n$ and in the domains $(\bar{z}_D)_d$.

The MKM was used to predict the survival curves of human salivary grand tumour (HSG) and GM05389 cells for a broad range of LETs from various ion beams along with 200 kV x-rays and ^{60}Co γ (Kase et al., 2006). The beam quality was measured by a commercial spherical TEPC simulating a 1.0 µm diameter volume. The authors showed that model predicted the survival curve better when the saturation effect was applied to the domain as well, and not just for the nucleus. The MKM was then modified to

$$\bar{w}_n = [\alpha_0 + \beta (z_D^{\star})_d] D + \beta D^2, \qquad (2.37)$$

with

$$(z_D^{\star})_d = \frac{\bar{l}}{m} y^{\star}, \qquad (2.38)$$

where $y^{\star}$ is defined in equation (2.32), where y_0 was 150 keV/µm.

Kase et al. (2006) showed that the new model predicted the survival curve well for the two cell lines across a wide range of LETs and particle species. However, the model did not perform well for the ^{60}Co γ and for LETs above 450 keV/µm.

2.7.4 Local Effect Model (LEM)

The local effect model (LEM) was developed by Scholz and Kraft (1994, 1996) and hypothesises that the probability of cell inactivation depends only on the local dose deposited in sensitive target volumes within the cell nuclei. The model assumes that there is no principle difference between the dose deposition by photons and ions, as most of the dose is deposited by electrons in both cases. The difference is that the dose distribution from photon radiation is near homogenous, while for ions it is concentrated along their tracks. Thus, there is a difference in the dose distributions on a micrometric scale between photon and ion radiation.

Due to the homogeneous dose deposition of x-rays, the local dose in the sensitive volumes is equal to that of the surrounding macroscopic volume. This makes x-ray survival data particularly useful to estimate the dependency between the number of lethal events within a cell nucleus and the local dose. Where the number of lethal events in a cell nucleus is taken from the survival data:

$$N(D) = -\ln S(D). \tag{2.39}$$

It is assumed that the cell nucleus contains a homogeneous distribution of sensitive volumes such that the lethal events from photon radiation will be randomly distributed throughout the nucleus. The mean lethal event density for a nucleus with a volume, V, is then

$$v(D) = \frac{N(D)}{V} = \frac{-\ln S(D)}{V}, \tag{2.40}$$

where the x-ray survival curves are described by

$$-\ln S = \begin{cases} \alpha_x D + \beta_x D^2 & D < D_t \\ \alpha_x D_t + \beta_x D_t^2 + s_{max}(D - D_t) & D > D_t \end{cases}, \tag{2.41}$$

where α_x and β_x are the same as in the LQ model. However, in order to get a better fit to the survival data, the exponent of the cell survival becomes linear when the dose is above a threshold, D_t, with the slope $s_{max} = \alpha_x + 2\beta_x D_t$. Thus, the cell survival has a shoulder before becoming a pure exponential function for doses above D_t.

When the dose deposition is inhomogeneous, as is the case for ions, the dose to the sensitive volumes are described by $D(x, y, z)$ and depends on their position within the cell nucleus. The average number of lethal events in a cell nucleus is then found by

$$\bar{N}_{lethal} = \iiint v\big(D(x, y, z)\big)\, dxdydz = \iiint \frac{-\ln S\big(D(x, y, z)\big)}{V}\, dxdydz. \qquad (2.42)$$

Thus, the LEM model depends only on photon cell survival data and the dose deposition distribution. In LEM, the dose deposition from an ion is not treated as a stochastic distribution of single energy deposits. Instead, the dose deposition around a track is deterministic, and extends radially from the central core of the track. This is because most of the dose from a track is deposited by delta electrons that deposits their energy away from the ions track. Since the density of deltas decline with distance in the transverse direction, so does the dose. The dose is assumed constant within a radius of 10 nm of the track, before it falls off as $1/r^2$. The dose drops to zero at the radius that is equivalent to the maximum range of the delta electrons.

In a later revision, LEM was simplified to reduce the necessary computation power such that it could be used in treatment planning for ion therapy in (Scholz, Kellerer, Kraft-Weyrather, & Kraft, 1997), known as LEM I. A newer version (LEM IV) was presented by Elsässer et al. (2010) that considers that a higher density of complex DSB is created in high LET radiation compared to that of photons, which increases the effectiveness of high LET ions. In a comparison between LEM I and IV, it was found that LEM IV predicted up to 35% higher biological dose at the distal edge in previously radiated patients and about 10% lower dose in the centre region of the treatment field (Gillmann, Jäkel, & Karger, 2019). Presently, the LEM I model is used for calculating the biological dose in ion therapy in Germany as there are not enough clinical evidence that the newer versions are clinically superior (Gillmann et al., 2019)

3. Silicon detectors

Crystalline silicon is a semiconductor that is used for both detectors and microelectronics. Silicon detectors are used for a variety of purposes in medical-, particle- and nuclear physics as well as industrial purposes. They are often used to measure energy deposition, intensity of light and position. The emphasis here is energy deposition measurement in micrometric silicon volumes that can be used for microdosimetry. The chapter contains a short introduction of the properties of silicon detectors, followed by a presentation of different designs of silicon microdosimeters. Finally, the new pixel detector for the CERN ALICE experiment is also presented, which might be used for a novel type of microdosimeter, presented in chapter 9.

3.1 Properties of silicon detectors

This section is a brief presentation on the properties of semiconductors that are important for creating silicon detectors. It is based on (Knoll, 2010, pp. 353-376; Leo, 1994, pp. 215-227; Spieler, 2005, pp. 43-73).

In semiconductors there are energy *bands* where the electron energy levels are so close that they can be considered a continuum and each of these bands can be separated by a region where there are no energy states, called an *energy gap*. The two outermost band structures are the *conduction* and the *valence band*. In the valence band, the electrons are bound to the atoms, and the valence electrons make up the covalent bonds between the atoms in a crystalline material. If an electron in the valence band receives enough energy, it is excited into the conduction band, where it is no longer bound to any one atom and can roam the crystal lattice freely. The valence electrons can be excited into the conduction band by heat and radiation. At room temperature, insulators normally have no electrons in the conduction band, while conductors have electrons in the conduction band at all temperatures.

In silicon at room temperature, the valance band of most atoms will be filled by electrons while some electrons are thermally excited into the conduction band.

Whenever an electron is excited into the conduction band a hole is left in the lattice. This hole can be filled by a neighbouring valence electron which can be interpreted as the hole moving to the previous position of the neighbouring valence electron. The hole can therefore move about the lattice when this is repeated, and the hole can be modelled as a positive particle. If an electric field is applied, the electrons and holes will move in opposite direction, and the current is thus constituted by both moving electrons and holes. In pure silicon there are always equal amounts of electrons and holes.

Free electrons and holes can also recombine when they are near each other, and the rate of recombination depends on the concentration of electrons and holes. Under stable conditions, the charge carrier (electrons and holes) concentration is constant and depends on the temperature. The concentration of electrons and holes in intrinsic silicon at room temperature (300 K) is $n_i \simeq 1.5 \times 10^{10}$ cm^{-3}, whereas the density of silicon atoms is $\sim 10^{22}$ cm^{-3} (Leo, 1994).

However, direct recombination of electrons and holes are rare events and do not lead to significant loss of charge carriers in a detector system. There are always some impurities present in the silicon lattice, and these “alien” atoms can create energy states within the forbidden band gap. Whenever free charge carries fall into these energy states, they become trapped, and can be released back into the conduction band after some time. Alternatively, both an electron and a hole can be trapped in the same energy state leading to an “annihilation” of the two. Similar energy states can also occur in the energy gap by deformation in the silicon lattice, such as vacancies in the lattice or silicon atoms being lodged between lattice points. These deformations can be created several ways but are also the result of radiation damage when the silicon atoms are scattered. These *trapping* and *recombination* centres deteriorate detector performance. Both trapped and recombined charge represent lost charge since they do not participate in the short current pulse output from the detector. The density of traps reduces the lifetime of the charge carries, and the effect of trapping can be reduced by decreasing the charge collection time.

3.1.1 Doping

In pure semiconductors the number of free electrons and holes are equal, but this equilibrium can be changed by adding specific impurity atoms. The controlled adding of impurities is called *doping*. By adding an atom with 5 valence electrons, such as phosphorus, into the lattice there is one extra electron after the 4 covalent bonds are made. This electron sits in an energy state near the conduction band created by the presence of the impurity atom and it is easily excited into the conduction band. Atoms with 5 valence electrons are called donors, and the concentration of free electrons are increased when silicon is doped with donors. In donor doped silicon, the number of holes is also decreased as the large amounts of electrons in the conduction band increase the holes' probability for recombination. Donor doped silicon is known as *n-type* silicon.

A similar effect is achieved by adding impurity atoms with 3 valence atoms, such as boron, which are called *acceptors*. This causes there to be a missing electron in the lattice, and an energy state is created near the valence band. Acceptor doped silicon is known as *p-type* silicon and will have an overweight of holes compared to free electrons.

In n-type silicon the number of electrons in the conduction band is approximately equal to the number of donor atoms. Similarly, the number of holes in p-type silicon is approximately equal to the number of donor atoms. In semiconductor devices there are often both acceptor and donor atoms in the same volume, and it is the majority of impurity atoms that decide if it is p- or n-type silicon. Higher doping concentration increases the amount of free charge carriers and thus increases the conductivity of the semiconductor. Typical doping concentrations is in the range $10^{12} - 10^{18}\ \mathrm{cm}^{-3}$, while the density of silicon atoms are $\sim 10^{22}\ \mathrm{cm}^{-3}$ (Spieler, 2005, p. 56).

3.1.2 PN-junction

Semiconductor diode detectors are made by creating so called *pn-junctions*. A pn-junction is created by forming p- and n-type silicon in close vicinity of each other in the same silicon volume.

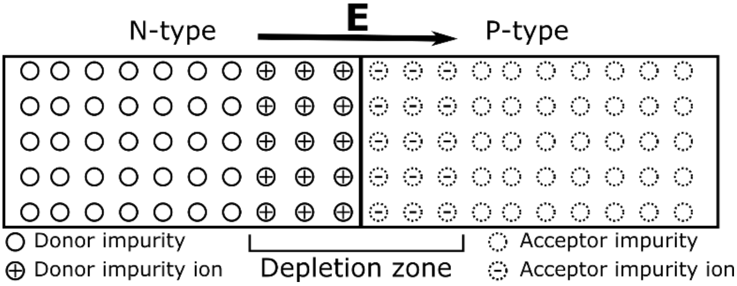

Figure 3.1: Illustration of a pn-junction where the donor and acceptor impurities near the junction have been ionized. The depletion zone covers the volume of ionized impurities. The space charge in the depletion regions create an electric field from the n-type into the p-type silicon. Taken from (Samnøy, 2010) with permission.

As the electrons in the n-type silicon randomly diffuse around, some will diffuse over to the p-side where they have a much higher probability of being captured due to the large concentration of holes. As the n-side loses electrons to the p-side, the n-side becomes positively charged and the p-side becomes negatively charged, which creates a potential difference between the two. This is illustrated in Figure 3.1. When this potential difference reaches a certain magnitude, it stops the electrons and holes in crossing the junction between the p- and n-type silicon. The volume around the junction now contains static charge, *space charge*, and is called the *depletion zone,* which has an electric field from the n-side towards the p-side.

When radiation is deposited in the depletion zone, and electron-hole pairs are produced, the electric field will cause the electrons and holes to move in opposing direction, creating a current that can be detected. The naturally occurring potential difference across the depletion in silicon, V_0, is found by (Gray, Hurst, Lewis, & Meyer, 2009, p. 2)

$$V_0 \simeq 26 \text{ mV} \times \ln \frac{N_A N_D}{n_i^2} \quad for \quad T = 300° \text{ K}, \tag{3.1}$$

where N_A and N_D is the doping concentration of acceptors and donors respectively, and V_0 is typically in the order of 1 V (Leo, 1994).

The potential difference across the depletion zone can be increased by applying an external *reverse bias voltage*, V_B, such that the total voltage across the junction is $V = V_B + V_0$. This increases the depletion depth, such that a larger silicon volume is sensitive to radiation. The depletion zone's penetration depth into the donor doped (W_D) and acceptor doped (W_A) silicon is given by (Gray et al., 2009, p. 4)

$$W_A = \left[\frac{2\epsilon V}{qN_A\left(1+\frac{N_A}{N_D}\right)}\right]^{\frac{1}{2}} \qquad W_D = \left[\frac{2\epsilon V}{qN_D\left(1+\frac{N_D}{N_A}\right)}\right]^{\frac{1}{2}}, \tag{3.2}$$

where ϵ is the permittivity of the silicon, q is the electron charge, and the total depth of the depletion zone is $d = W_A + W_D$. The equations show that when one side is more heavily doped than the other, $N_A \gg N_D$ or $N_A \ll N_D$, the depletion zone primarily extends into the lesser doped side. If enough reverse bias voltage is applied the depletion zone will extend through the entire silicon volume, and the detector becomes *fully depleted*. If the voltage is increased beyond the *depletion voltage*, the electric field strength across the depletion zone increases which increases the velocity of the charge carriers. This decreases the collection time and thus lowers the probability of trapping and recombination.

The depletion region has similar characteristics as a capacitor, and the capacitance for a planar junction is (Leo, 1994)

$$C = A\frac{\epsilon}{d}. \tag{3.3}$$

An increase in capacitance also increases the electronics noise and should be kept as small as possible. The formula shows that increasing the depletion depth, d, decreases the capacitance.

The current flowing through the detector when no radiation is present is called *leakage current* and is a source of noise in the detection system. The leakage current increases with increasing bias voltage and can be lowered by cooling the detector.

Impurities and lattice defects also increase the leakage current, thus an increase in leakage current after radiating is a sign of radiation damage.

3.2 Read out electronics

The charge liberated in silicon and gas detectors by radiation has the form of a short current pulse and the role of the read-out electronics is to measure this charge with as little added noise as possible. The read-out electronics is generally split into the analogue (front-end) and digital electronics. The front-end electronics shapes and amplifies the current signal from the detector into a signal that can be digitized for further processing and storage.

When discrete amplifiers are used, they are usually split into a *charge sensitive preamplifier* (CSP) and a *shaping amplifier* and a typical schematic of the electronics is shown in Figure 3.2.

The current pulse from the detector is integrated by the CSP and the output is a voltage step pulse with a slow logarithmic decay. The CSP usually has an input for detector bias voltage and test signal from a signal generator. When a voltage step signal is applied to the test input from a signal generator, it produces a charge at the input node that is equal to the product of the CSP's test capacitance and the amplitude of the voltage step. Thus, a signal generator can be used to mimic a detector signal, which is used for testing and calibration.

Since the CSP is the first amplification stage it is particularly important that the noise input to the CSP and that the noise generated by the CSP is as small as possible since this noise will be amplified by both the CSP and the shaping amplifier. The noise depends mostly on the input capacitance to the CSP that mainly comes from the detector and the cable connecting the detector and CSP.

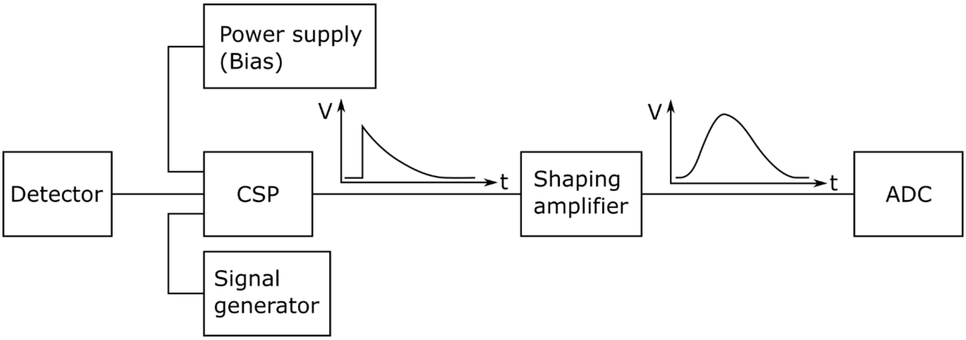

Figure 3.2: Schematic of discrete components typically used to measure single event energy depositions. The voltage step signal output from the CSP and semi-gaussian signal output from the shaping amplifier is shown.

The shaping amplifier further amplifies the voltage signal and shapes the signal to a semi-gaussian signal. The semi-gaussian shape allows the signal to return to baseline faster than the slow logarithmic decay of the CSP. This avoids overlapping pulses (pile-up) at high detection rates. The semi-gaussian shape is usually created by first applying a high pass filter followed by a series of low pass filters but can also be created by an active circuit. While the CSP usually has fixed amplification, the amplification of the shaper can be tuned to fit the input range of the analogue to digital converter (ADC) that digitizes the signal. The width of the semi-gaussian pulse depends on the time constant (shaping time) of the high and low pass filters and can often be changed. Since the shaping amplifier is usually a series of filters, they will also filter out noise.

In microdosimetry, the ADC is usually self-triggering, meaning that it will start to digitize a pre-set number of samples whenever the input voltage exceeds a voltage threshold. The voltage threshold is equivalent to the detection threshold, which is the lowest event that can be detected. The threshold should be set as low as possible to detect all radiation events in the detector. However, the random electronic noise can also trigger the ADC and produce false events, and thus the noise sets a lower limit of detectable signals.

By splitting the detector into many small detector elements and creating individual front-end electronics for each detector element close to the detector, three things are achieved. Firstly, it is possible to know which detector element that were hit, giving much better spatial resolution. Secondly, the detector can handle very high count rates from intense beams without suffering from pile-up. Thirdly, the dark current, detector element capacitance and cable capacitance is significantly reduced, resulting in very little noise. This type of detector and front-end electronics combination can be achieved by fabricating a detector and readout chip pair that is connected by micrometric solder *bumps* connecting the individual detector element with its electronics (L. Rossi, Fischer, Rohe, & Wermes, 2006, pp. 203-218). It is also achieved in *monolithic detectors*, where the read out circuitry and the sensitive detector elements are fabricated on the same silicon substrate (see section 3.4).

3.3 Silicon detectors for microdosimetry

Silicon detectors for microdosimetry are being developed as an alternative to TEPCs to reduce some of the TEPCs shortcomings, see Rosenfeld (2016). However, silicon microdosimeters are not superior to TEPCs and have their own shortcomings that must be considered when used. An introduction is given here, and the properties of silicon microdosimeters are compared to those of the TEPC.

Since silicon microdosimeters have true micrometric SVs they do not suffer from wall effects. The small SV also results in a very small cross-sectional area such that the silicon detector can handle much higher fluxes than TEPCs without suffering from pile-up or events during detector dead time. The small SV also gives much higher spatial resolution than TEPCs. Furthermore, there is no need for a gas system, which is both expensive and bulky, and the bias voltage of silicon microdosimeters are typically 5-20 V compared to a few hundred volts to 1000 V for TEPCs.

3.3.1 Signal formation

The average energy necessary to create mobile charge carriers in silicon is 3.62 eV at room temperature and is independent on radiation type and energy (Klein, 1968). The average energy necessary to produce electron ion pairs in TE gas depends on both radiation type and energy, and is typically 30-40 eV, but can be above 100 eV for slow moving charged particles (IAEA, 1995, pp. 560 - 599). Thus, there are produced more charge carriers from radiation in silicon than in TE gas i.e. there are more relevant transfer points in a silicon volume than in a TE gas volume of equivalent size. However, the charge multiplication due to the avalanche effect in TEPCs increases the charge output significantly and more charge is produced in TEPCs compared to silicon in equivalent volumes. TEPC generally has higher signal to noise ratio (SNR) than silicon detectors when similar cables and preamplifiers are used, and thus has lower detection threshold. The lower threshold is seen in a study by Agosteo et al. (2010), where a silicon detector is compared to a TEPC (De Nardo, Moro, et al., 2004) in a proton medical beamline. The silicon microdosimeter has cylindrical SVs that are 2 μm deep and 9 μm in diameter, while the TEPC simulates a 1 μm diameter site. The lower detection threshold due to noise is 6 keV/μm for the silicon microdosimeter, while it is 0.2 keV/μm for the TEPC. Thus, the silicon microdosimeters needs a larger SV to detect low LET particles, but a larger SV might also make the microdosimeter less relevant for biological models. By bump-bonding silicon microdosimeters to its readout electronics or by designing a monolithic microdosimeter with front-end electronics, the detection threshold can be significantly reduced, allowing for smaller SVs with lower detection threshold.

3.3.2 Tissue Equivalence

Silicon is not tissue equivalent and it is necessary to *correct* the measurements from a silicon microdosimeter such that they become tissue equivalent. Two methods have been used to correct single events measurement from silicon microdosimeters, where one is based on stopping power tables and the other is based on Monte Carlo (MC) simulations.

In Bradley and Rosenfeld (1998) the tissue corrected energy deposition for a single ion, $\epsilon_{1,T}$, was calculated by

$$\epsilon_{1,T} = \epsilon_{1,Si} \cdot \frac{1}{E_{max}} \int_{0}^{E_{max}} \frac{S_T(E)}{S_{Si}(E)} dE = \xi \cdot \epsilon_{1,Si}, \tag{3.4}$$

where S_T and S_{Si} is the stopping power for tissue and silicon respectively for ion energy, E, while E_{max} is the maximum ion energy and $\epsilon_{1,Si}$ is the single event energy deposition in the silicon SV. ξ is the tissue correction factor and is an average over the relevant energy range for a specific particle type. ξ must be calculated for every particle species present and a weighted average of these is used to transfer to tissue equivalent energy deposition. Figure 3.3 shows that the stopping power ratio between tissue and silicon for protons and alpha particles changes slowly above 10 MeV/u.

This method was modified by using a two-stage silicon detector, a ΔE/E telescope (Agosteo et al., 2010; Agosteo et al., 2008; Agosteo et al., 2009). The ΔE/E telescope has an array of micrometric SVs on top (ΔE-stage) used for microdosimetry with a 500 µm deep detector underneath (E-stage) that could measure total energy when the track was shorter than ~500 µm. A comparison between the ΔE/E telescope and a TEPC in a clinical 62 MeV proton beamlines with a spread out Bragg peak (SOBP) was conducted by Agosteo et al (2010). The measurments from the silicon microdosimeter was tissue corrected by using equation (3.4) when the proton energy was above 6.5 MeV. However, for protons below 6.5 MeV that stop inside the E-stage, the protons' indivudual stopping power ratio was used as a correction factor. This method resultet in little deviation between the results from the silicon microdosimeter and the TEPC. However, when equation (3.4) was used for protons below 6.5 MeV, the deviation from TEPC results were severe, indicating that the tissue correction method produces large errors for low energy protons.

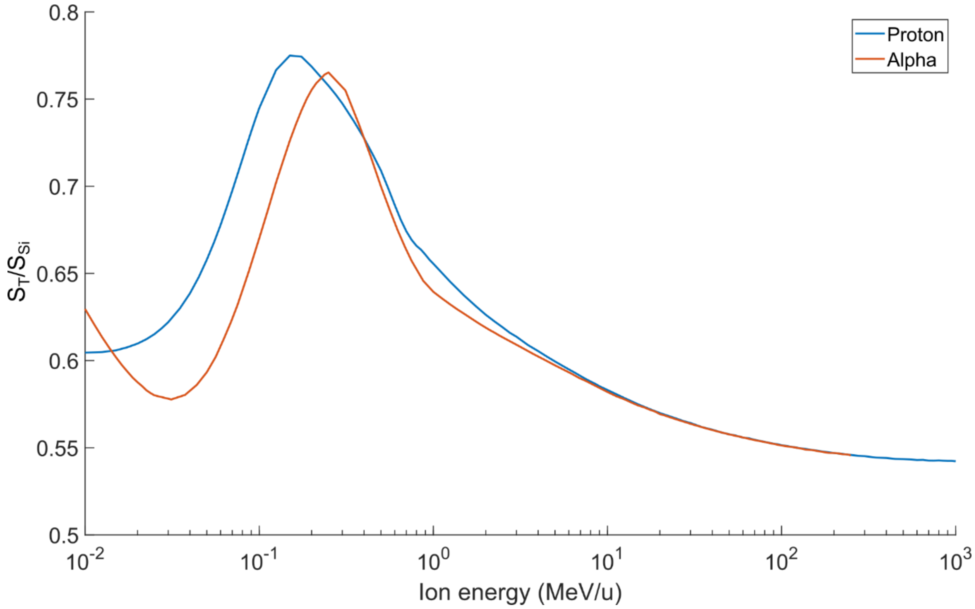

Figure 3.3: Ratio of stopping power to tissue over silicon as a function of ion energy for protons and alpha particles. Created from PSTAR and ASTAR data (Berger et al., 2017) where the material "skeletal muscle" from ICRP is used for tissue.

As high energy ions generate a variety of secondary particles it is difficult to find the weighted average ξ. This is challenging when estimating microdosimetric spectra along a Bragg curve, where the type, fraction and energies of the secondary particles change with depth. MC simulations have in a previous study been used to calculate the lineal energy in silicon and tissue composed microdosimeters (Bolst, Guatelli, et al., 2017). In that work, the cylindrical SVs of the simulated silicon composed detector were modelled after the real detector, with equal height and radius, while the radius and height of a tissue composed SVs were $1/\kappa$ times larger. The aim was to find the correction factor, κ, giving approximately the same energy deposition in silicon and tissue at all depths of the Bragg curve, i.e. giving $\epsilon_{1,Si} \approx \epsilon_{1,T}$. The tissue equivalent lineal energy, y_T, is then

$$y_T = \frac{\overline{l_{Si}}}{\overline{l_T}} y_S = \kappa \cdot y_{Si}, \tag{3.5}$$

where y_{Si} is the lineal energy to the silicon SV, while $\overline{l_{Si}}$ and $\overline{l_T}$ are the mean chord lengths in the silicon and tissue SVs respectively. This method has been used to correct measurements from silicon microdosimeters in several proton and ^{12}C medical beamlines (Bolst, Tran, et al., 2017; Debrot et al., 2018; L. T. Tran, Chartier, Bolst, et al., 2018; Linh T. Tran et al., 2017; L. T. Tran, Chartier, Prokopovich, et al., 2018).

It is expected that any constant correction factor will yield large errors for low velocity ions. A novel tissue correction function for protons is therefore explored in chapter 7 that do not need a two-stage detector such as the ΔE/E telescope. The novel function is used to correct measurements in a microdosimetric characterization of a low energy proton beamline used for radiobiological experiments in chapter 8.

3.3.3 Definition of the sensitive volume (SV)

The charge collection across the SV of any microdosimeter must be homogeneous such that the measured energy deposition does not depend on the position within the SV. Inhomogeneous charge collection increases the uncertainties of the measured energy deposition and widens the single event spectra. Furthermore, no charge should be collected from outside the SV, as this would diffuse the border of the SV, giving a poorly defined SV. Poorly defined SVs yield partial charge collection from outside the SV, which is measured as lower energy events. Poorly defined SVs also increase the uncertainty of the effective mass and mean chord length which is necessary for calculating the specific and lineal energy.

Silicon microdosimeters have usually been fabricated on silicon on insulator (SOI) wafers such that the charge is only collected from the top *device layer*, which creates a well-defined border in the depth direction.

In conventional or planar fabrication of silicon detectors and microelectronics, doped patterns are created at the surface of the silicon that extends into the silicon and forms the necessary pn-junctions (Spieler, 2005, pp. 418-432). In conventional detector fabrication the high concentration dopants do not extend more than a few μm into the silicon. Diffusing dopants deep into the silicon causes large gradients in dopant concentration which also causes a sensitivity gradient.

The ion beam induced charge collection (IBICC) technique has proven to be an effective way of determining the position sensitivity of the microdosimeter. The IBICC technique uses a monoenergetic ion microbeam with diameter of 1 μm or less to scan the surface of the microdosimeters. By recoding the single event pulse height in conjunction with the beam position it is possible to produce a sensitivity map of the devices.

Figure 3.4 shows the design of a silicon detector used for microdosimetry that was characterized by Bradley (2000) where all the diodes (SVs) on the detector were connected in parallel. Results from microbeam experiments showed that the detector diodes shared charge produced between them (crosstalk) and an inhomogeneous charge collection that was position sensitive. The maximum charge collection was under the N^+ silicon, while the minimum was below the P^+ silicon.

Another design is shown in Figure 3.5 where each diode has a guard ring (GR) to reduce the crosstalk between them and to better define the SV. The SV is defined as the volume between the central N^+ electrode and surrounding P^+ ring, where the guard ring structure collects the charge produced outside the P^+ ring. However, for thick SOI layers the electric field becomes weaker at higher depths, which causes more diffusion of the charge carriers before they are collected.

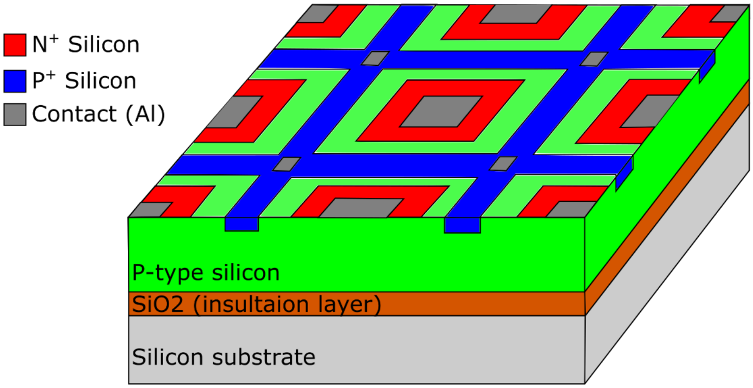

Figure 3.4: Illustration of an early silicon microdosimeter where all the diodes (N+) were connected in parallel. The detector showed inhomogeneous charge collection. The maximum charge collection was below the N^+ silicon while the minimum was below the P^+ silicon. Illustration reproduced from Bradley (2000).

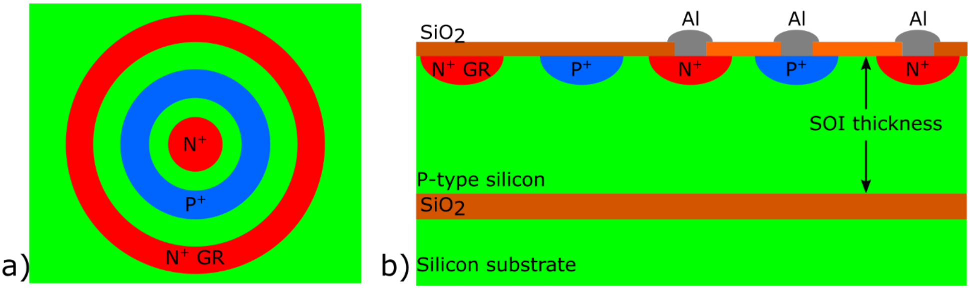

Figure 3.5: Illustrations of a single diode with a guard ring (GR) in a silicon microdosimeter. a) shows a top view of the dopants structure, and b) shows a cross section view with the oxide layer and aluminium contacts. The microdosimeter consists of an array of diodes that are connected in parallel. The illustration is reproduced from Lai et al. (2008).

Thus, the sensitivity of microdosimeters with thick SOI layers is less homogeneous than those with thin SOI layers. Several microdosimeter designs with guard rings have been produced and tested, and microbeam experiments show well defined SVs when the SOI layer is 2 µm thick (Lai et al., 2008).

Well defined SVs without crosstalk is possible by etching away the silicon surrounding the SVs. However, the metal layering that connects the diodes must be deposited on a flat surface to ensure good connectivity, which means that the diodes cannot be completely free standing. The “bridge” microdosimeter (Figure 3.6) has etched away most of the silicon surrounding the diodes, but left a “bridge” of silicon between the diodes for the metal layer (L. T. Tran et al., 2015). Due to difficulties in etching a straight wall along the diodes, the walls become slightly skewed, and out of the 10 µm deep SOI layer, only 5 µm was etched. Results from microbeam experiments show a homogeneous charge collection at the centre, but with a slight sensitivity gradient around the edges of the diodes. The bridges were also seen to be slightly sensitive.

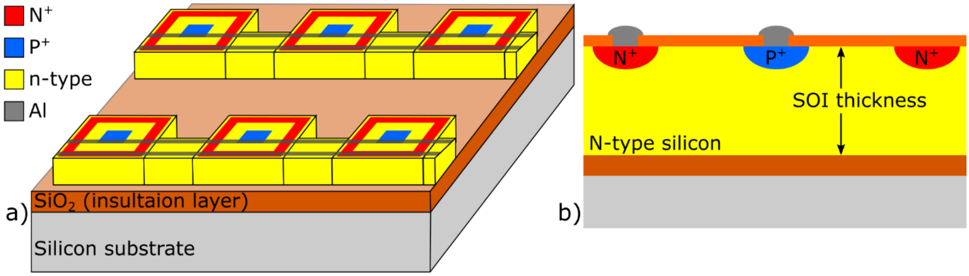

Figure 3.6: Illustration of the “bridge” microdosimeter that is 10 µm thick with a front area of 30 x 30 µm^2. The silicon surrounding the diodes area is etched, but a bridge is left for the metal layer (Al) that connects the diodes. The illustration is reproduced from L. T. Tran et al. (2015).

3.3.4 The 3D SOI “mushroom” microdosimeter

The microdosimeter characterized and used in this work is a 3D silicon detector (S. I. Parker, Kenney, & Segal, 1997) with active edges (Kenney et al., 2006), and produced at MiNaLab, SINTEF. The microdosimeter consists of an array of diodes that are embedded in a 10 µm deep p-type SOI layer, seen in Figure 3.7. The diodes were fabricated by etching a circular deep narrow trench through the entire device layer using deep reactive ion etching (Kok et al., 2009). The trench walls were then doped by boron gas diffusion (P$^+$) such that the trenches function as an electrode (active edge). An N$^+$ electrode was formed at the centre of the diode which is used for signal extraction and biasing, where the even and odd rows of N$^+$ electrodes are connected in parallel. The 3D doped trenches isolate the diodes such that no liberated charge is collected from the outside, giving well-defined SVs. Furthermore, the 3D design has low depletion voltage and swift charge collection compared to a planar design.

Two different diode designs were fabricated and are called *trenched planar structure* (Figure 3.8) and *trenched 3D structure* (Figure 3.9). The trenched planar structure has a trench that encompasses the entire diode that is doped (P$^+$) and filled with doped (P$^+$) polycrystalline silicon (polysilicon). The central N$^+$ electrode is doped by ion implantation and sits at the surface (planar process). The polysilicon filling planarize the surface, which allows the aluminium to pass over the diode to connect the central N$^+$ electrode.

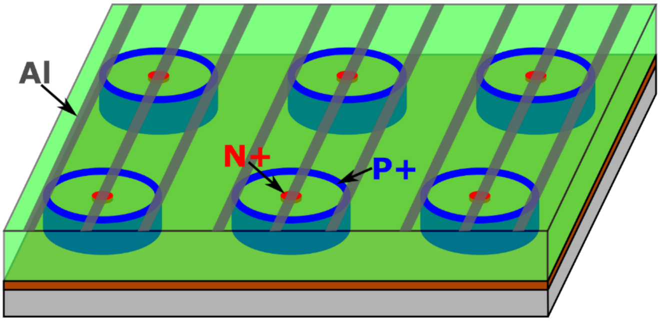

Figure 3.7: Principle sketch of the 3D SOI "mushroom" microdosimeters. The diodes are isolated by the etched and doped (P^{+}) trench that surrounds the diodes. The central N^{+} column is used for signal extraction and biasing. The even and odd columns are connected in parallel.

The trenched 3D structure also has doped trenches, but they are not filled. The trenches do not encompass the entire diode such that a "bridge" is left on two opposite sides of the diode that allow the aluminium to pass over the diode in order to connect the central N^{+} electrode. The central N^{+} electrode in the trenched 3D structure is an etched and gas doped cylinder that extends through the entire device layer. It is expected that the trenched 3D structure will be somewhat sensitive outside the opening in the trenches.

The microdosimeters were fabricated on 10 µm SOI, and the two structures come in two sizes where the diameter of the circular trench was designed to be 25 µm (small) and 34 µm (large). Scanning electron microscopy (SEM) of a cross section cut of a large trenched 3D structure showed 30 µm diameter with 9.1 µm height (L. T. Tran, Chartier, Prokopovich, et al., 2018). The difference in size between the design and actual size is well known and was considered in the design process. The microdosimeter chip with large diodes has 33 x 33 SVs with 75 µm in both directions, covering an area of 2.40 x 2.40 mm^{2}, while the microdosimeter with small diodes has 50 x 50 SVs with 50 µm pitch covering 2.45 x 2.45 mm^{2}.

The silicon between the diodes on a few trenched planar structures has been etched away and replaced by a polyimide through spin coating. This has been done to make the microdosimeter more tissue equivalent, as polyimide has an atomic composition similar to tissue.

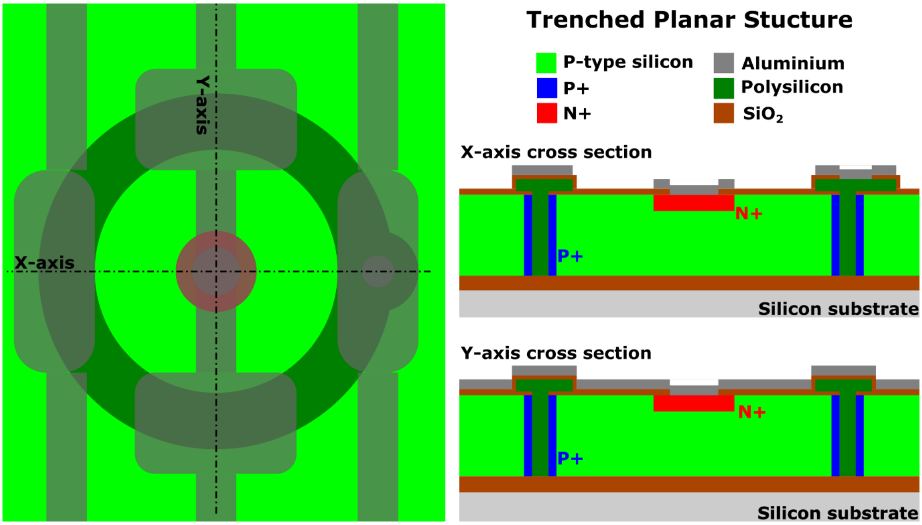

Figure 3.8: Top and cross sectional view of the “trenched planar structure” where the SiO_2 is removed and the aluminium is made partially transparent in the top view. The trenches encompass the entire diode and are filled with polysilicon, while the central N^+ electrode is planar. The polysilicon filling planarize the surface which allows the aluminium to pass over the diode to connect the central N^+ electrode.

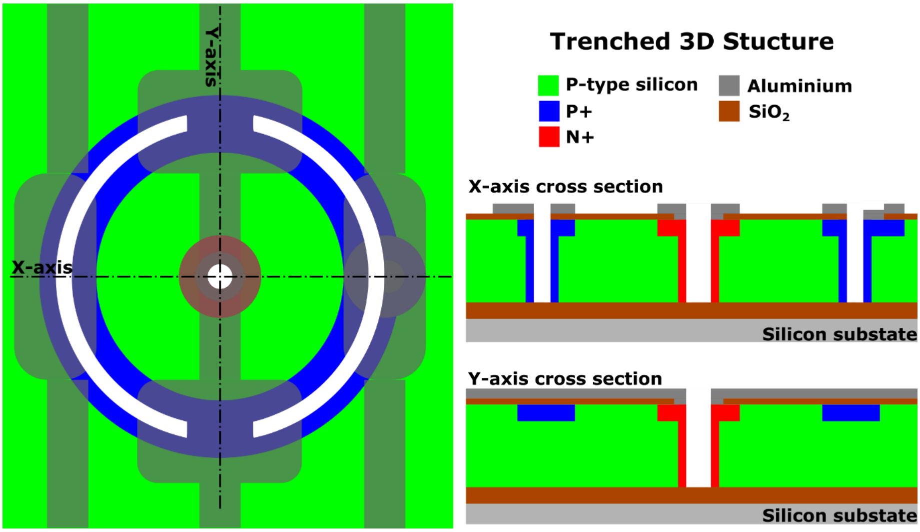

Figure 3.9: Top and cross sectional view of the “trenched 3D structure” where the SiO_2 is removed and the aluminium is made partially transparent in the top view. The central N^+ electrode is an etched and doped column (3D), while the trenches are doped but not filled. Since the trenches are not filled, a “bridge” is left on two sides of the diode that allow the aluminium to pass over the diode to connect the central N^+ electrode.

The printed circuit board (PCB) with a microdosimeter chip wire bonded to it can be seen in Figure 3.10 along with a photomicrograph of the microdosimeter. The PCB was made by Øyvind Lye and is presented in his master thesis (Lye, 2016). The PCB was made very general to facilitate for several types of connections and filter circuits. The central N^+ electrodes of the odd and even rows and the P^+ trench of all the diodes are connected through LEMO cables.

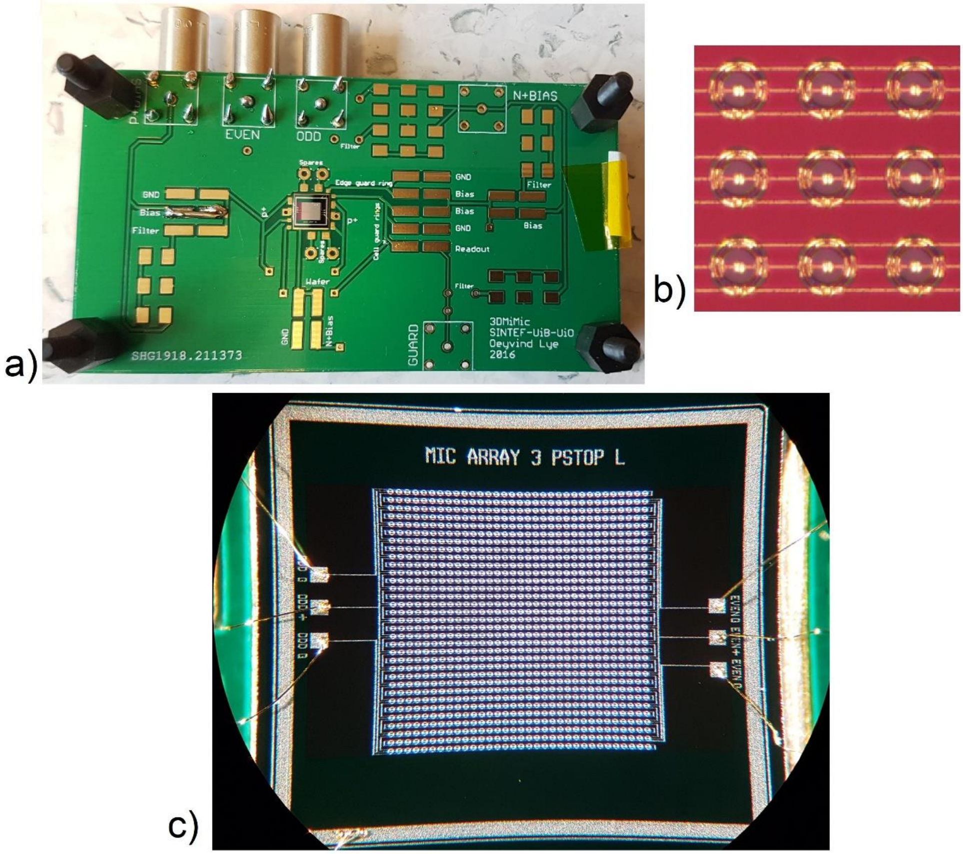

Figure 3.10: a) Picture of the printed microdosimeter chip bonded to a PCB.
b) Photomicrograph of the microdosimeter showing 9 diodes.
c) Photomicrograph of the entire microdosimeter chip with wire bonds.

3.4 ALPIDE

The ALPIDE is a monolithic active pixel sensor (MAPS) where the readout electronics and the sensitive pixels are fabricated on the same silicon chip (Kim et al., 2016; Šuljić, 2016). The detector measures the position of charged particles as they cross the detector and was developed for the inner tracking system (ITS) in the ALICE experiment at CERN.

The ALPIDE is also being used for a proton computer tomography (proton CT) currently under development at the University of Bergen (UiB) and Western Norway University of Applied Sciences (HVL) (Pettersen, 2018; Pettersen et al., 2019; Pettersen et al., 2017). The proton CT aims to lower the stopping power uncertainty of protons traversing patients such that the range uncertainty in proton therapy can be reduced.

The ALPIDE or future generation of MAPS is also considered for a novel tracking microdosimeter where all particles in a radiation field are tracked with micrometric resolution within the detector volume. This is discussed in chapter 9.

Design specifications

The dimensions of a single ALPIDE chip is 15 x 30 mm^2 with 512 rows and 1024 columns of pixels, where the pixel pitch is 29.24 x 26.88 μm^2. The detector fabrication is based on the TowerJazz 180 nm CMOS imaging process, seen in Figure 3.11, which allows for the fabrication of both NMOS and PMOS transistors at the surface of the silicon SV (Kim et al., 2016; Šuljić, 2016). Thus, advanced circuitry can be designed on the same substrate as the SV, and each pixel has its own front-end electronics with amplification and discrimination. The extremely low RMS noise of 3.9 e^- allows for thresholds below 100 e^- such that minimum ionizing particles (MIP) can be detected (Aglieri Rinella, 2017; Šuljić, 2016). The low noise is possible due to the small input capacitance at the front-end electronics which is a result of the small structure size of the collection diode and the short distance between the collection diode and the electronics. The readout is hit driven, i.e. only addresses of hit pixels are sent to the periphery, which significantly reduces the data rate.

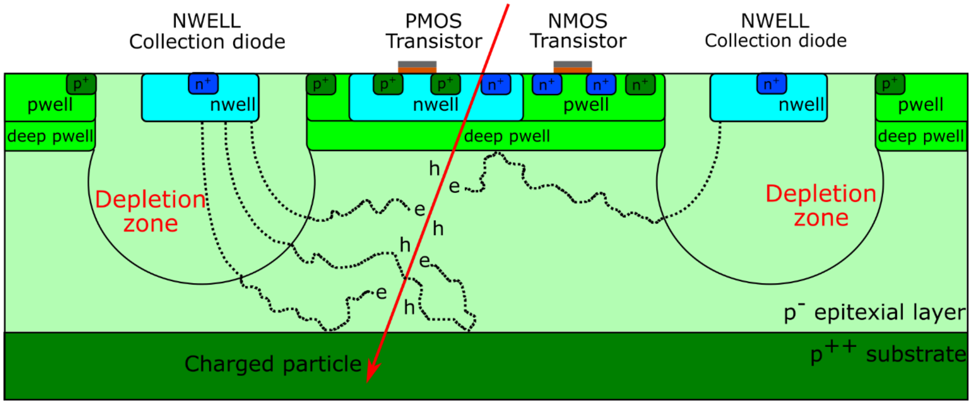

Figure 3.11: Generic cross section of a MAPS created with the Tower Jazz 180 nm CMOS imaging process. The epitaxial layer (p^-) is 18-30 µm thick and the transistors for the circuitry is fabricated close to its surface. The figure is inspired by (Kim et al., 2016; Šuljić, 2016).

The SV and readout circuitry are created in a p-type epitaxial layer which is grown on a P^+ substrate, as seen in Figure 3.11. Several epitaxial layer thicknesses between 18 and 30 µm have been fabricated and tested (Aglieri Rinella, 2017). A nwell forms a pn-junction (collection diode) with a depletion zone extending into the epitaxial layer, necessary to collect the liberated charge in the epitaxial layer. The electrons liberated in the epitaxial layer (p^-) have long lifetimes and are collected once entering the depletion zone, while liberated electrons in the more heavily doped p- and nwells have very short lifetimes and will recombine instantly. The charge is shared between the collection nodes, and several pixels can thus trigger a hit from a single hit, generating a *cluster* of neighbouring triggered pixels. Negative bias can be applied to the bulk which increases the depletion zone, which yields faster charge collection and lower capacitance, thus increasing the SNR. Applying bias will also result in less charge sharing between the collection nodes which reduces the cluster size.

4. Monte Carlo simulation

The experiments conducted in this thesis work have also been modelled and simulated through Monte Carlo (MC) simulations. This has been done to better understand the experimental findings, as part of the calibration procedures, and to create an exact model of the microdosimeter that can be used to predict the detector response in other radiation fields. MC simulations were also used to create the tissue correction function presented in chapter 7.

4.1 GATE and Geant4 simulations tools

In the work presented here, the MC software GATE (Geant4 Application for Emission Tomography) has been used. GATE was originally created for simulating positron emission tomography (PET) and single-photon emission computed tomography (SPECT), but has later been extended to facilitate other imaging modules and detectors as well as radiotherapy (Jan et al., 2011; Jan et al., 2004; "Open Gate Collaboration," 2020). GATE is an application of the C++ MC toolkit Geant4 (GEometry ANd Tracking) ("Geant4," 2020; Strulab, Santin, Lazaro, Breton, & Morel, 2003), created to simplify Geant4 simulations, as GATE uses simple macro files to set up the simulations instead of C++ programming.

GATE/Geant4 simulates the passage of particles through matter where they undergo a very high number of stochastics interactions between the particles and matter. The simulations follow all the generated individual particles from their creation until they stop, thereby mimicking how real particles behave in matter.

Complex geometries can be modelled that can be constructed through many smaller simpler geometries (e.g. boxes, cylinders, spheres…), by importing STL files generated by CAD software or by importing DICOM images from CT scans and other imaging modalities. This makes it possible to model complete experimental setups, such as beamlines, patients, phantoms, absorbers, detectors, and other relevant objects.

The user can manually select which physics processes that are possible in the simulation. However, this is time consuming and demands a high level of expertise from the user. The user can also import *physics lists* from Geant4 that contains models of the processes that the particles can undergo. The level of detail differs between the physics lists, where the more detailed also demand more CPU power, and slows down the simulation. Thus, the user must balance the necessary precision in the simulation against simulation time or statistics. There are two main categories of physics lists: electromagnetic processes and hadronic processes.

Sources of radiation can be generated to simulate beams and radioactive sources. The radiation can be emitted from within a 3D object or a 2D surface and the particle type, energy distribution, beam shape distribution and angular distribution are all easily modified.

Geant4 transports the particles through the simulations in *steps* with finite *step lengths*, instead of using a continuous process to lower CPU time. Instead of regarding energy loss due to electronic collisions as individual collisions, the loss and loss fluctuation is calculated along a step (Bethe theory) to reduce CPU time. The same is done with multiple Coulomb scattering, where the effect is calculated for each step. The possibility of discrete events is calculated for all possible processes for each step, such as production of delta rays or nuclear reactions. Short step lengths will generally increase the accuracy of the simulation but will also slow it down. To balance the need for CPU power and simulation accuracy, each possible process proposes a step length where the shortest proposition is chosen. However, the user can set a maximum step length for each object in the simulation, and the step length cannot be longer than the distance to the border of the object that the particle is currently within.

Several processes can produce secondary particles that will also be tracked until they stop. However, to lower simulation time, *production cut*s are set that do not allow the production of secondaries below a certain energy threshold, and all energy lost that does not produce a secondary is deposited locally. In GATE/Geant4 the production cuts are set as ranges that are calculated into energy cuts, which depends on particle type and material. The production cuts can be set for individual volumes and for particle types and are very important when the user balances the need for accuracy and CPU power.

When detector geometries are implemented the user can specify which volumes that are sensitive to radiations (SV), where information regarding radiation interactions are written to file. In GATE, the particle type, energy deposition, position, and time of each step within the SV can be written to file in a *hit file*. The hit files can become very large, and as an alternative the energy deposition, position and time within the SV can be written to file for every event instead of every step, in a *singles file*.

4.2 GATE model of the 3D SOI “mushroom” microdosimeter

In this thesis work, GATE v8.1 running on Geant4 v10.4 patch 2 was used for simulations. The physics list used for hadron interactions was QGSP_BIC_HP which gives increased accuracy for low energy neutrons (< 20 MeV), while the Livermore physics lists was used for electromagnetic (EM) processes which gives increased accuracy for photon and electron interactions compared to the standard EM physics list. The Livermore physics list also allows for production cuts for photons and electrons as low as 250 eV compared to 1000 eV for the standard EM list.

A precise model of the trenched planar structure (Figure 3.8) was created in GATE and can be seen in Figure 4.1. The silicon volume between the central electrode and the doped trenches is defined as the sensitive volume, while the highly doped electrodes themselves are insensitive as ion pairs created here immediately recombines. The polysilicon and doped regions are simply simulated as pure silicon as the fraction of dopants is several orders of magnitude lower than the density of silicon atoms.

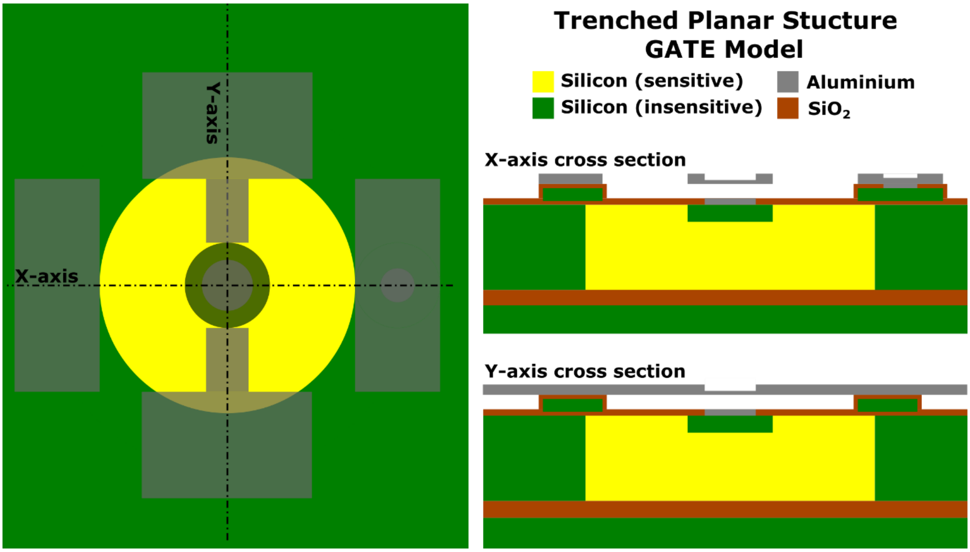

Figure 4.1: GATE model of trenched planar structure shown in Figure 3.8. The region between the central N^+ electrode and P^+ trenches is defined as the sensitive volume. The highly doped regions are modelled as pure silicon which is also insensitive to radiation.

The model has been made such that the dimensions of the SV and the different layers of silicon, aluminium and silicon dioxide can be changed by simply setting a new value without creating empty space between the geometries. This makes it easy to test different sizes of the SV and thicknesses of the overlying layers to see what best fits the experimental results.

GATE does not allow objects to overlap and cannot create an object that is a union or subtraction of several geometries. This has led to two minor geometrical simplifications when the microdosimeter was modelled. Firstly, the aluminium layer is positioned on top of the highest positioned SiO_2 layer in the simulation model as it would otherwise have to intersect with the polysilicon sticking up above the surface around the trenches. This creates a 1-2 µm gap between the aluminium and the SiO_2 layer above the centre of the SV. This gap is “filled” with vacuum such that no scattering can occur in this gap. Secondly, the aluminium strip along the y-axis (Figure 4.1 top view) does not conform to the central aluminium circle as this would demand a union of two shapes. This creates four small openings in the aluminium.

These simplifications in the MC model is assumed to have little influence and should not be noticeable in the energy deposition spectra produced by the simulations.

The production cuts in the simulations presented was set to 250 eV within the SVs, the surrounding silicon volume, and the overlying layers of SiO_2 and aluminium to ensure accurate results. The production cuts further away from the microdosimeter are generally higher to speed up the simulation and has been selected such that secondaries are only produced when they can reach the SVs.

5. Basic characterization of microdosimeters

Four slightly different microdosimeter designs of the trenched planar structure (Figure 3.8) were characterized, two with large (34 µm) and two with small diodes (25 µm). One large and one small microdosimeter have had most of the silicon between diodes replaced with polyimide, while the other small and large microdosimeter were left unetched. The four different devices are denoted as:

- Large standard, L_{st}
- Small standard, S_{St}
- Large with polyimide, L_{Poly}
- Small with polyimide, S_{Poly}

The dark current and capacitance were measured as a function of bias voltage (I-V & C-V) for all four microdosimeters. The microdosimeters were also used to measure the spectra from an alpha source and several soft photon sources with energies between 8 and 60 keV. The results were compared with MC simulations to better understand the results, and to benchmark the simulations toolkit and model for microdosimetry.

The soft photon measurements were conducted as a low energy calibration from photoelectrons that lose all their energy within a single SV. They also serve as a benchmark of the simulations with respect to low energy photons and electrons.

The alpha source measurements were conducted in vacuum to reduce the uncertainty in particle energy at the detector surface. Measurements with a thin absorber between the microdosimeter and the alpha source were also conducted such that the alpha particles would stop within the SVs. This was done to estimate the thickness of the various layers on top of the SVs, as particles passing through thick layers would deposit less energy than those passing none.

5.1 Setup & Method

5.1.1 I-V and C-V

A Keithley 2635A SourceMeter was used for biasing and current measurement when recording the I-V curve and was used for biasing during the C-V measurement. A HP 4263B LCR meter was used for the capacitance measurement when the C-V curve was recorded.

The I-V curve was measured for voltages between 0 and 100 V with steps of 0.5 V with a 5 second wait time between each voltage step to allow the current to settle before it was measured. The C-V curve was measured for voltages between 0 and 20 V with steps of 0.5 V with a 5 second wait time between voltage steps.

5.1.2 Readout electronics for measurements of single event energy deposition

The readout electronics for single event measurements were connected as shown in Figure 3.2. The signals from the microdosimeters and an Ortec Ultra PIN diode detector for calibration were amplified by an Amptek A250CF CoolFET CSP and a Cremat CR-S-1µs shaping amplifier with 1 µs shaping time. A Keithley 2635A SourceMeter was used for biasing, and 20 V bias voltage was used. The signal output from the shaping amplifier was digitized by a SP Devices ADQ14 analogue to digital converter (ADC) with a PCI-Express interface to a desktop computer. A LabVIEW program was used for signal processing and the pulse height, time, and the full width at half maxima (FWHM) for every event was written to file. A digital low pass filter was applied to the signal for a slight reduction in noise. An Agilent/Keysight 33250A 80 MHz signal generator was used for signal testing and calibration.

The Ortec Ultra PIN diode detector used for calibrations is manufactured for spectroscopy and has 100% charge collection efficiency (CCE) for alpha particles and just 50 nm of entrance window (dead layer) according to the vendor. The detector was used for calibration and CCE estimation. The procedures for this are given in the sections below.

5.1.3 Soft photon measurements

A variable energy X-ray source from The Radiochemical Centre Amersham and an ^{241}Am gamma source (59.54 keV) were used to irradiate the microdosimeter. The variable X-ray source contained 6 different elements that were radiated by an ^{241}Am source, producing characteristic X-rays. The energy and relative intensity of the distinct X-ray emission lines from each of the elements is shown in Table 5-1, where only the K-shell emission lines are shown as only these have energy above detection threshold.

The radioactive source and elements in the variable X-ray source were all within the same metal container, and all the elements were continuously irradiated. The container had an opening for the elements with a sliding switch that selected which of the elements were at the opening. Thus, the measured X-ray spectra will contain traces of the shielded sources along with the selected source at the opening. This was not the case when the microdosimeters were irradiated with the ^{241}Am 59.54 keV gamma source as this source was used alone. However, ^{241}Am sources do have several X-ray spectral lines, but these were not simulated since the source had unknown thickness which made it difficult to estimate the intensities of the different energies at the source surface.

Table 5-1: Energy (keV) emitted by the X-ray sources used in the experiment, where the intensity relative to the strongest line (100) is given in parenthesis. The data is taken from (Thompson et al., 2009). In addition to these 6 X-ray sources, an ^{241}Am photon source with 59.54 keV gamma emission was also used.

	Cu (keV)	**Rb** (keV)	**Mo** (keV)	**Ag** (keV)	**Ba** (keV)	**Tb** (keV)
Kα$_2$	8.03 (51)	13.34 (52)	17.37 (52)	21.99 (53)	31.82 (54)	43.74 (56)
Kα$_1$	8.05 (100)	13.40 (100)	17.48 (100)	22.16 (100)	32.19 (100)	44.48 (100)
Kβ$_3$	8.91 (17)	14.95 (7)	19.59 (8)	24.91 (9)	36.30 (10)	50.23 (10)
Kβ$_1$		14.96 (14)	19.61 (15)	24.94 (16)	36.38 (18)	50.38 (20)
Kβ$_2$			19.97 (3)	25.46 (4)	37.26 (6)	51.70 (7)

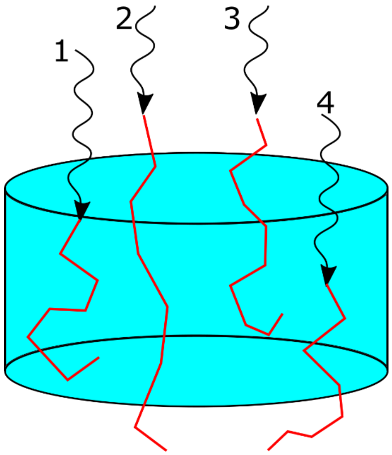

Figure 5.1:Illustration of 4 types of events where photons (black tracks) produce photoelectrons (red tracks) that deposits energy in a cylindrical SV. The events are called: insider (1), crosser (2), stopper (3) and beginner (4).

For the distinct X-ray energies in Table 5-1 to be visible in a single event energy deposition spectrum, a significant fraction of the photons has to create a photoelectron within the SV that becomes entirely absorbed within the SV, an *insider event*. However, the photoelectron can also deposit only parts of its energy within the SV as seen in Figure 5.1. The fraction of insider events increases with increasing SV and decreasing photon energy. The calculated range of photoelectrons in silicon with energy approximately equal to the photon sources used can be seen in Table 5-2. Approximate values were used since the range for exact energies and energies below 10 keV were not available.

Table 5-2: Range of electrons in silicon with energy comparable to the photon energies used. Calculated from ESTAR data (Berger, Coursey, Zucker, & Chang, 2017).

Electron energy (keV)	*Range* (μm)	*Comparable sources* Element	Energy (keV)
10	1.5	Cu	8.0
12.5	2.2	Rb	13.4
17.5	3.9	Mo	17.5
20	4.9	Ag	22.2
30	9.9	Ba	32.2
45	20.0	Tb	44.5
60	32.8	^{241}Am	59.5

Due to the small SVs a very low fraction of X-rays will produce photoelectrons within the SVs which demand high intensities to get a decent counting rate. In order to position the source as close to the SVs as possible without risking any damage to the microdosimeter or its wire bonds, the source was positioned behind the microdosimeter, radiating through it. This led to an attenuation of the beam, especially for the softest X-rays. Through the 300 μm thick silicon bulk, the X-rays from Cu and Rb were attenuated by approximately 90 and 50%, respectively, while the rest was attenuated less than 20% (Hubbell & Seltzer, 2004).

The peaks in the measured spectra from all the photon sources were used for calibration. However, the measured peaks consisted of several spectral lines that were merged into a single peak due to noise, thus it was not straightforward to determine the mean energy of the peaks. This was solved by simulating the experimental setup with photon energies and intensities as in Table 5-1. An RMS noise equal to that measured in the experimental setup was added to the simulated energy deposition, which merged the spectral lines to a single peak, as in the experiment. These peaks were then used for calibration.

The microdosimeter CCE was estimated by first measuring the spectra of the 6 photon sources with an Ortec Ultra PIN diode detector. With the source removed, the signal generator was tuned to inject charge that generated spectra with peaks at the same position as those measured with the source and PIN diode. The same charges were then injected while the microdosimeters were connected, which generated spectra with peaks that represent 100% CCE from the photon sources. The microdosimeter CCE was determined as the ratio of measured photon peaks over the charge injected peaks.

5.1.4 Alpha measurements

The source used for alpha measurements was an ^{241}Am source (Ortec Am-1U) where the equivalent source thickness was < 8 keV. The measurements were conducted in vacuum below 10^{-2} mbar with a detector-source distance of 25 mm, resulting in < 0.03 keV energy attenuation according to ASTAR data (Berger et al., 2017). The source was collimated through a 4 mm diameter hole directly above the microdosimeter.

Measurements were also performed with a nylon6 absorber film attached in front of the collimator. The thickness of the absorber film was measured to 27 µm with a Mitutoyo Series 293 QuantuMike Micrometer. The absorber thickness was chosen such that the alpha particles would stop within the SV, and generate a spectrum containing several peaks corresponding to the thicknesses of the dead layers above the SVs, as illustrated in Figure 5.2.

Calibration was conducted by measuring the ^{241}Am spectra with an Ortec Ultra PIN diode and then tuning the signal generator to inject charge equivalent to the main 5.486 MeV peak from the ^{241}Am spectra. With the microdosimeter connected, the signal generator injected charge equal to 5/10, 4/10, 3/10, 2/10 and 1/10 of the 5.486 MeV peak. Along with a baseline measurement, this gave a 6-point calibration between 0 and 2.743 MeV.

The experimental results from the L_{st} microdosimeter were compared to the simulation model to test the validity of the model, and to estimate the microdosimeters’ CCE. The large standard was used as this was the only microdosimeter design with a detailed model.

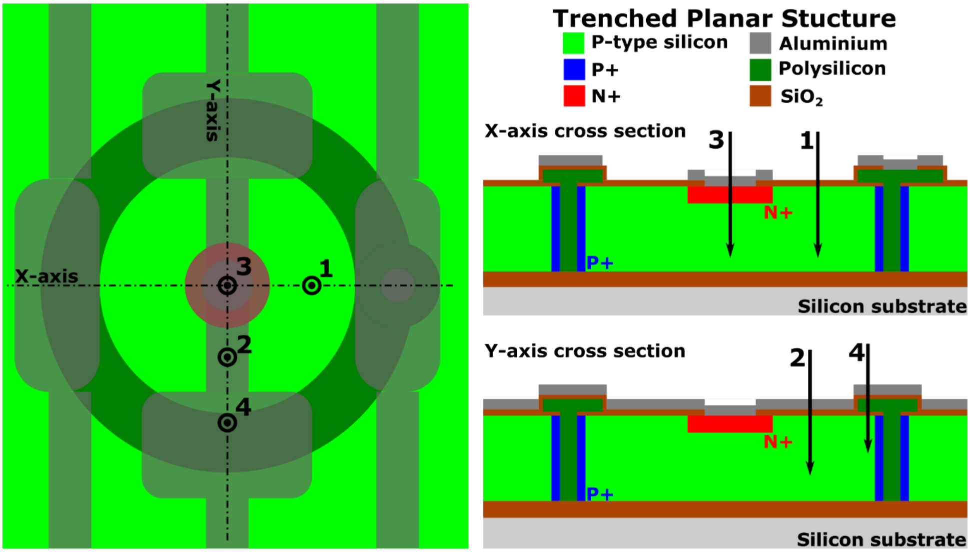

Figure 5.2: Illustration of four alpha particle tracks that deposit different amounts of energy due to the varying dead layer thickness above the SV. The four tracks are shown in both the top view and in the cross-section cuts.

Energy deposition from several of the X-ray sources was also measured with all the microdosimeters when the setup was calibrated for alpha measurements (0-2.743 MeV). This was done to estimate the measurement accuracy of energy depositions from delta electrons when the system was calibrated for high LET particles.

The L_{st} microdosimeter was also used to measure the energy deposition from ^{241}Am alpha particles with 6 bias voltages between 0 and 40 V to see if the bias voltage had any visible effects on the energy deposition and CCE.

5.2 Results

5.2.1 I-V and C-V characteristics

The I-V characteristics for the four detectors from 0 – 100 V can be seen in the semi log plot in Figure 5.3, where the detectors break down and become conductive between 75 and 95 V. Figure 5.4 shows the same I-V data in a linear plot over the first 30 V which is the relevant voltage range when operating the detectors. The detectors show a sharp increase in current with increasing voltage the first 5 V before settling on a constant slope after 5 – 10 V, except for the S_{Poly} microdosimeter which has an almost constant slope from 0.5 V to 30 V. The L_{st} detector shows an almost ideal I-V curve with a roughly constant leakage current between 30 and 40 pA in the range 10 to 50 V.

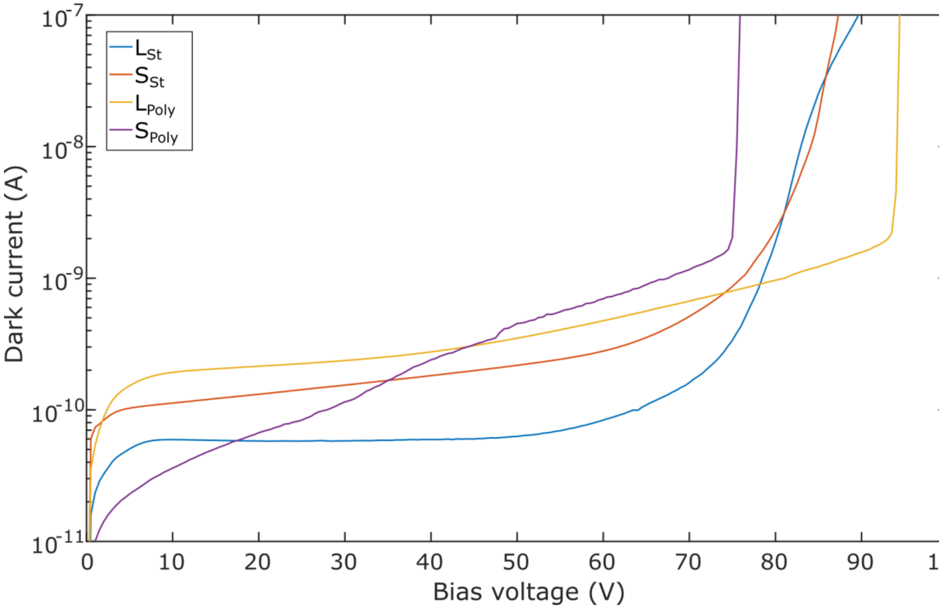

Figure 5.3: I-V curves from the four microdosimeters with logarithmic y-axis that shows the leakage current from 0 V up to the breakdown point where the current increases rapidly with increasing voltage.

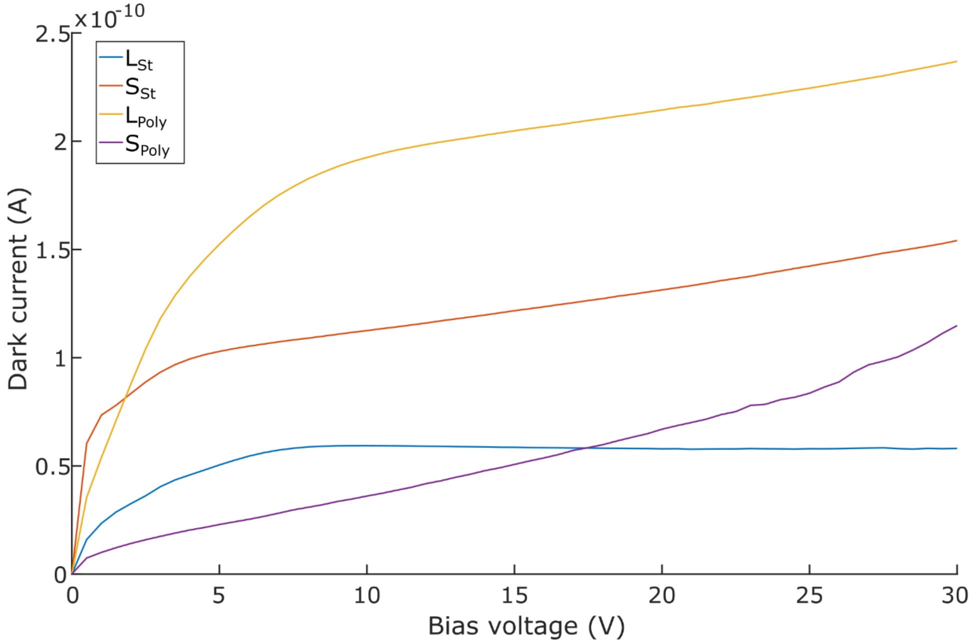

Figure 5.4: I-V curve from the four microdosimeters with linear scale over the voltage range used to operate the devices.

The C-V characteristics for the four microdosimeters is shown in Figure 5.5. The capacitance for all the microdosimeters falls with increasing bias voltage as expected and reaches a minimum once the detector is fully depleted. The depletion capacitance between the devices is relatively large. The largest depletion capacitance is 78 pF for the S_{St} microdosimeter, while the smallest depletion capacitance is 9 pF for the S_{Poly}. All microdosimeter are fully depleted at 5 V except for the L_{Poly} which is fully depleted at 13 V.

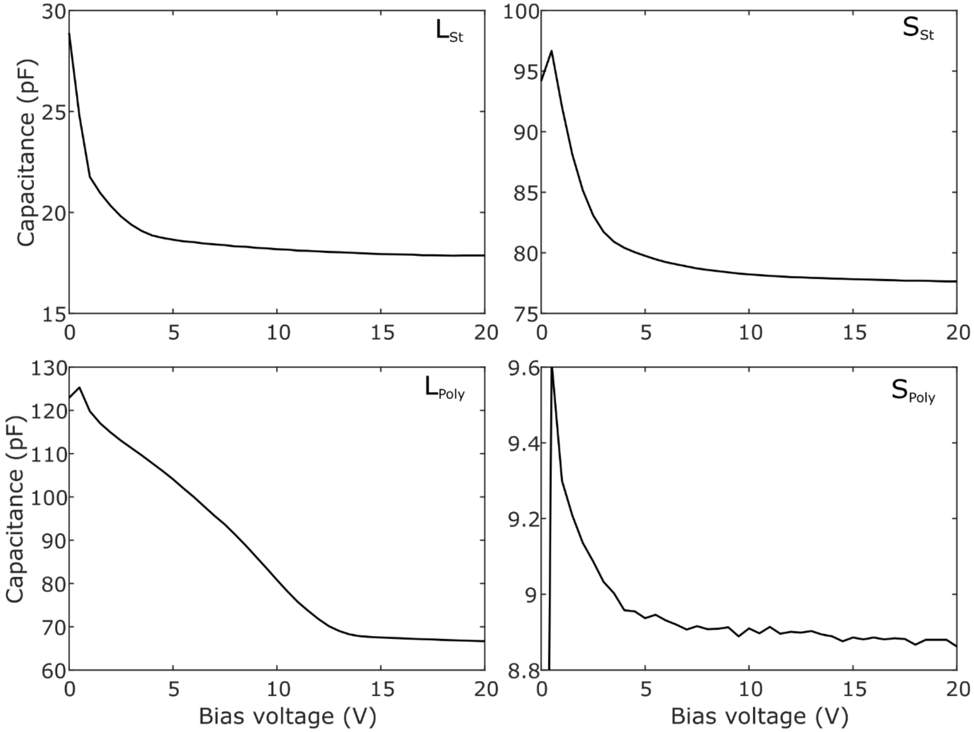

Figure 5.5: C-V plots from all four microdosimeters.

5.2.2 Soft Photons

Figure 5.6 shows the calibrated experimental results from all the photon sources, measured with the L$_{st}$ microdosimeter, where a threshold has been added to the plots to have fewer crossing lines. The top of each peak has been fitted with a Gaussian function and the mean and standard deviation from the Gaussian fit is shown at the top of the figure.

All the distributions contain clear peaks corresponding to full absorption of the photoelectrons (insider events). Except for the Cu and Tb source, the Gaussian fit gives a standard deviation, which is approximately equal to the measured RMS noise of 0.9 keV. It was expected that the spectrum from the Cu source would have a wider peak than the others as the difference between the Kα and Kβ lines are approximately equal to the RMS noise. In the Tb source, the two Kα lines are separated by 0.74 keV, which is close to the RMS noise, and this broadens the measured peak slightly.

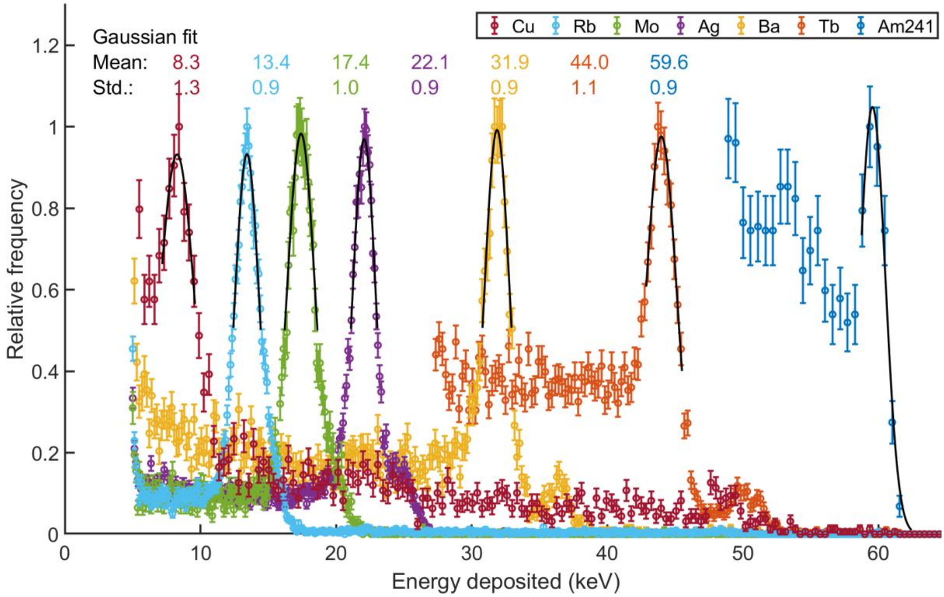

Figure 5.6: Measured energy deposition from all six photon sources with a the large standard microdosimeter. The distributions have been normalized with respect to the peak amplitude. Thresholds have been added to get fewer crossing lines to make the peaks more visible. A Gaussian fit has been added to the top of each peak and is shown with black lines. The mean and standard deviation for each of the Gaussian fits can be seen at the top.

The fitted means for all the peaks are within 0.5% of the intensity-weighted average of the two Kα lines in Table 5-1, except for the Cu source. For the Cu source the mean is within 3.2% of the intensity-weighted average of the two Kα lines, and within 1.6% of all three K-lines. The detection threshold used was equivalent to 5.1 keV.

Comparison of the experimental and simulated energy deposition spectra for the L_{st} microdosimeter for all sources is shown in Figure 5.7, 5.8 and 5.9. The large rise in events above the detection threshold (5.1 keV) in the experiments are due to noise and a not “real” events. Apart from the Cu measurements, the experimental and simulated spectra match well. The Cu measurements had approximately 1/10 of the detection rate compared to the other sources. This is due to the inherent lower intensity of the Cu source and because about 90% photons were absorbed in the silicon bulk before reaching the SVs.

The low counting rate in the Cu measurements increased the fraction of noise generated events (low energy) and events from the other shielded X-ray sources with higher energy.

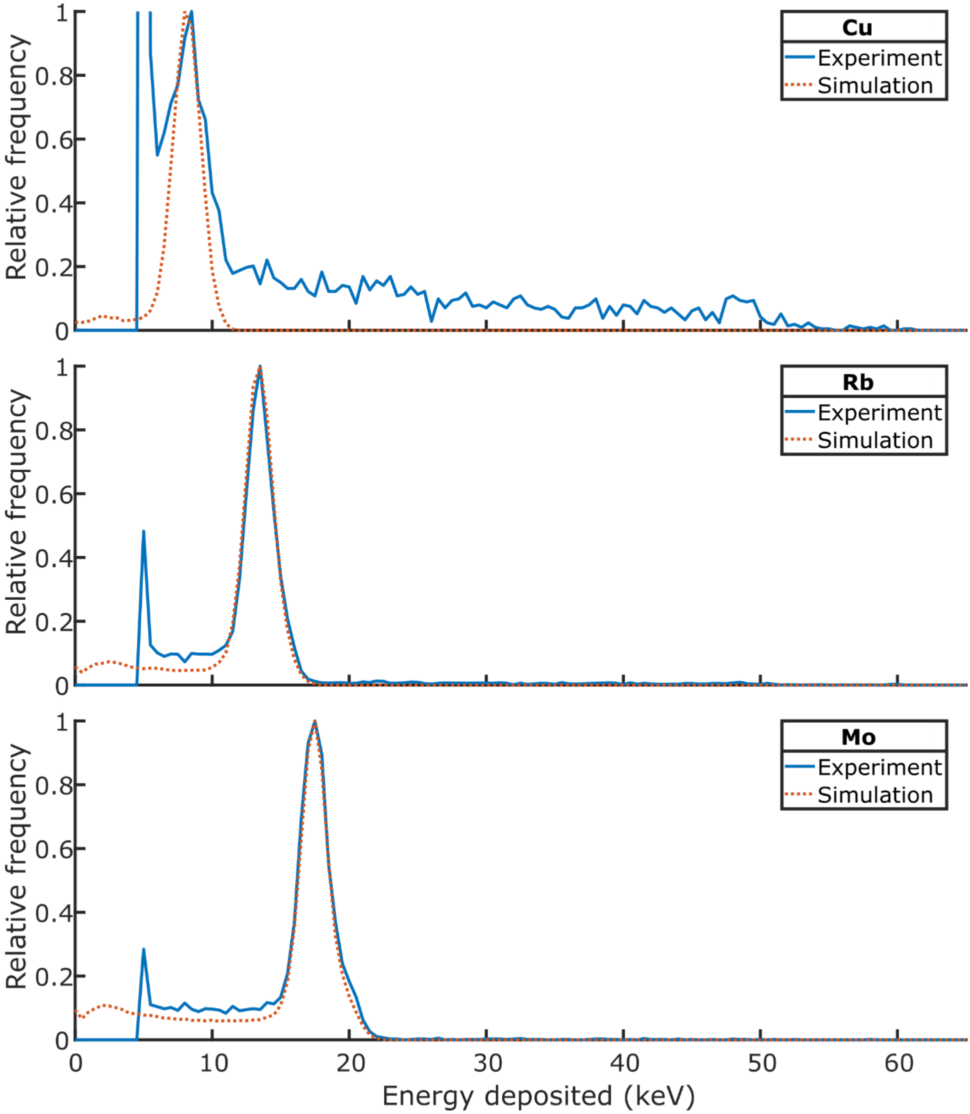

Figure 5.7: Measured and simulated energy deposition in the L_{st} microdosimeters from the X-ray sources: Cu, Rb and Mo. The distributions have been normalized with respect to the peak amplitude. An RMS noise of 0.9 keV has been added to the simulation results, which is equal to the RMS electronics noise in the experiment.

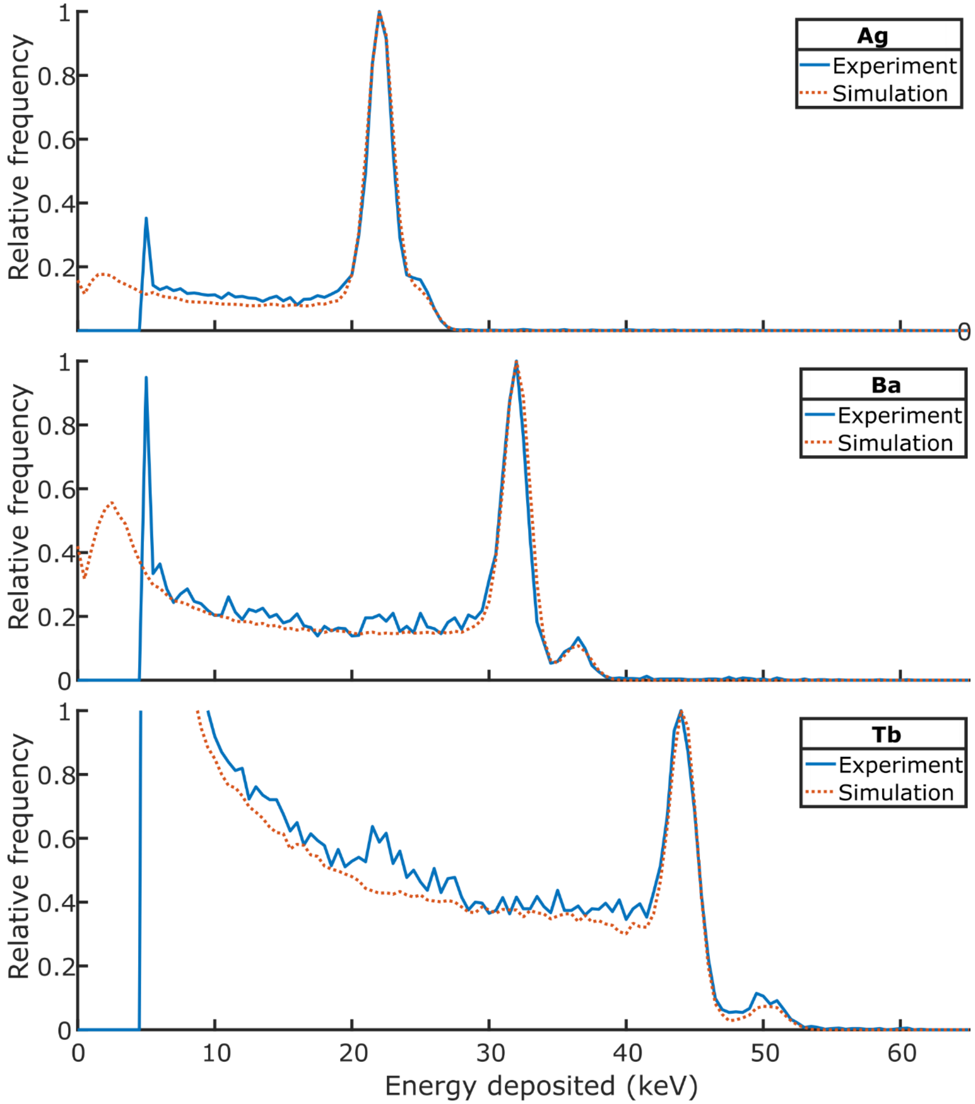

Figure 5.8 Measured and simulated energy deposition in the L_{st} microdosimeters from the X-ray sources: Ag, Ba and Tb. The distributions have been normalized with respect to the peak amplitude. An RMS noise of 0.9 keV has been added to the simulation results, which is equal to the RMS electronics noise in the experiment.

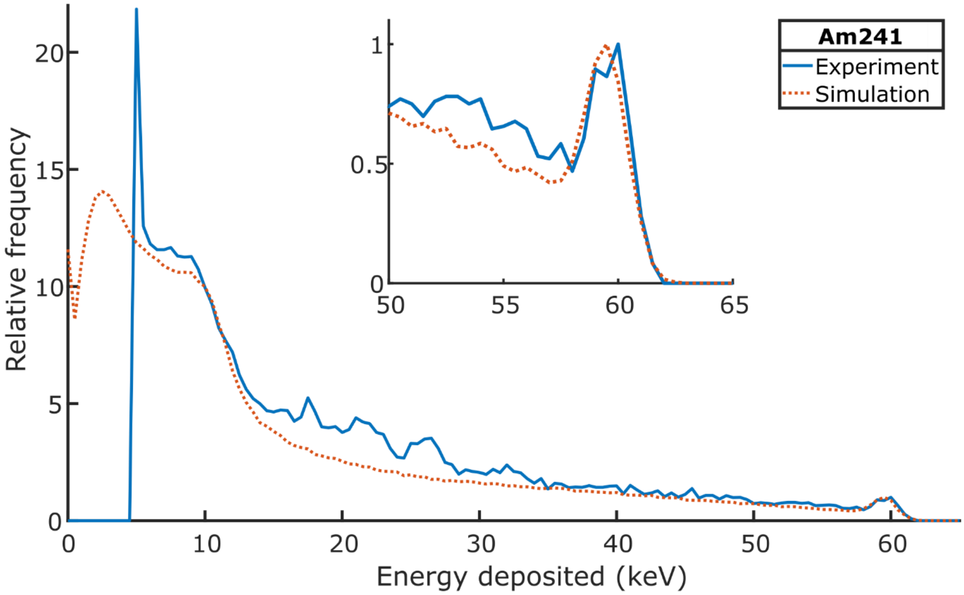

Figure 5.9: Measured and simulated energy deposition in the L_{st} microdosimeters from the ^{241}Am gamma source. The distributions have been normalized with respect to the peak amplitude. An RMS noise of 0.9 keV has been added to the simulation results, which is equal to the RMS electronics noise in the experiment.

All the photon sources with energy above that of Cu resulted in spectra with a long tail towards lower energies in both the experiments and the simulations. This tail is due to crosser, beginner and stopper events depositing less energy than the insider events in the peak. For the lower energy sources, Rb, Mo and Ag, the low energy tail is approximately constant in amplitude. For the higher energy photon sources, Ba, Tb and ^{241}Am, the tail amplitude is largest for low energy events and falls with increasing energy in both the experiment and simulation. For the ^{241}Am gamma measurement the fraction of events making up the peak (insider events) were 1.1% of all recorded events. For the x-ray sources, Ag, Ba and Tb, the lower intensity Kβ lines are visible in both the experiment and simulation.

The experimental results generally had slightly more events in the low energy tail than the simulation. The simulation results showed that the amplitude of the low energy tail was elevated when the added noise and the histogram bin size were increased.

All sources were not measured with all the microdosimeters as measurements took more than a day for a single source and microdosimeter combination. The S_{Poly} microdosimeter had a considerably lower count rate than the other devices and were therefore only used to measure the x-ray sources: Mo, Ba and Tb. Due to the very low fraction of insider events with the ^{241}Am gamma source it was only measured with the L_{st} (Figure 5.9).

The experimental results for all four microdosimeters are shown and compared in Figure 5.10 and 5.11. All devices successfully generated spectra that contain clear peaks from photoelectron insider events. The peaks produced by the L_{st} and S_{Poly} are narrower than the other two, which is due to differences in electronics noise. The RMS noise was equivalent to 0.9 keV for the L_{st} and S_{Poly}, while it was 1.3 keV for the S_{St} and L_{Poly}. This is consistent with the I-V and C-V measurements that showed the lowest dark current and capacitance for the L_{st} and S_{Poly}. These two microdosimeters also had a lower count rate than the others, which suggest that many of the diodes/SVs were unconnected.

The amplitude of the low energy tail increases with noise and are thus largest for the S_{St} and L_{Poly}. For the higher energy sources, Ba and Tb, the tail is also increased for the microdosimeters with small SVs as the combination of small SV and large photo electron range produces a smaller fraction of insider events.

The measured CCE for the different photon sources and microdosimeters is shown in Table 5-3, where the mean from all sources and microdosimeters is 100.6% with a standard deviation of 0.7%.

Table 5-3: CCE estimates for all the microdosimeters and sources.

	L_{st}	S_{St}	L_{Poly}	S_{Poly}
^{241}Am γ	101.4%	-	-	-
Tb	101.2%	100.2%	100.4%	101.0%
Ba	100.2%	99.5%	99.4%	100.3%
Ag	101.2%	100.9%	101.1%	-
Mo	101.0%	100.7%	100.9%	101.5%
Rb	99.8%	99.5%	-	-

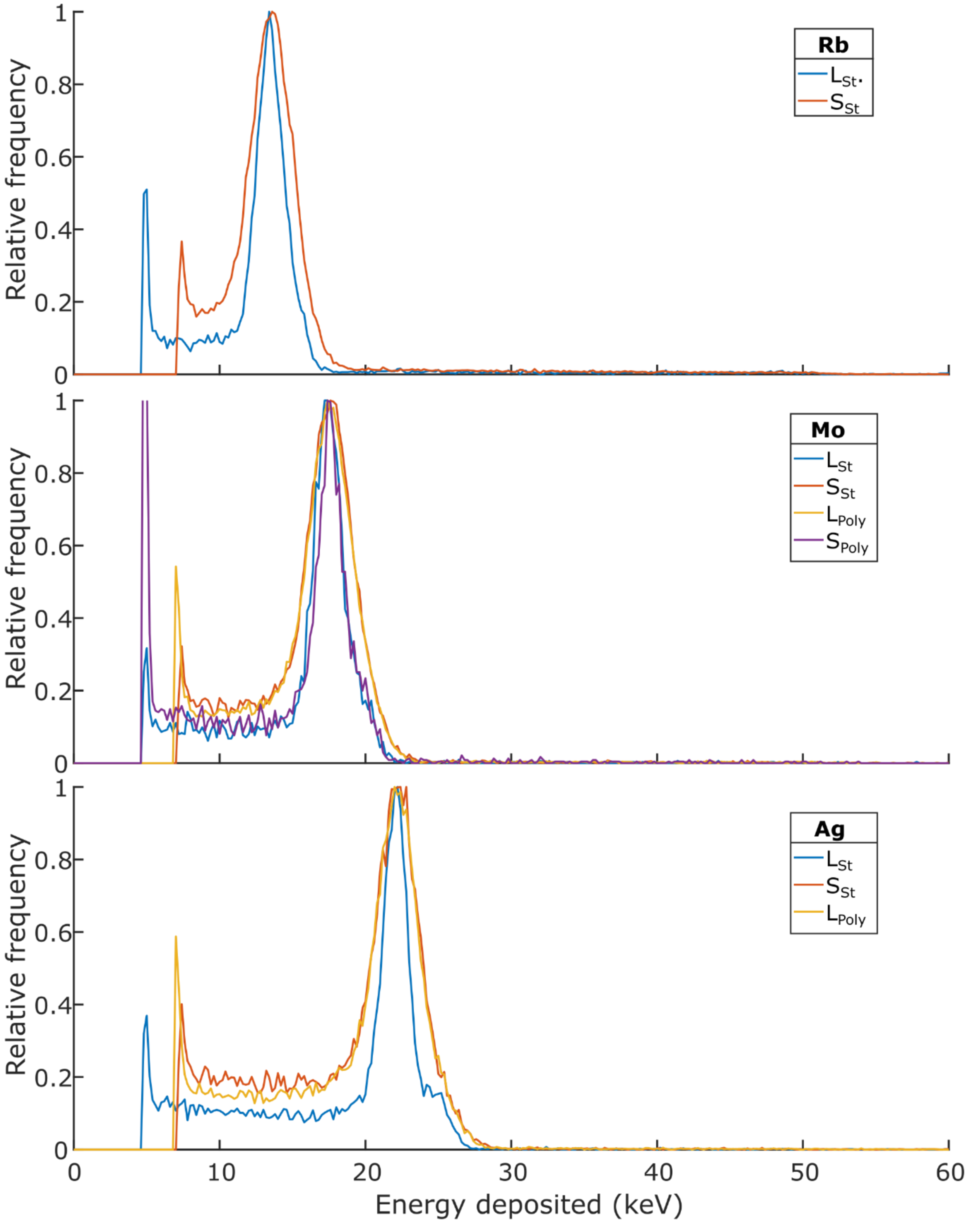

Figure 5.10: Measured energy deposition in the four microdosimeters from the X-ray sources: Rb, Mo and Ag. The distributions have been normalized with respect to the peak amplitude.

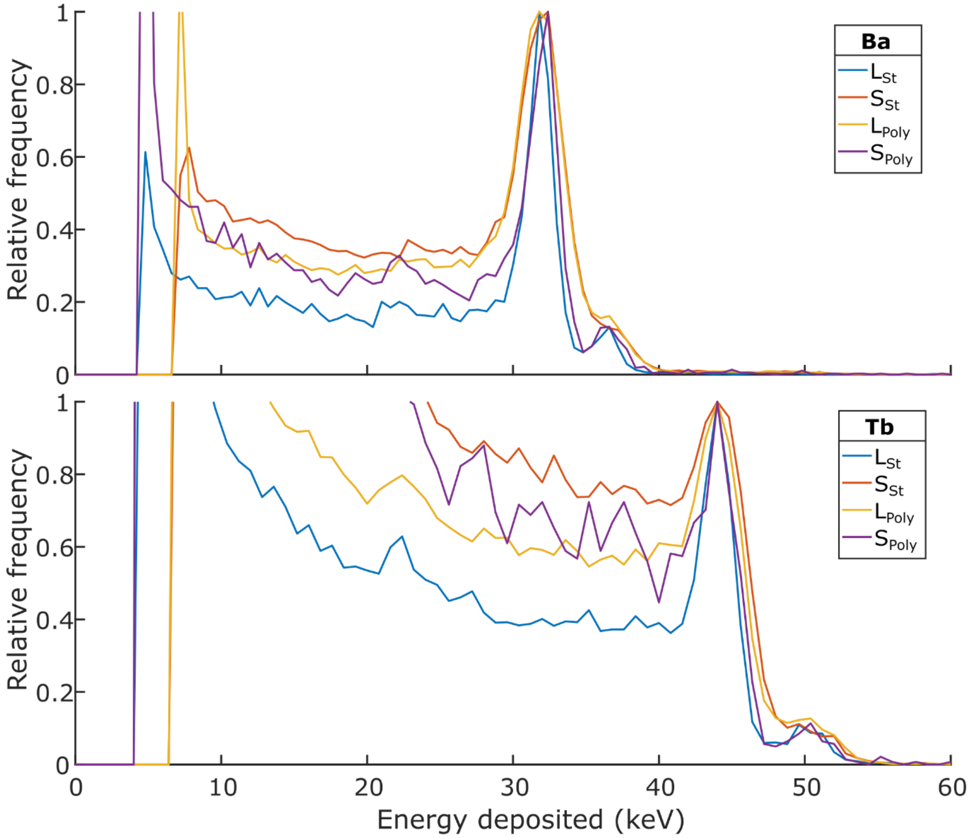

Figure 5.11: Measured energy deposition in the four microdosimeters from the X-ray sources: Ba and Tb. The distributions have been normalized with respect to the peak amplitude.

5.2.3 Alpha measurements

The experimental and simulation results from the ^{241}Am alpha source without absorbers are shown in Figure 5.12. The microdosimeter was simulated with both 9.1 and 9.5 μm high SVs, where 9.1 μm was measured for the slightly different 3D trenched device with an SEM (L. T. Tran, Chartier, Prokopovich, et al., 2018) and 9.5 μm gave the best fit with the experimental data. The mean energy of the peak in the experimental result is 4.6% higher than the peak in the simulation with the 9.1 μm high SVs.

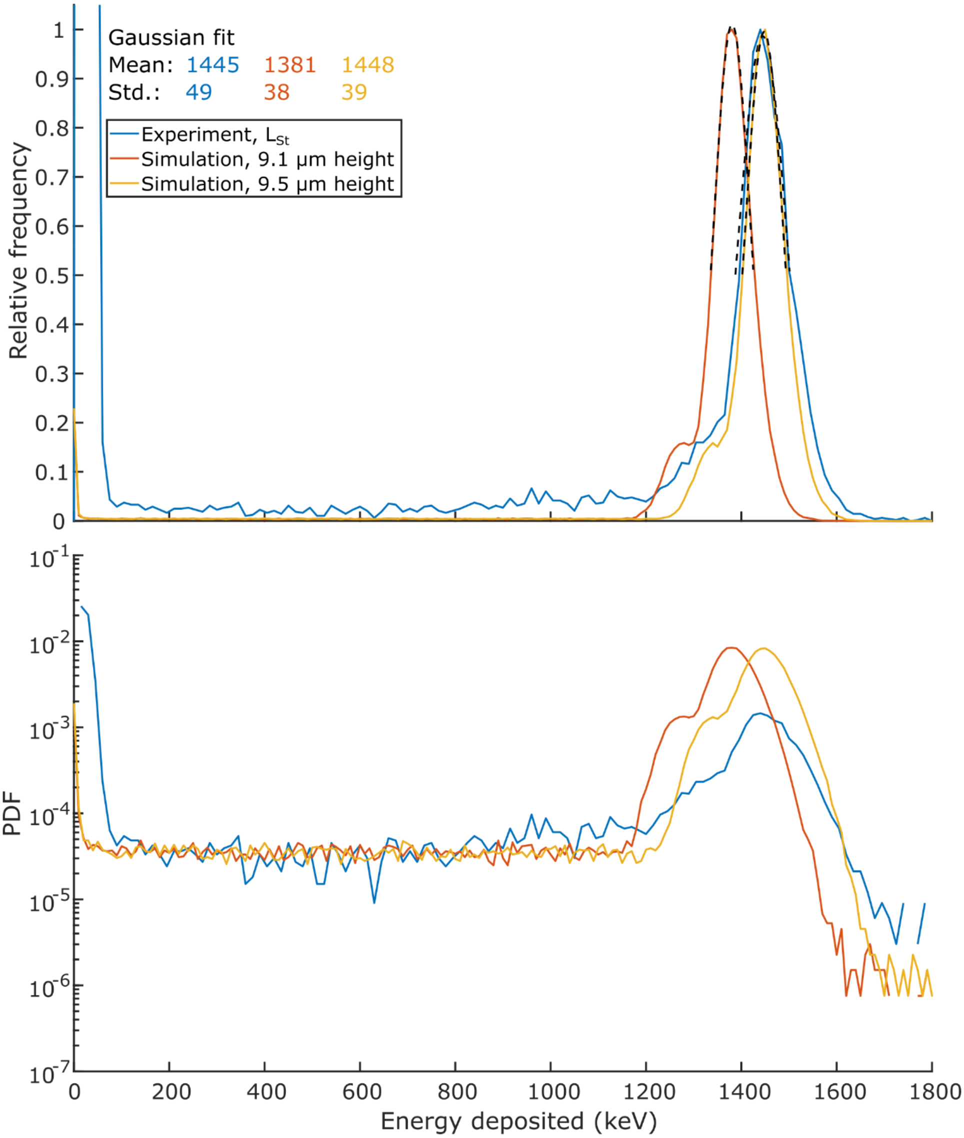

Figure 5.12: Measured and simulated energy deposition in the L_{st} microdosimeter from ^{241}Am alpha particles with no absorbers shown with linear (top) and logarithmic (bottom) y-axes. The linear plots have been normalized with respect to the peak's amplitude, while probability density functions are applied in the semi-log plot.

The top half of the peak has been fitted with a Gaussian function in the linear plot (black line). The spectra are shown without error bars to increase visibility, and the relative bin error in the peak is 4.5%. The microdosimeter was simulated with 9.1 and 9.5 μm high cylindrical SVs, where the 9.1 μm was measured with a SEM (L. T. Tran, Chartier, Prokopovich, et al., 2018) and 9.5 μm gave the best fit to experimental results.

In Figure 5.12, the peak in the experiment is slightly wider than in the simulations, and while there are virtually no events below 1200 keV in the simulations, the experimental results show an approximately constant event rate between 100 keV and 1200 keV. Below 100 keV the experimental results show vastly more events than the simulations, which is not due to electronics noise as these do not occur without the source. There is also a small shoulder on the rising edge of the peaks, at ~1350 keV in the experiment, which is from tracks passing through the highly doped N^+ central electrode (track 3 in Figure 5.2), which is less sensitive to radiation due to the high dopant concentration. In the MC model this was modelled as a 1 µm thick insensitive cylinder, as seen in Figure 4.1, which fits the experimental data well.

The experimental and simulation results from the ^{241}Am alpha source with the ~27 µm thick Nylon6 is shown in Figure 5.13. The setup was simulated with 27.0 and 24.7 µm thick absorbers, where 27 µm was the thickness measured with the micrometer, while a 24.7 µm thick absorber resulted in the best agreement with the experimental results.

The plots show two distinct peaks, where the high energy peaks of the simulation at 2250 and 1811 keV are from events passing the least amount of dead layer above the SVs (track 1 in Figure 5.2). The lower energy peaks at 1866 and 1384 keV are from particle tracks passing through the 1.4 µm thick aluminium layer above the SVs (track 2 in Figure 5.2). The overall shape is very similar, but the experimental results have more events with energy between the two peaks than the simulations. This is likely because the aluminium layer in the simulations have perfect 90° edges while they are rounded in the real detector. The experimental results also have an approximately constant event rate between 100 keV and 1600 keV, and a sharp increase in events below ~100 keV, as seen in Figure 5.12.

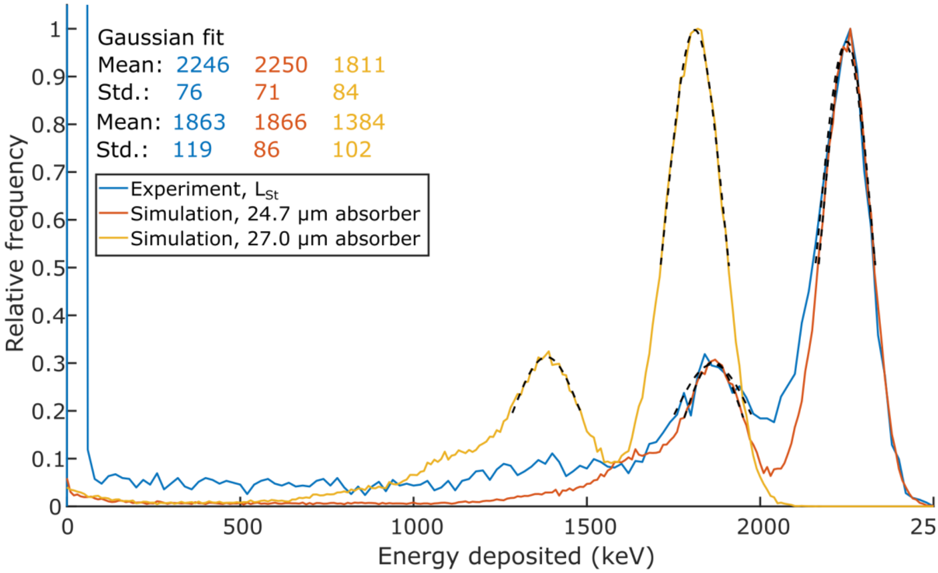

Figure 5.13: Measured and simulated energy deposition in the large standard microdosimeter from ^{241}Am alpha particles with Nylon6 absorbers where the alpha particles stop within the SV. The spectra have been normalized with respect to the peak's amplitude. The top of the two peaks in each spectrum has been fitted with a Gaussian function. The relative bin error in the high and low energy peak is 4.5% and 7.9%, respectively. The simulation was performed with 24.7 and 27 µm thick absorber.

The experimental results for all four microdosimeters without the absorber are shown in Figure 5.14 and with the absorber in Figure 5.15. The microdosimeters had an RMS noise equivalent of 1.9 keV, and the detection threshold was set to 12 keV. The S_{Poly} microdosimeter had a very low count rate which resulted in only 359 and 773 events with and without the absorber, respectively, after measuring for almost four days.

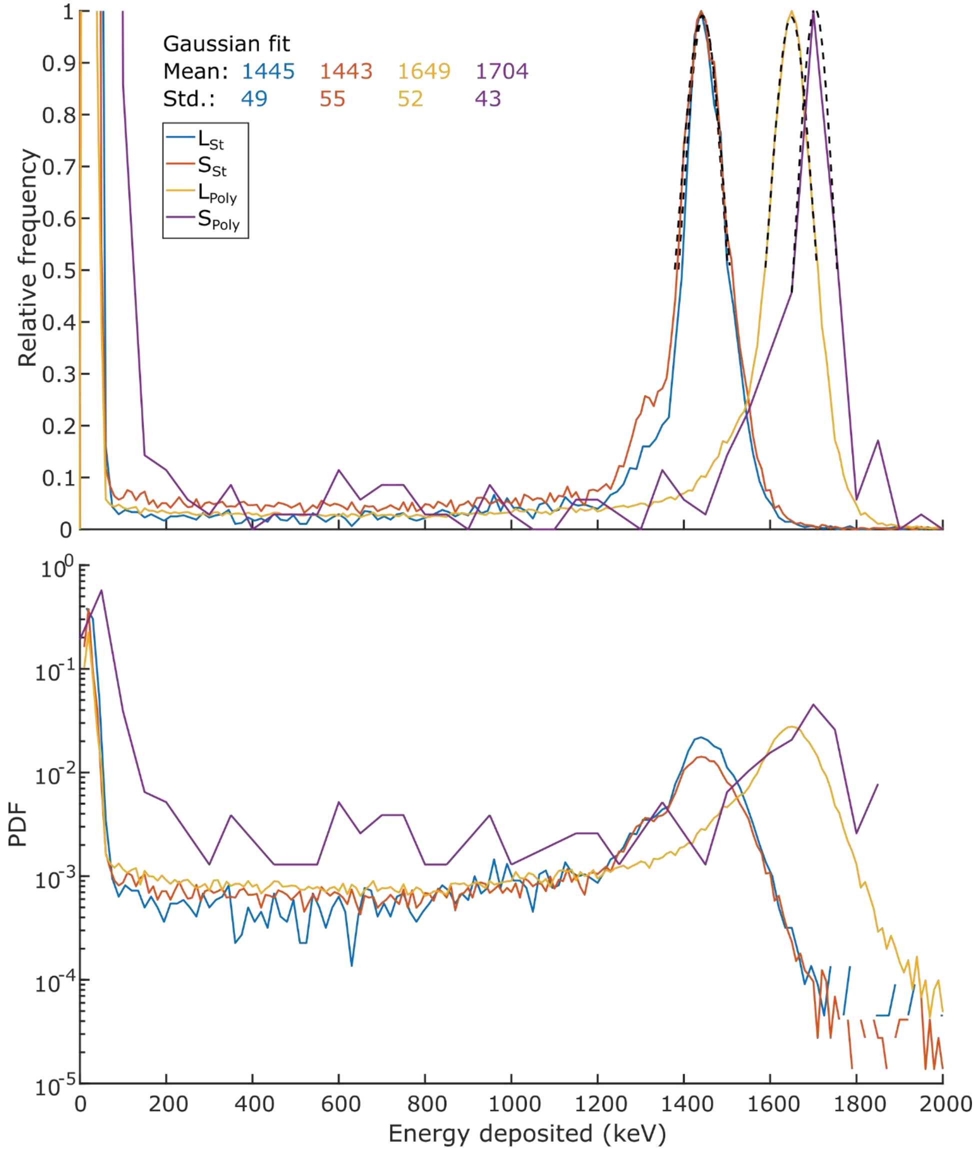

Figure 5.14: Measured energy deposition from ^{241}Am alpha particles from all four microdosimeters without absorbers, shown with linear (top) and logarithmic (bottom) y-axes. The linear plots have been normalized with respect to the peak's amplitude, while probability density functions are applied in the semi-logarithmic plots. The max bin error in the peak for P_{Poly} was 17%, while it was 4.5% or below for the others. The top of the peaks has been fitted with a Gaussian function in the linear plot.

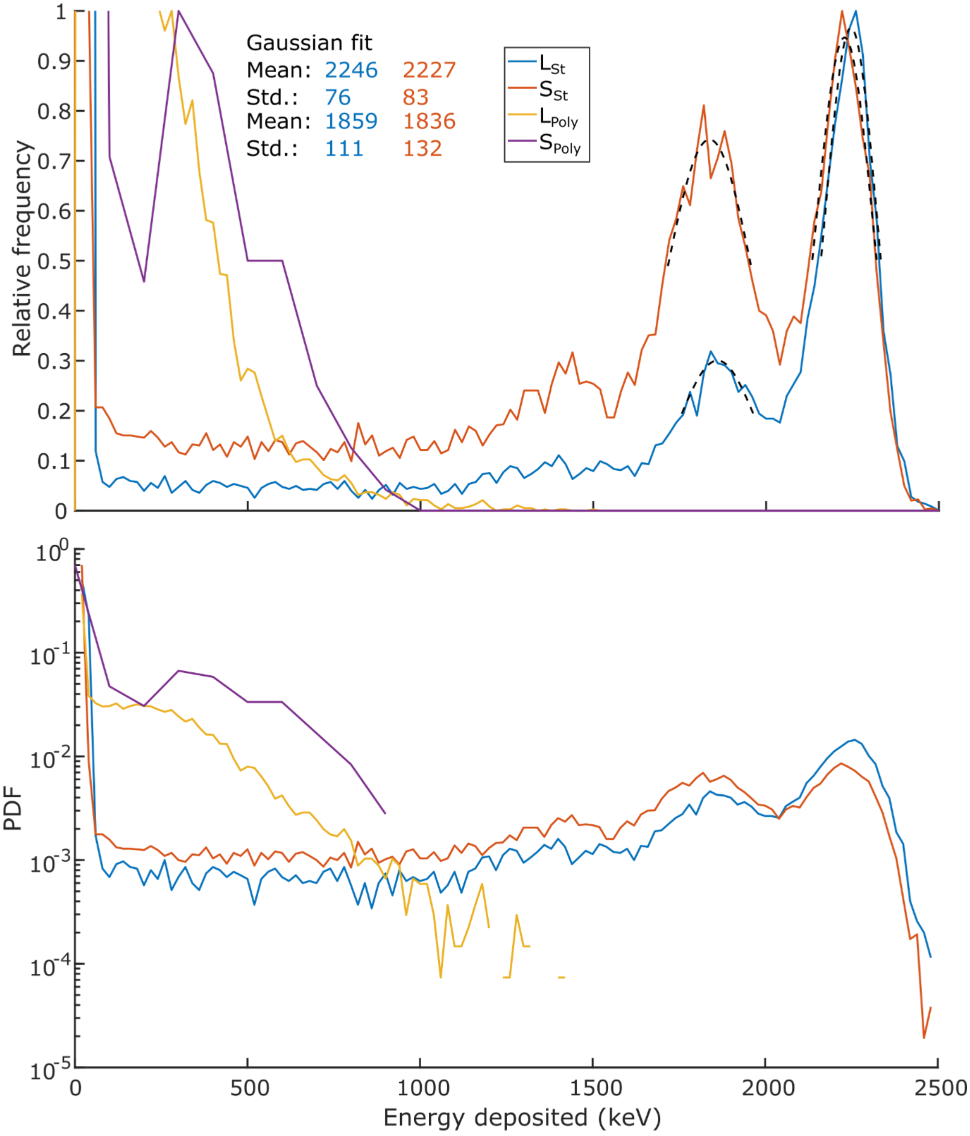

Figure 5.15: Measured energy deposition from ^{241}Am alpha particles from all four microdosimeters with Nylon6 absorbers, shown with linear (top) and logarithmic (bottom) y-axes. The linear plots have been normalized with respect to the peak's amplitude, while probability density functions are applied in the semi-logarithmic plots. The relative bin error for both the high energy peaks are 4.7%, while for the lower energy peaks it is 7.9% (L_{St}) and 5.3% (L_{St}). The top of the peaks has been fitted with a Gaussian function in the linear plot.

The peaks' mean value from the L_{st} and S_{St} are equal without the absorber and are within 0.9% with the absorber. The L_{Poly} and S_{Poly} microdosimeter shows peaks with much higher energy without the absorber, and with the absorber the alpha particles barely penetrate the SVs. The likely reason for this is that a thin layer of a few microns of polyimide also covers the SVs. The thickness of the polyimide layer above the SVs must be homogeneous since the width of the peaks without absorbers are approximately the same as for the standard microdosimeters. The S_{St} microdosimeter also has a more distinct shoulder at ~1350 keV than the L_{st} in Figure 5.14. This is due to the central N^+ electrode having a larger cross-sectional area relative to the entire SV in the small devices.

With the absorber, the low energy peak of the S_{St} microdosimeter (1836 keV) has a much higher amplitude than the L_{st} (1859 keV), as the small devices has a much larger fraction of its surface covered by aluminium. The S_{St} microdosimeter also has a third peak at ~1450 keV with the absorber, which is likely due to the polysilicon extending slightly over the SVs at the trench (track 4 in Figure 5.2). This third peak is not visible for the L_{st} microdosimeter.

An overview of the measurements with the X-ray sources when the system was calibrated for alpha particles is shown in Table 5-4 along with the simulation results. The peaks mean energy is given in keV and relative to the simulation (%) for all measurements. On average, the energy deposition in the experiments are 100.5% of the simulation with a standard deviation of 2.5%.

Table 5-4: Comparison of the peaks mean energy deposition in the experiments and simulation for the x-ray sources when the setup was calibrated for alpha particles. The mean values are given in keV and relative to the simulation results. The S_{St} and L_{Poly} microdosimeter were not used to measure the Rb source as the peak was below the detection threshold. Due to a very low count rate, the S_{Poly} device were only used to measure the Ag and Ba X-ray sources.

X-ray	Simulated	L_{St}		S_{St}		L_{Poly}		S_{Poly}	
sources	(keV)	(keV)	%	(keV)	%	(keV)	%	(keV)	%
Tb	44.1	43.8	99.4	42.8	97.0	43.1	97.8	-	-
Ba	32.0	32.0	100.1	31.6	98.7	31.7	98.9	31.9	99.8
Ag	22.1	22.6	102.3	22.3	101.0	22.5	101.8	22.6	102.1
Mo	17.4	18.3	105.1	18.0	103.7	18.1	103.8	-	-
Rb	13.4	12.9	96.5	-	-	-	-	-	-

The L_{st} microdosimeter was used to measure the alpha source without an absorber with 6 different bias voltages between 0 and 40 V. The results are shown in Figure 5.16 and show that neither the mean nor the width of the high energy peak change significantly by altering the bias voltage, indicating full CCE for all bias voltages. However, the energy deposition below 50 keV show peaks that depend on bias voltage. The position of the low energy peak is ~20 keV at 0 V and increases to ~36 keV at 40 V. The relative peak height of the low energy peaks is ~10 to ~25 times larger than the main high energy peak at ~1450 keV. This shows that the low sensitive area has a much larger cross-sectional area than the main SV.

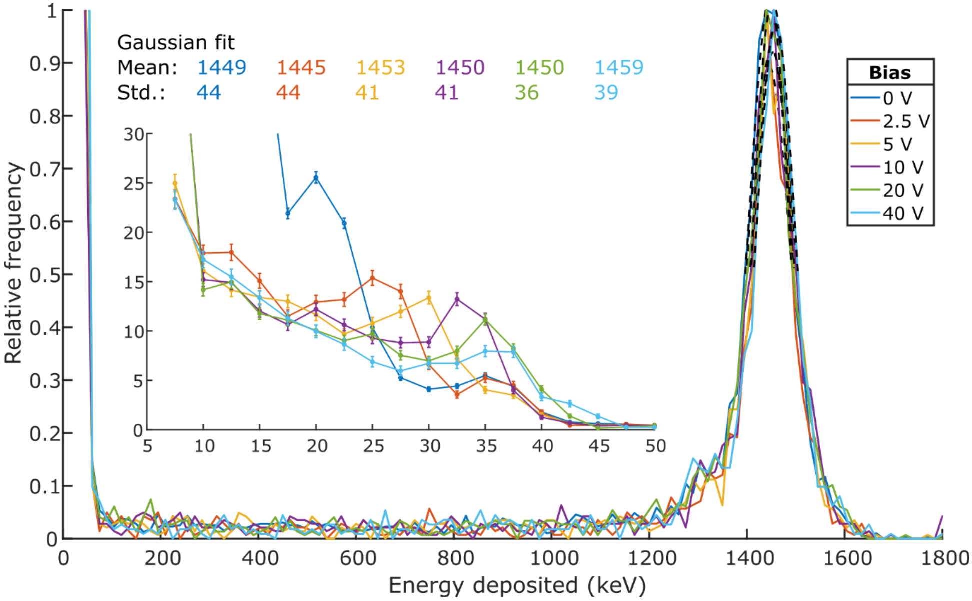

Figure 5.16: Energy deposition spectra from an ^{241}Am alpha sources with bias voltages ranging from 0 – 40 V. The spectra are normalized with respect to the amplitude of the high energy peak, and a Gaussian function has been fitted to the peak. The relative bin error in the peaks are from 9.5% and below. Events between 5 and 50 keV are magnified and showed in the middle of the figure with error bars on the bins to show that the peaks are significant.

5.3 Discussion

All four designs of the microdosimeter perform similarly and generally agree well with the simulations of the L_{st} device. The S_{Poly} microdosimeter had a very low dark current, capacitance and count rate, which is likely due to several unconnected SVs. It is not believed that this is a problem with the S_{Poly} design in general, rather a problem for this specific device. This is due to problems with the planarization of the polysilicon which led to breaches in the aluminium layer. This was also seen in the microbeam experiment of another trenched planar microdosimeter (L. T. Tran, Chartier, Prokopovich, et al., 2018).

The overall good match between the experimental and simulation results of the L_{st} microdosimeter for both photons and alpha particles suggests that the MC model is accurate and that the GATE software can produce reliable results for micrometric SVs for low energy photons, electrons and alpha particles.

For soft photons, the fraction of insider events decreases rapidly beyond approximately 40 keV as the Tb (44 keV Kα) source still has a significant fraction of insider events, while the ^{241}Am γ source (59.5 keV) had a very small fraction of insider events. The lineal and specific energy of an insider event from a monoenergetic photon source depend only on the size of the SV. Beginner and ending events also depend heavily on the SV size, and less on energy deposition. However, the lineal energy and specific energy are less dependent on the SV size when most events are crossers. Thus, the microdosimetric spectra from soft photons in SVs with 1 μm and 10 μm mean chord lengths will differ considerably.

The large amount of low energy events from the alpha source was also seen in a microbeam test of the L_{st} microdosimeter (L. T. Tran, Chartier, Prokopovich, et al., 2018), which showed that they come from a circular belt outside the diode trenches. The likely reason for this is that the aluminium on top of the SiO_2 produces a capacitor, and when a large amount of charge moves underneath it, a pulse is induced in the aluminium conductor. Figure 5.16 shows that this effect depends slightly on bias voltage. The microdosimeters have a highly doped P^+ layer right underneath SiO_2 that stops this effect, called p-stop. The p-stop covers the entire surface of the microdosimeters but was not deposited within the SVs and at the surface right outside them. Thus, large energy depositions on the outside of the diode trenches produce a small signal.

Results from the soft photon experiments show 100% CCE for all four microdosimeters (Table 5-3). The experimental and simulation comparison with the alpha source suggests that the SVs of the L_{st} and S_{St} are approximately 9.5 μm high (Figure 5.12 and Figure 5.14). The SV heights of the L_{Poly} and S_{Poly} devices were difficult to estimate due to the unknown thickness of the polyimide layer on top.

The detector system showed great linearity as the X-ray measurements gave accurate results when the system was calibrated for high LET alpha particles as well. This shows that delta electrons can be accurately measured when the system is calibrated over a wide LET range. However, the low energy deposition from delta electrons might drown in the large number of low energy events from the low sensitive region outside the diodes.

5.4 Summary

Four designs of the trenched planar microdosimeter were characterized electrically and used to measure the energy deposition from soft photons and alpha particles. The experimental results were compared to GATE MC simulations.

An overall good match between simulations and experiments were observed for both photon and alpha irradiations. The soft photons can be used as a low energy calibration and the photon experiment also showed that all the microdosimeters has 100% CCE, also without applied bias voltage.

Although the main peak in the energy deposition spectra from alpha particles matched very well with simulations, the experiment showed a very large number of low energy events below 100 keV not visible in the simulations. The experiments also showed a low constant event rate with energy between 100 keV and the main peak that were not visible in the simulations. These events are assumed to come from areas of the microdosimeters with less than 100% CCE, and they will lead to a slight distortion in the measured microdosimetric spectra.

There were large differences in event rate between the devices which is assumed to be due to a large fraction of unconnected SVs on some of the devices due to breaks in the aluminium layer.

6. Ion beam induced charge collection for 3D microdosimeter

The ion beam induced charge collection (IBICC) technique is an effective way of determining the position sensitivity of the microdosimeter. The IBICC technique uses a monoenergetic ion microbeam with diameter of 1 μm or less to scan the surface area of the microdosimeters. By recoding the single event pulse height in conjunction with the beam position it is possible to produce a sensitivity map of the microdosimeters.

The IBICC technique has previously been utilized on the trenched planar and trenched 3D structure with a 5.5 MeV ^{4}He beam (L. T. Tran, Chartier, Prokopovich, et al., 2018). In the work presented here, a 24 MeV ^{12}C beam was used to scan a trenched 3D structure microdosimeter. The high LET 24 MeV ^{12}C gives a very high SNR which makes it possible to detect signals from regions on the microdosimeter with very low sensitivity. The high LET beam also deposits a large dose to the scanned area which produces radiation damage effects, which can be studied from the generated sensitivity maps. The aim of the study was multiple. Sensitivity maps of the microdosimeter with increasing radiation damage were generated to characterize the effects of the damage. A detailed map of a few SVs created taken to investigate the sensitivity near the trenches.

In a previous IBICC experiment it was seen that the trenched 3D structure microdosimeters were sensitive outside the opening in the trenches, as seen in Figure 3.9 (L. T. Tran, Chartier, Prokopovich, et al., 2018). The opening in the trenches allowed charge generated outside the SV to enter the SV and be collected leading to a sensitivity gradient at the trench opening. The microdosimeter collects the liberated charge at the N^{+} central column where a positive bias voltage is normally applied. One of the aims of the experiment was to investigate if the electrons liberated outside of the diode would be repelled if a negative bias was applied to the P^{+} trench instead of applying a positive bias at the N^{+} central column, making the region outside of the diodes less sensitive. However, when conducting the experiment, the leakage current kept increasing when the diode was biased through the N^+ column, while the leakage current was stable when the P^+ trench was biased. Only measurements with bias at the P^+ trench were conducted since there was no time to investigate and fix the problem during the one-day beam time. Thus, it is not possible to directly compare the two biasing methods and conclude if the alternative way of biasing decreases the sensitivity outside the diodes. However, in another study the same type of microdosimeter was investigated in a 5.5 MeV ^{4}He microbeam before and after it was radiation damaged (James et al., 2018), and those results are compared with the results presented here.

6.1 Setup & Method

The microbeam experiment was conducted at the Centre for Accelerator Science (CAS) facility at ANSTO where a 24 MeV ^{12}C beam was accelerated by a 4 MV Pelletron tandem accelerator (Zeljko Pastuovic et al., 2016). The standard deviation for the accelerator potential was less than 0.8 kV when operated at 4 MV giving less than 0.02% uncertainty in ion energy. The beam was focused to a spot size of 1 µm and was used to raster scan the surface of the microdosimeter with a Confocal Heavy Ion Micro-Probe (Z. Pastuovic et al., 2017).

An Amptek A250 CSP and CANBERRA Model 2024 shaping amplifier with 1 µs shaping time was used for amplification. The beam scanning and data acquisition was controlled by the OMDAQ software from Oxford Microbeams Ltd. The position of the beam and pulse height (energy deposition) was written to file for every recorded event. An Ortec 480 Pulser was used for signal testing and calibration.

The beam rate was approximately 1500 ions/s, and the absorbed dose (E/m) to the microdosimeter device layer was calculated for each scan. The total deposited energy, E, was calculated from the beam rate multiplied by the irradiation time and the mean energy deposition from 24 MeV ^{12}C ions (8384 keV). The mass was calculated as the product of the scanned area, the silicon device layer thickness (9.1 µm), and the silicon density.

6.2 Results

The energy deposition maps and spectra from the raster scans are shown chronologically in this section. This is done because the dose rate to the device layer was high, and radiation damage effects become more pronounced for each scan.

When a change in bias voltage is discussed in the text, the absolute change is used, such that a change from -5 to -10 V is an *increase* in bias voltage, as this *increases* the E-field in the diodes.

The microdosimeter was calibrated by using a Hamamatsu S3590-09 PIN diode in the 24 MeV ^{12}C beam as described in section 5.1.4. However, the calibrated energy depositions in the experiment was approximately 10500 keV, while the mean energy deposition in 9.1 µm of silicon with 0.85 µm of SiO_2 on top was 8384 keV from 24 MeV ^{12}C, according to simulations. It is assumed that the calibration was inaccurate due to less than 100% CCE in the Hamamatsu S3590-09 PIN diode for 24 MeV ^{12}C ions. Thus, the results are not calibrated, and the measurements are given in the unit of ADC lvl which are proportional to the charge collected for each event.

6.2.1 Large area scan

Maps of the first four raster scans are shown in Figure 6.1, where the X- and Y-axes are given in µm, and the colour coding of each pixel represents the average energy deposited at that point. The four scans were conducted over the same area of the microdosimeter with different bias voltages applied and a 70 ADC lvl detection threshold. As these scans were performed over a relatively large area compared to the size of a single diode, the details are not visible, and the four scans look quite similar. The scans show that one of the rows has a series of insensitive diodes which is probably due to a break in the aluminium that connects the diodes. The accumulated dose deposited to the 2000 x 2000 µm^2 area was 100 Gy after the four scans.

Figure 6.2 shows the energy deposition distribution of the four scans. The high energy peaks in the spectra have been fitted with a Gaussian function and the mean and standard deviation given by the fitting are shown in the top of the figure.

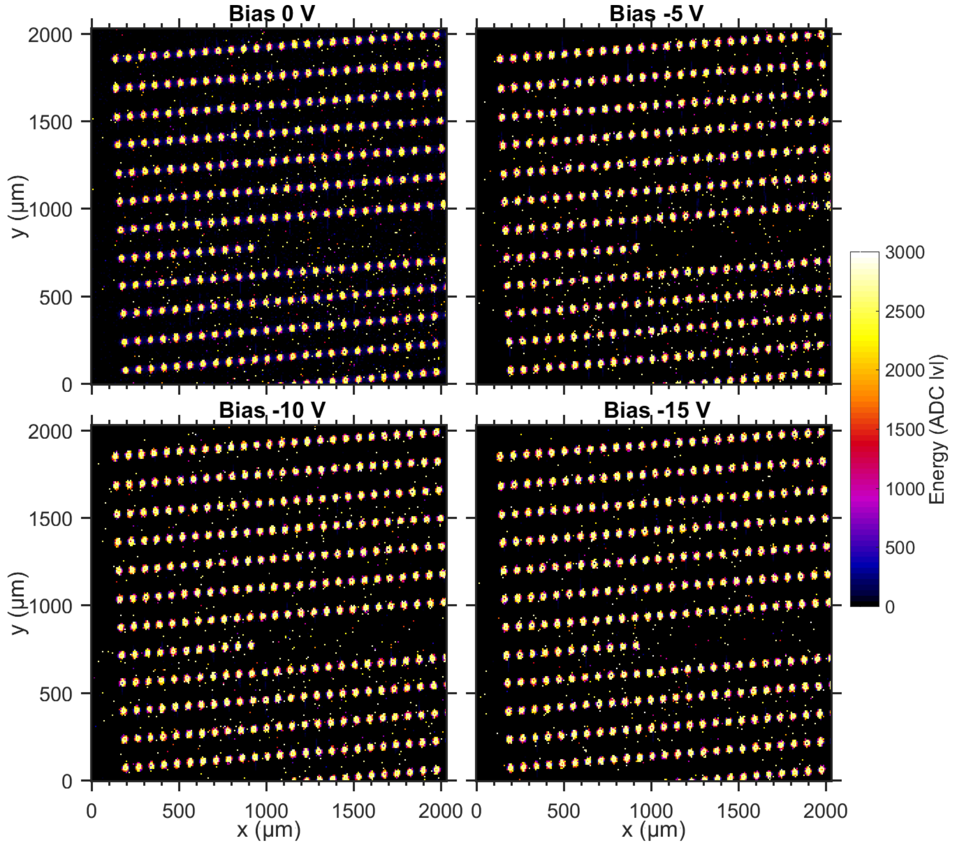

Figure 6.1: Energy deposition maps from four scans over a 2000 x 2000 µm^2 area of the microdosimeter. The scans were performed over the same area with bias voltage: 0, -5, -10 and -15 V.

The ratio of the area from the entire Gaussian function and the area under the whole curve is given under the variable "Gauss area%" and represents the fraction of recorded events from the volume with maximum sensitivity. In an ideal microdosimeter, events should only come from perfect cylindrically shaped SVs with 100% CCE and completely insensitive outside, which would result in a Gauss area close to 100%.

The Gauss area increases significantly from 18% to 37% when the bias voltage increases from 0 to -5 V. The area continues with a slight increase to 41% and 45% as the bias voltage increases to -10 and -15 V, respectively. The fitted mean also increases slightly with increasing bias voltage which was also seen when a test signal was applied at different bias voltages and is due to detector capacitance.

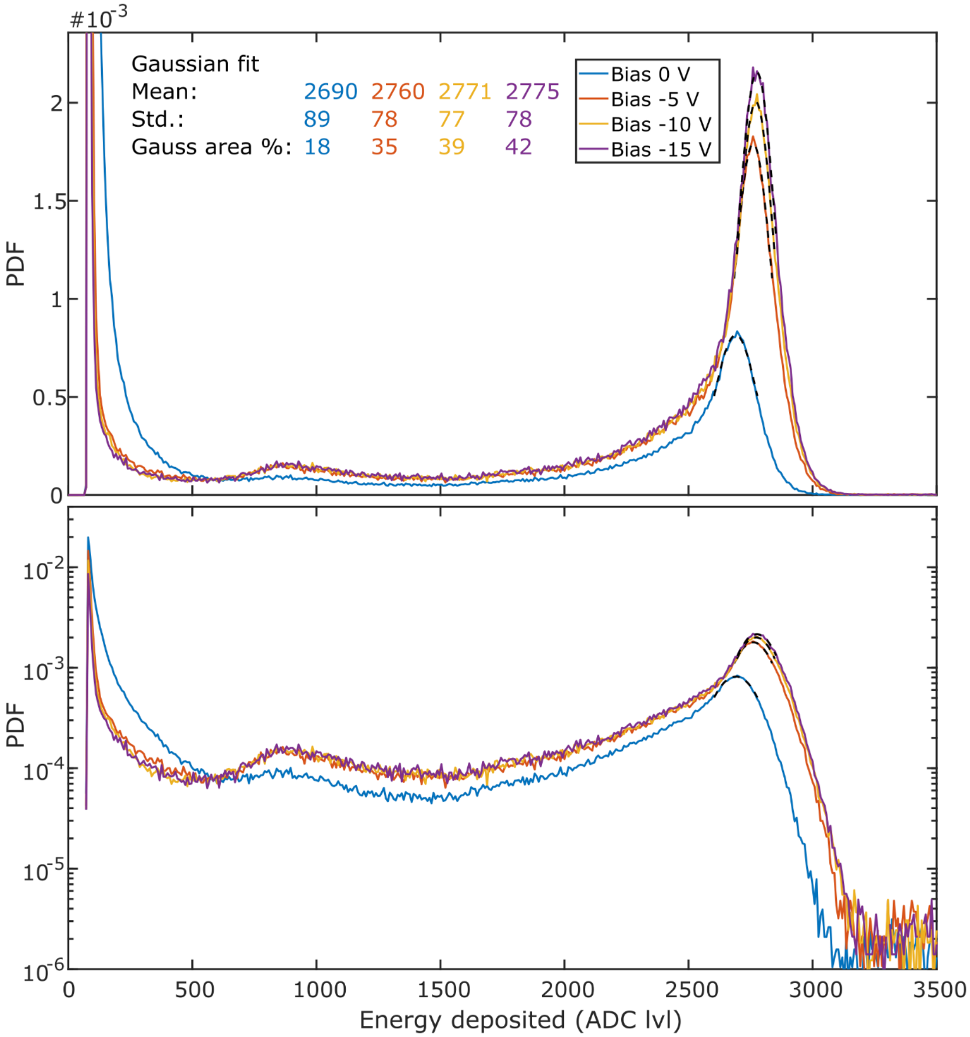

Figure 6.2: Energy deposition spectra from the 2000 x 2000 μm² scans with four different bias voltages with linear (top) and semi-log (bottom) axes. The top half of the peaks have been fitted with a Gaussian function, and the mean and standard deviation for each peak are shown. The “Gauss area%” shows the ratio of the area of the entire Gaussian function to the area of the entire spectrum for each of the spectra.

6.2.2 Medium area scan

Figure 6.3 shows the maps from two scans with -5 and -10 V bias over a 400 x 400 μm^2 area. In the top row of the figure the colour coding covers the entire range of energy depositions (0-3000 ADC lvl), while the bottom row has a colour range of 0-500 ADC lvl to better see where the low energy events are coming from. The detection threshold was reduced from 70 to 40 ADC lvl for these scans making the low energy events more visible.

The maps show circular diodes where the etched central column is not sensitive to radiation and the CCE is homogeneous within the diodes. The opening in the trenches is clearly visible by the dense number of events with low energy to the left and right of each diode. In the low energy maps at the bottom row of Figure 6.3 the unconnected row of diodes are clearly visible as black circles containing no events. It is also evident that the density of low energy events is far higher in the -5 V map than in the -10 V map, and the recorded event rate was 40% higher for the -5 than the -10 V scan. The accumulated dose deposited to the 400 x 400 μm^2 area was 950 Gy after the two scans.

Figure 6.4 shows the energy deposition spectra from the two scans. The relative Gaussian area increases significantly from 21% to 28% when the bias voltage was increased from -5 to -10 V. Note that the relative Gaussian area cannot be directly compared to the previous four scans since a higher detection threshold was used there.

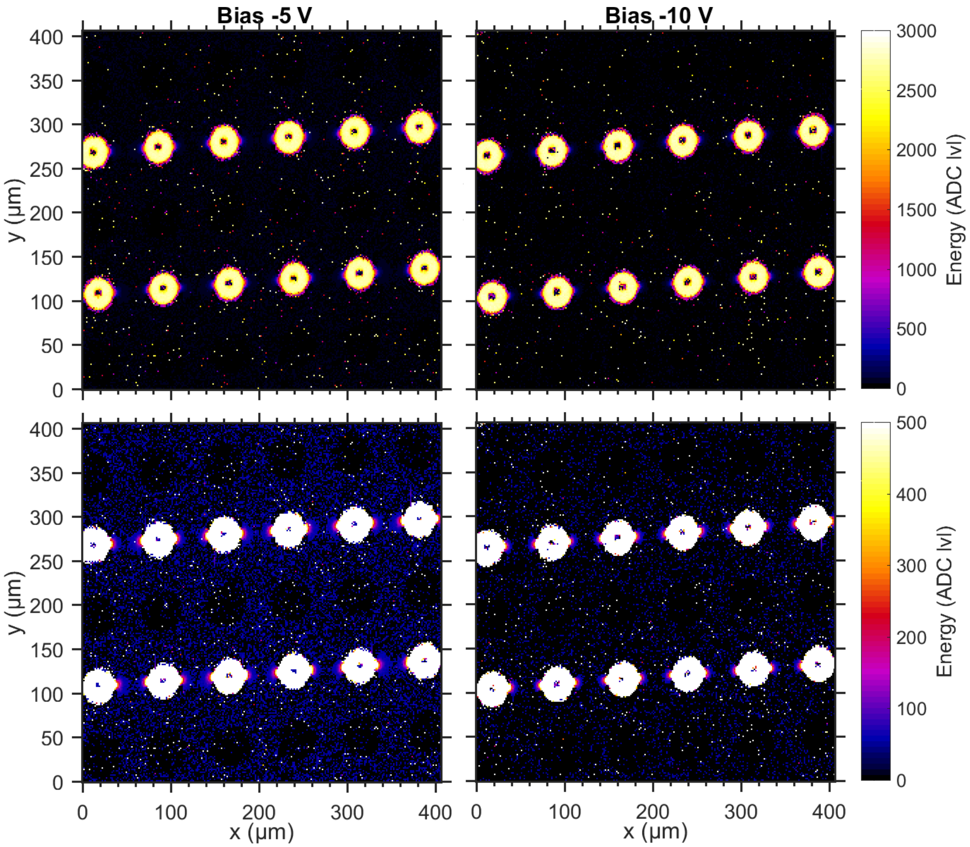

Figure 6.3: Energy deposition maps from two scans over the same 400 x 400 µm^2 area of the microdosimeter with -5 and -10 V bias. The maps in the top row has a colour coded energy range of 0-3000 ADC lvl, while the lower row has an energy range of 0-500 ADC lvl.

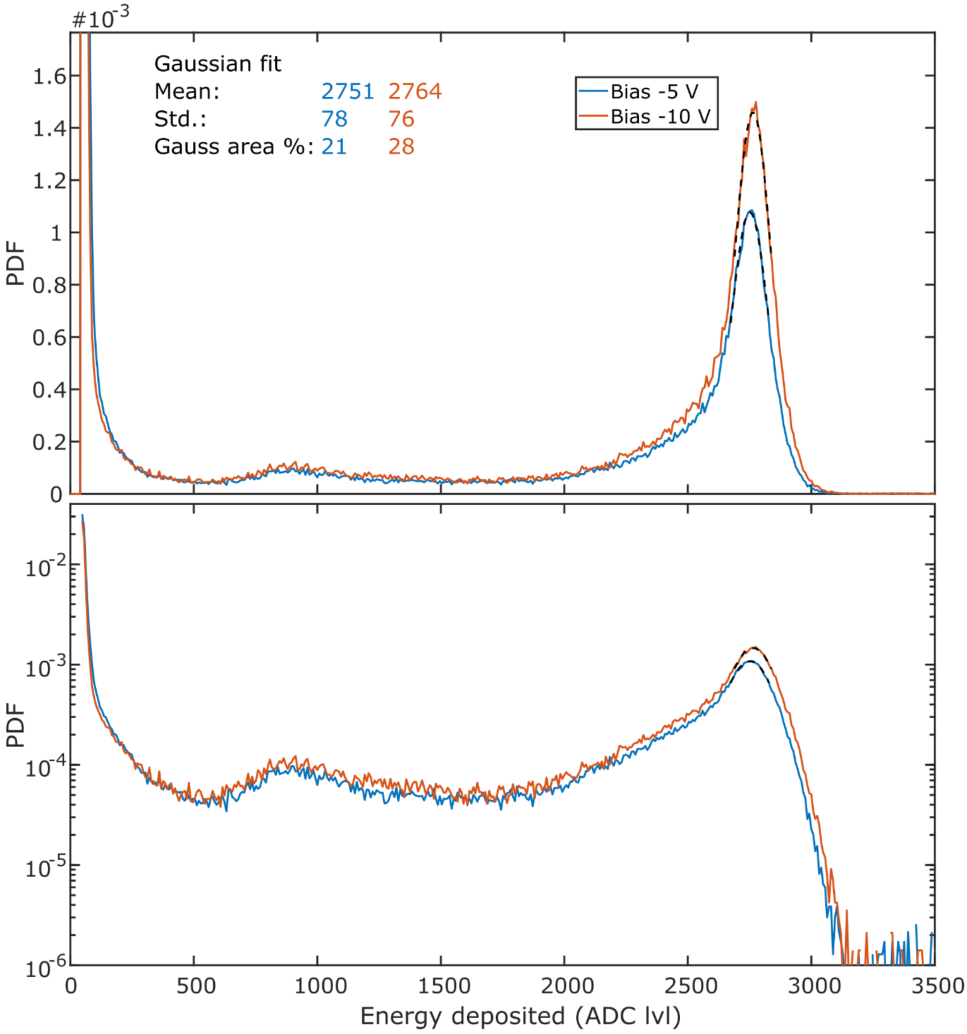

Figure 6.4: Energy deposition spectra from the 400 x 400 µm^2 scans with two different bias voltages with linear (top) and semi-log (bottom) axes. The top half of the peaks have been fitted with a Gaussian function, and the mean and standard deviation for each peak are shown. The "Gauss area%" shows the ratio of the area of the entire Gaussian function to the area of the entire spectrum for each of the spectra.

6.2.3 Small area scan

Figure 6.5 shows the maps from three scans with 0, -5 and -10 V bias of a 140 x 140 µm^2 area, and the energy deposition distributions from the scans are shown in Figure 6.6. The detection threshold was raised to 170 ADC lvl as the noise at 0 V bias had increased due to radiation damage. The maps show four detailed circular diodes, where two are connected and two are unconnected. The etched trenches and columns are clearly insensitive to radiation, and the CCE is homogeneous within the diodes. Apart from the etched trenches and columns, the entire scanned area is clearly sensitive when the microdosimeter is unbiased, resulting in an energy deposition of about 1800 ADC lvl between the diodes. The unconnected diodes are slightly less sensitive than the volume between the diodes when unbiased. The unconnected diodes and the volume between diodes were not sensitive in the previous unbiased scan seen in Figure 6.1.

When the bias voltage was increased to -5 V the unconnected diodes became insensitive to radiation as all the liberated charge within these diodes was collected by the unconnected central N-column. The volume between the diodes are still sensitive, but the events are registered as low energy events at approximately 300 ADC lvl compared to 1800 ADC lvl when unbiased.

When the bias voltage was increased to -10 V, most of the volume between the diodes became insensitive or the energy deposition was below the threshold and thus not visible. However, there is a slightly sensitive strip above and below the left side of the left pixel in Figure 6.5. The opening in the trenches to the left and right of both diodes are slightly sensitive, but the sensitivity is decreasing rapidly with distance from the trench opening. The accumulated dose deposited to the 140 x 140 µm^2 area was 4300 Gy after the three scans.

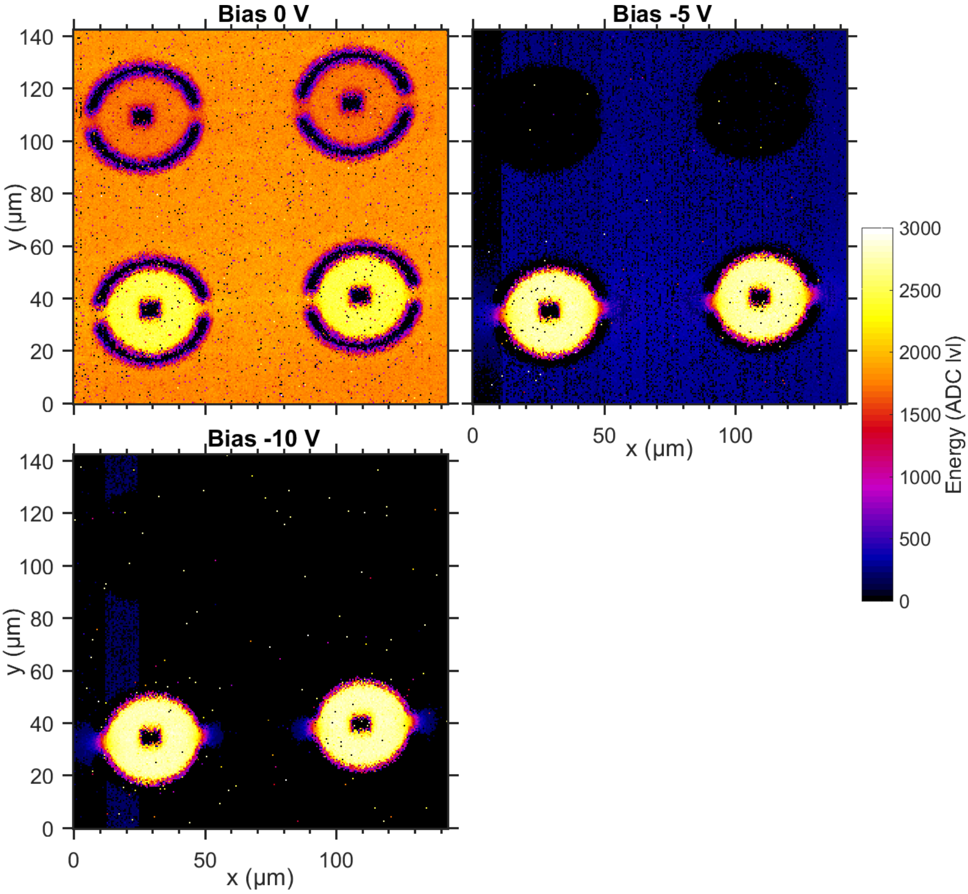

Figure 6.5: Energy deposition maps from three scans over the same 140 x 140 µm^2 area of the microdosimeter with bias voltages: 0, -5 and -10 V.

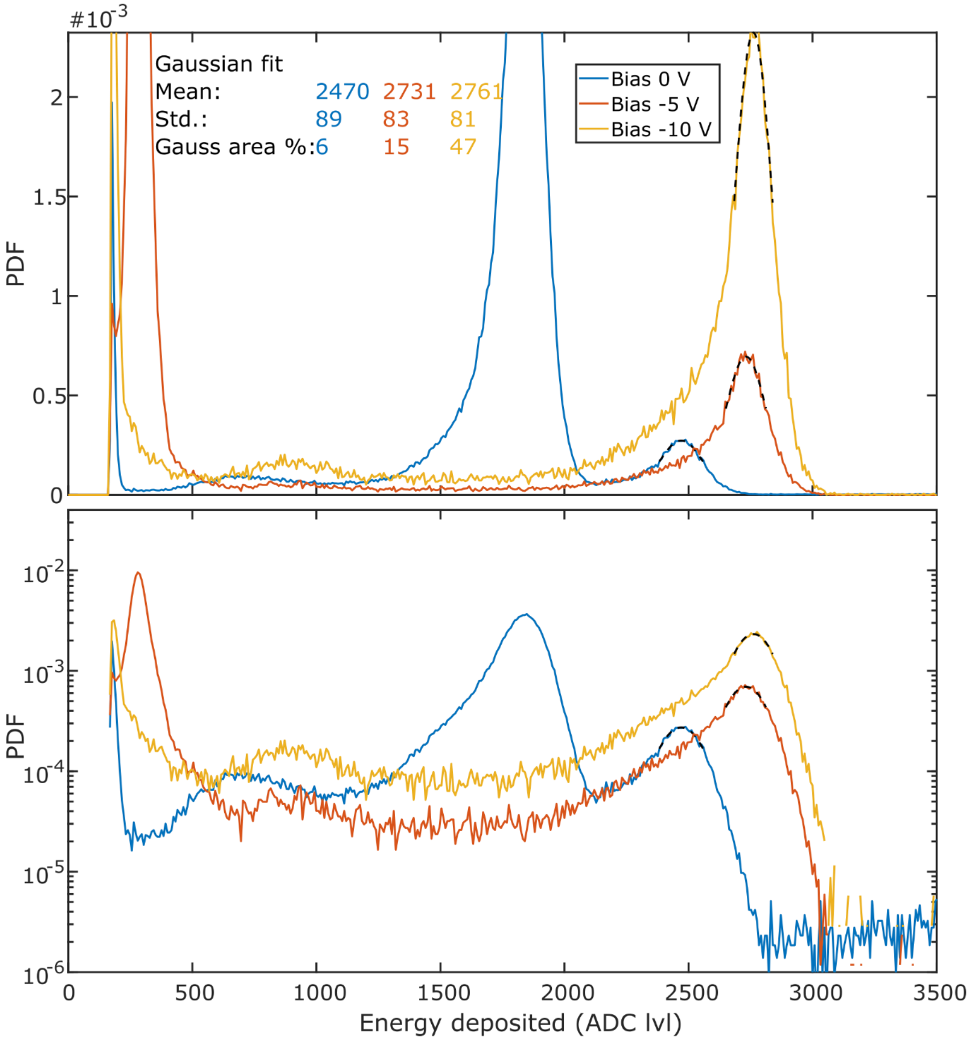

Figure 6.6: Uncalibrated energy deposition spectra from the 140 x 140 µm^2 scans with three different bias voltages with linear (top) and semi-log (bottom) axes. The top half of the peaks have been fitted with a Gaussian function, and the mean and standard deviation for each peak are shown. The "Gauss area%" shows the ratio of the area of the entire Gaussian function to the area of the entire spectrum for each of the spectra.

6.2.4 Radiation damage

Figure 6.7 shows the maps from three scans with 0, -10 and -15 V bias over a 1000 x 1000 µm^2 area, while the energy deposition distributions for these scans are shown in Figure 6.8. The previous 400 x 400 µm^2 and 140 x 140 µm^2 scans are at the centre of the 1000 x 1000 µm^2 scans shown in Figure 6.7, where they are marked with white squares. The threshold was adjusted for each scan due to the large variation in noise at different bias voltages and was 210, 160 and 40 ADC lvl for the bias voltages: 0, -10 and -15 V, respectively.

When the microdosimeter was unbiased the entire scanned area was sensitive, where the connected diodes were the most sensitive, and the unconnected diodes were the least sensitive. The volume between the diodes was also more sensitive within the previously radiated 400 x 400 µm^2 area than outside of it.

When the bias voltage was increased to -10 V the radiation damage effects were significantly reduced, but low energy events were present around the previously radiated 400 x 400 µm^2 area. This is also seen from the large peak at ~300 ADC lvl in the spectrum shown in Figure 6.8. When the bias voltage was further increased to -15 V the radiation damage is almost not visible. There were both fewer low energy events and they were smaller in magnitude. However, there were more events with energy below 100 ADC lvl in the 400 x 400 µm^2 area than outside of it.

While the 400 x 400 µm^2 area show clear effects from radiation damage at all bias voltages, the 140 x 140 µm^2 area does not show an increase in radiation damage effect even though this area received more than 4 times the dose compared to the 400 x 400 µm^2 area.

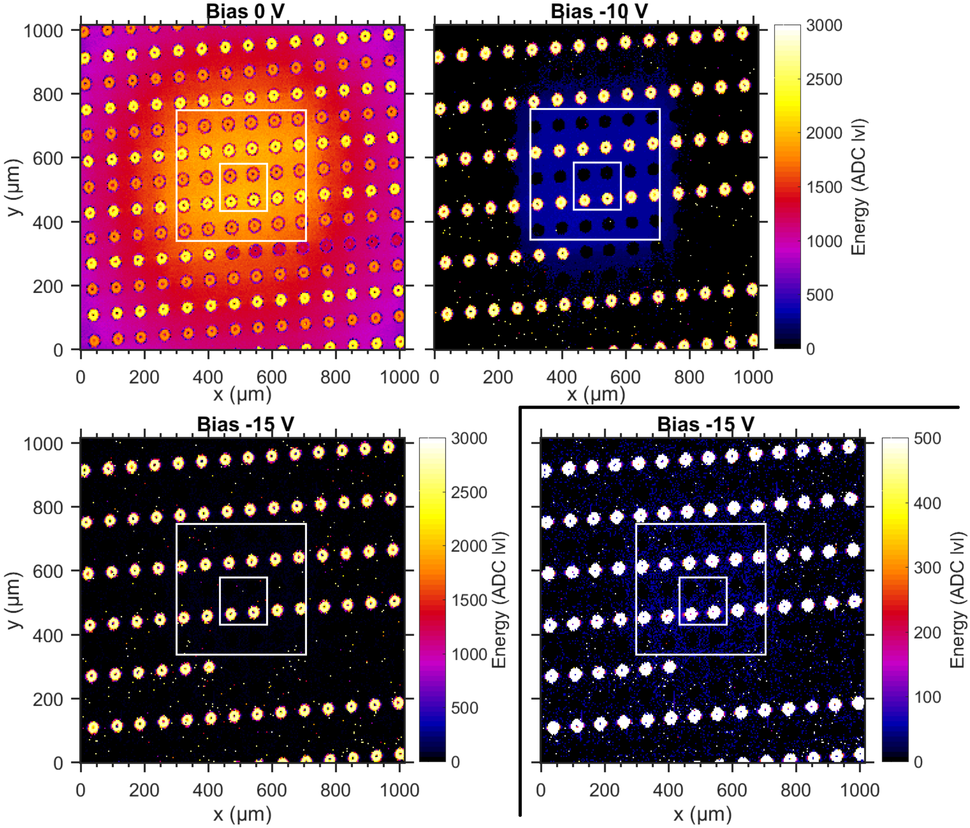

Figure 6.7: Energy deposition maps from three scans over the same 1000 x 1000 µm area with bias voltages: 0, -10 and -15 V. The -15 V scan is also shown at the bottom right with a lower colour-coded energy range. The previously radiated 400 x 400 µm^2 and 140 x 140 µm^2 areas are outlined with white squares. Radiation damage is clearly present since the volume outside the diodes has become more sensitive, but the effect is reduced when increasing the bias voltage.

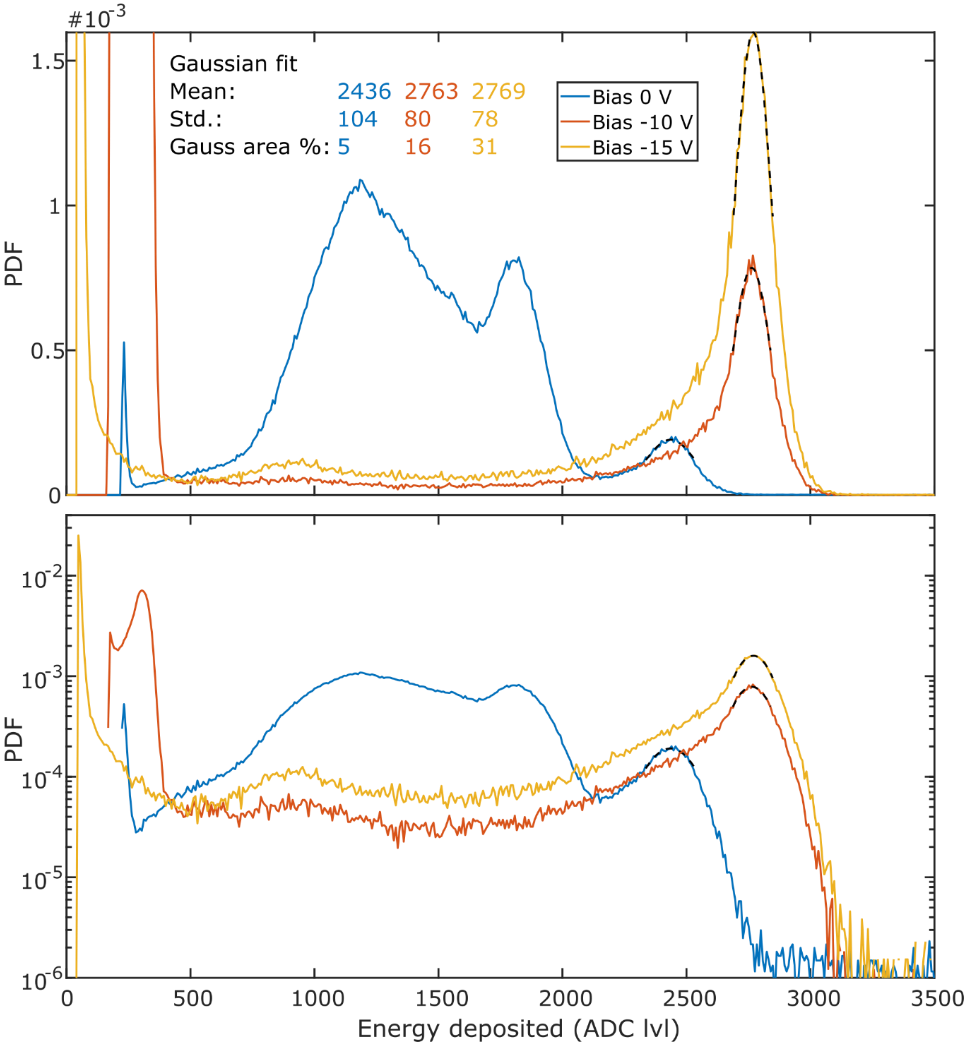

Figure 6.8: Energy deposition spectra from the 1000 x 1000 μm² scans with three different bias voltages with linear (top) and semi-log (bottom) axes. The top half of the peaks have been fitted with a Gaussian function, and the mean and standard deviation for each peak are shown. The "Gauss area%" shows the ratio of the area of the entire Gaussian function to the area of the entire spectrum for each of the spectra.

6.2.5 Single Sensitive Volume

To better see the general features of a single diode, the left diode in the -10 V scan of Figure 6.5 was enlarged, the was resolution increased and the image was smoothed out with Gaussian blurring to produce the image in Figure 6.9. A green circle with 16 µm radius outlines the diode to better see its approximate size and to find the diodes centre with respect to the outer trenches. Two lines cross the diode in the figure, a red along the row of diodes and the diode centre, and a blue along the column and the diode centre. The relative energy deposition along the two lines is shown in Figure 6.10. The map shows that the central column is slightly offset relative to the centre of the circular trenches. The map clearly shows a homogeneous energy deposition in the volume between the central column and the trenches implying a homogeneous CCE. The maps also show that there is an energy deposition gradient near the central column and the trenches. The opening to the left and right of the diode is also evident as this gradient is clearly less steep here.

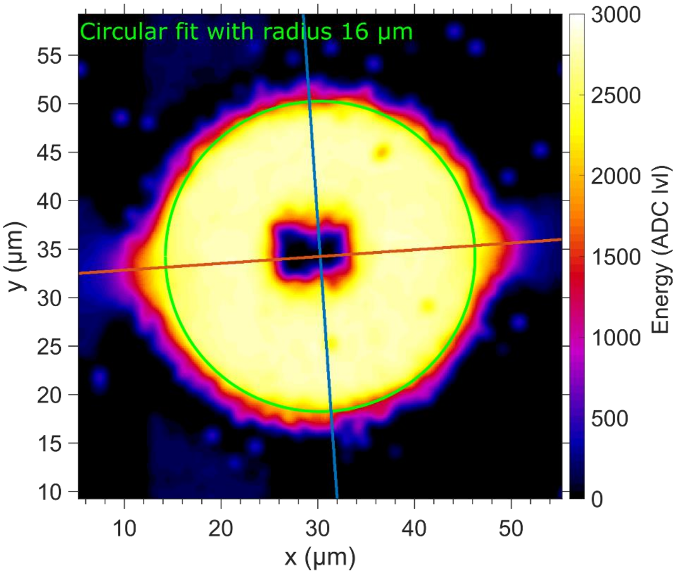

Figure 6.9: The left diode shown in the -10 V scan of Figure 6.5 is enlarged, scaled up and blurred to better see the general feature of a single diode. The green circle with 16 µm radius outlines the approximate size of the diode and is used to estimate the centre of the diode with respect to the outer trenches. Two lines cross the diode, a red along the row of diodes and the diode centre, and a blue along the column and the diode centre. The relative energy deposition along the two lines is shown in Figure 6.10.

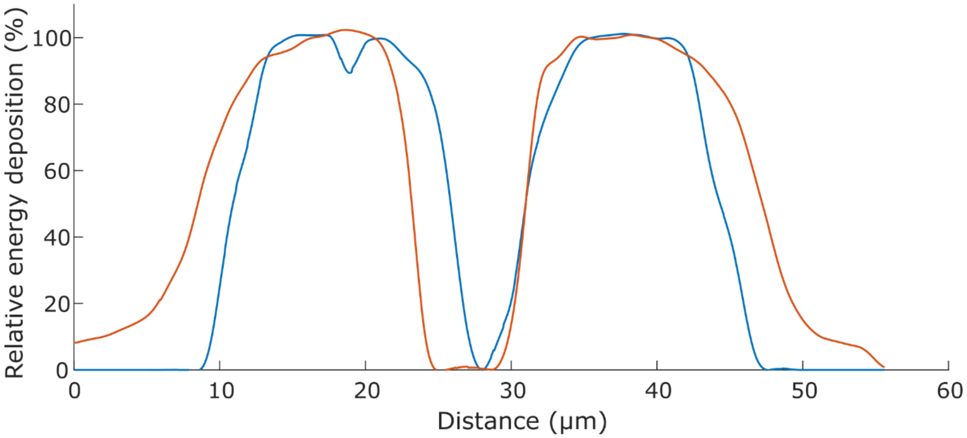

Figure 6.10: Relative energy deposition along the lines crossing the scanned diode in Figure 6.9. The red and blue curve is the energy deposition along the red and blue line in Figure 6.9. The energy deposition is relative to the mean energy deposition of the -10 V peak in Figure 6.6.

The energy deposition gradients and the approximate size of the diode are better seen in Figure 6.10. The diameter of the diode is defined as the distance between the first and last occurrence of a predefined *cut-off* energy deposition relative to the maximum energy deposition. As an example, the distance between the first and last instance of 90% energy deposition is 29.4 µm and 31.1 µm for the blue and red plot, respectively. As the energy deposition gradient is steeper for the blue line than the red that runs through the diode opening, the size difference between the two becomes larger for lower cut-off energies.

The nominal diameter of the SV was estimated by plotting the relative energy deposition along 180 lines of the diode running through the centre with a 1° angle increment. The distance between the first and last instance of nine cut-off energies between 10% and 90% was calculated for each line and is shown in Table 6-1. The mean sensitivity gradient near the trenches can be calculated from the table, and the sensitivity drops from 90 to 10% in $\frac{39.8\ \mu\text{m} - 30.6\ \mu\text{m}}{2} = 4.6\ \mu\text{m}$. The area within the 90% limit is 730 µm^2 while it is 1240 µm^2 within the 10% limit.

Table 6-1: The mean and standard deviation of the diameter of the diode in Figure 6.9 calculated by the distance between the first and last register of the energy cut-off relative to the maximum energy deposition.

Relative energy cut-off	90%	80%	70%	60%	50%	40%	30%	20%	10%
Mean diameter (μm)	30.6	31.8	32.7	33.5	34.2	35.0	36.0	37.0	39.8
Standard deviation (μm)	0.9	1.1	1.3	1.4	1.5	1.6	1.8	2.2	3.9

Thus, for every 100 events that occur within the 90% limit, approximately 80 events will occur in the region between the 90% and 10% limit if the beam is perpendicularly incident onto the microdosimeter surface.

The nominal diameter for a range of cut-off energies was only calculated for a single SV, but is expected to be representable for all SVs as the sensitivity maps in Figures 6.3 and 6.5 shows apparently identical SVs.

6.3 Discussion

The microdosimeter works well with the alternative way of biasing the P^+ trench instead of the N^+ column, although a direct comparison between the two was not possible due to unstable dark currents when the N^+ columns were biased.

Radiation damage was clearly visible for the 140 x 140 and 400 x 400 μm^2 area which received 950 and 4300 Gy, respectively. The radiation damage increased the amount of low energy events between the diodes, but the effects were suppressed by increasing the bias voltage. The increasing sensitivity between the diodes is due to liberated charge in the oxide layer where the electrons escape due to their high mobility, but the holes are trapped. The trapped holes in the oxide layer attract electrons at the surface of the silicon which has the same effect as n-type doping at the surface. This creates a small pn-junction between the surface and the p-type substrate, and it makes the surface of the silicon slightly conductive such that some of the liberate charge outside the diodes can reach the N^+ column electrode. The hole concentration in the oxide layer saturates and reaches a maximum concentration of about 3×10^{12} cm^{-3} at about 1000 Gy (Seidel, 2001). This is also seen here, where there is not a noticeable increase in the low energy event between the 400 x 400 μm^2 area that received 950 Gy and the 140 x 140 μm^2 area that received 4300 Gy in Figure 6.7. This kind of radiation damage is known as *surface damage*.

In the measurements without bias voltage, the mean of the high energy peak was reduced by 8% between the first 2000 x 2000 μm^2 scan and the 140 x 140 μm^2 scan. This is likely due to an increasing loss of charge due to *bulk damage* creating trapping and recombination centres (Lindström, 2003). This occurs when the ^{12}C ions scatter off the silicon nuclei and transfers enough energy to displace the silicon atoms. This creates both vacancies in the lattice and atoms that are lodged between lattice positions. At -5 V bias the mean decreases 1% between the 2000 x 2000 μm^2 scan and the 140 x 140 μm^2, and no significant decrease was seen at -10 and -15 V. This is explained by the increased strength of the electric field in the diode that leads to swifter charge collection and thus lower probability of trapping and recombination.

Although the two ways of biasing could not be compared directly, they can be compared to the results in (James et al., 2018) where the N^+ column was biased in microbeam tests with 5.5 MeV ^{4}He conducted on the same type of microdosimeter in the same beamline at ANSTO. The microbeam measurements were conducted before and after the microdosimeter was radiation damaged in a Ti- and Li-beam with an integral fluence of $5 * 10^8$ cm^{-2}. The microbeam experiment showed that the unconnected diodes and the volume between the connected diodes had become slightly sensitive at 10 V bias. By comparison, the 140 x 140 μm^2 and the 400 x 400 μm^2 area marked in Figure 6.7 received a fluence of 2 x 10^9 and 1 x 10^{10} cm^{-2}, or 950 and 4300 Gy, from ^{12}C. When biased to -10 V, the low energy events due to radiation damage in the current work was similar to those found by James et al. (2018). However, since only 10 V bias was used by James et al. (2018) it is not possible to know if 15 V bias applied to the N^+ column would reduce the effects from radiation damage as effectively as -15 V applied to the P^+ trench as seen in Figure 6.7. Applying negative bias at the P^+ trench would likely decrease the sensitivity outside the diodes more effectively if there had been a grounded N^+ electrode between the diodes to collect the liberated electrons.

The sensitivity gradient near the P^+ trench seen in Figure 6.9 and 6.10, and summed up in Table 6-1, show that a large fraction of events occur in the gradient. In the energy deposition spectra shown in this and the previous chapter for alpha and ^{12}C particles, the sensitivity gradient near the trench creates an almost constant event rate from the detection threshold up to the high energy peak. These events are not visible in the simulations without a sensitivity gradient, seen in the previous chapter. The sensitivity gradient is believed to come from the P^+ dopant concentration gradient after the gas doping.

The sensitivity gradient can be added to the MC model by scaling the energy depositions from each step with a sensitivity function that depends on the distance from the centre of the SV. This would produce a more accurate MC model, and the effects from the sensitivity gradient could be determined by running the simulations with and without applying the sensitivity function.

6.4 Summary

The IBICC technique with 24 MeV C-12 ions was applied to trenched 3D structure microdosimeters. The microdosimeters were biased in an alternative way, where negative bias was applied to the P+ trench to see if the amount of low energy events from outside the SVs would be repelled.

The alternative way of biasing the P+ trench works well, however the results are inconclusive whether the alternate way of biasing reduced the number of low energy events from outside the SVs.

The effects of surface damage were effectively suppressed by increasing bias voltage, and the results suggest the bias voltage should be 15 V or above if there is risk of surface damage. Slight effect of bulk damage is seen at 0 V, but is not visible at voltages above 10 V.

A sensitivity gradient is observed near the trenches of the SVs which makes up about 44% of the cross-sectional area of the SVs. This gradient could be added to MC simulations to get more accurate simulation results.

7. Tissue correction function

Silicon is not tissue equivalent and the measurements from the microdosimeters must be corrected to be relevant for radiobiology and to be able to compare the results with those of a TEPC. Generally, a larger amount of energy is deposited in a silicon volume than in a tissue volume of equal size and shape, and thus the single event energy deposition or lineal energy in a silicon volume has to be reduced to be comparable to that in a tissue volume. Two methods for creating tissue equivalent factors were presented in section 3.3.2 that scales the measurements. However, as the stopping power ratio between tissue and silicon depends on particle energy (Figure 3.3), a constant scaling factor will result in an error that increases rapidly as the ion energy fall below 10 MeV/u. Thus, the error from a constant correction factor in a beam will be at a maximum near the Bragg peak (BP) and in the distal dose fall off (DDF), which are critical regions in therapeutic beamlines for cancer treatment. This became apparent when performing the microdosimetric characterization of the low energy proton beamline presented in chapter 8.

The solution was the tissue correction function for protons presented here, which is based on simulated energy deposition in silicon and tissue from a large range of proton energies below 200 MeV. The method is created for proton energies used in medicine, and does not need a second detector stage that measures the entire proton energy as used by Agosteo et al. (2010); (2008; 2009).

7.1 Method

The tissue correction for a single proton energy, E_p, is defined as

$$\frac{\overline{y_T(E_p)}}{\overline{y_{Si}(E_p)}}, \tag{7.1}$$

where $\overline{y_T(E_p)}$ and $\overline{y_{Si}(E_p)}$ are the mean lineal energy in tissue and silicon, respectively. By simulating the energy deposition in a thin slab of tissue and silicon

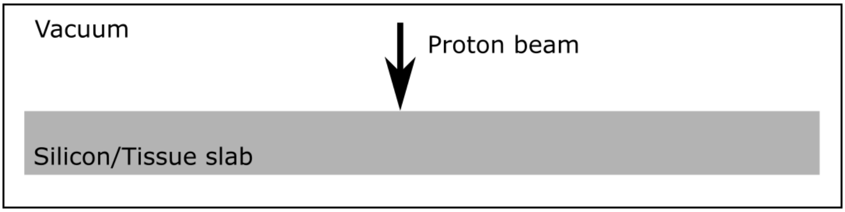

Figure 7.1: MC simulation setup, where a monoenergetic proton beam is perpendicularly incident on a slab of silicon or tissue.

for a range of proton energies, a generic correction function can be created from a polynomial fit to the correction from equation (7.1). However, since the proton energy, E_p, is generally not known when the function is used, the corrections are fitted as a function of the mean energy deposition in silicon, $\overline{\epsilon_{Si}(E_p)}$, creating an energy deposition tissue correction function $\kappa(\epsilon_{Si})$.

The simple MC simulation model used to record the energy depositions is shown in Figure 7.1. A silicon or tissue slab was positioned in vacuum with a monoenergetic proton beam perpendicularly incident on the slab surface. The simulation was run for a range of proton energies between 0.6 and 200 MeV for a 9.1 μm thick silicon slab and for 12.0, 12.5 and 13.0 μm thick tissue slabs. 9.1 μm thick silicon was used since this was measured for the microdosimeter by L. T. Tran, Chartier, Prokopovich, et al. (2018). $3 * 10^4$ protons were simulated in each run, and the energy deposition was recorded for each proton. The slab thicknesses were used as the mean chord length when calculating the lineal energy. The tissue material used in the simulations is identical to the material *muscle (skeletal)* defined in (ICRU, 1989).

7.2 Results

The simulation results are shown in Figure 7.2, where $\overline{y_T}/\overline{y_{Si}}$ for each of the tissue thicknesses is plotted as a function of the energy deposition in silicon, $\overline{\epsilon_{Si}}$. The 34 datapoints in each plot represents a single proton energy, and a cubic function is fitted to each of the plots. The three plots are nearly identical for energy depositions below 300 keV, which is from proton energies above 1.5 MeV.

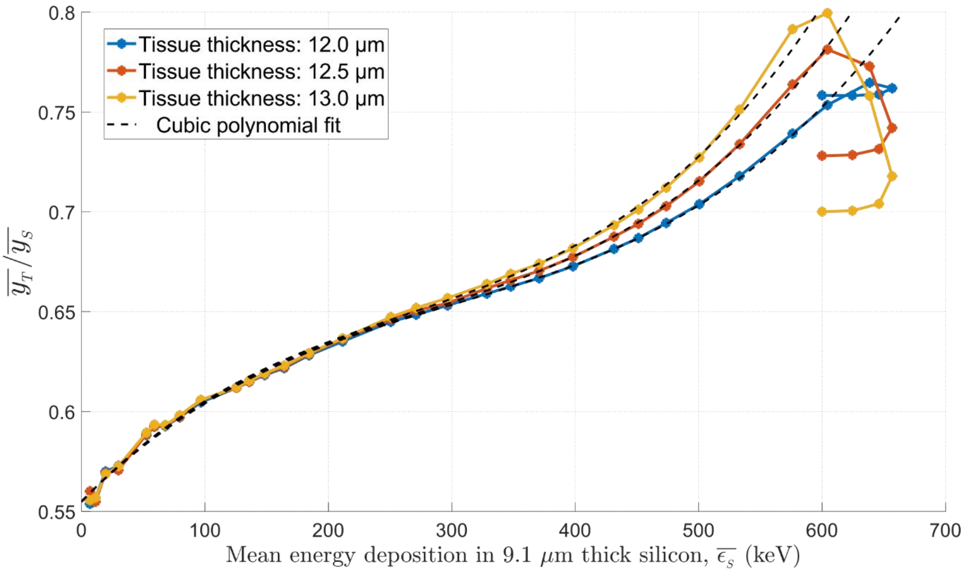

Figure 7.2: MC simulation of the tissue correction ($\overline{y_T}/\overline{y_{Si}}$) as a function of the mean energy deposition in silicon ($\overline{\epsilon_{Si}}$) from proton energies in the range 0.6 to 200 MeV from three different tissue thicknesses. Each data point represents a specific proton energy incident on the simulated silicon and tissue slab and the curves have been fitted between 0 and 600 keV energy deposition.

For proton energies below 0.65 MeV, all protons stop in all the thicknesses simulated and $\overline{y_T}/\overline{y_{Si}}$ becomes equal to the ratio of chord lengths, $\overline{l_{Si}}/\overline{l_T}$. This creates the "curl" at the end of the plots. The plots also show that the proton energy that stops in exactly 9.1 µm silicon also stops in 12.0 µm of tissue.

Three tissue correction functions $\kappa(\epsilon_{Si})$ were created by fitting the the three plots in Figure 7.2 for $\overline{\epsilon_{Si}}$ between 0 and 600 keV with cubic functions. The coefficients for the three correction functions are shown in Table 7-1. The functions are restricted such that the maximum value for $\kappa(\epsilon_{1,Si})$ is for 600 keV energy deposition, shown in the last column of Table 7-1.

Table 7-1: Coefficients for the three cubic regression fits shown in Figure 7.2. The cubic functions are used as tissue correction functions, $\kappa(\epsilon_{Si}) = a\epsilon_{Si}^3 + b\epsilon_{Si}^2 + c\epsilon_{Si} + d$*, where* ϵ_{Si} *is the energy deposited in silicon given in keV. The last columns show the maximum permitted value for* $\kappa(\epsilon_{Si})$ *when the energy deposition is above 600 keV*

Tissue thickness (μm)	a (keV^{-3})	b (keV^{-2})	c (keV^{-1})	d	$\kappa(\epsilon_{1,\mathrm{Si}} > 600\ \mathrm{keV})$
12.0	1.619E-09	-1.454E-06	6.183E-04	0.555	0.752
12.5	1.933E-09	-1.600E-06	6.386E-04	0.555	0.779
13.0	2.156E-09	-1.691E-06	6.525E-04	0.555	0.803

7.3 Discussion

The three correction functions transfer the lineal energy in a silicon SV with mean chord length of 9.1 μm into the lineal energy of a tissue composed SV with mean chord length of 12.0, 12.5 and 13.0 μm. The range of the functions is seen from the two last columns in Table 7-1, which match well with the stopping power ratio for protons seen in Figure 3.3, which is between 0.547 and 0.765 keV for proton energies between 200 and 0.25 MeV.

Since the proton energy that on average stops in 9.1 μm of silicon also stops in 12.0 μm of tissue, it seems natural that it is the 12.0 μm tissue equivalent function that would give the best results, however, this might not be the case. An optimal correction function would be based on the proton energy, and not the energy deposition, and is expected to increase as the proton energy fall to 0.25 MeV (Figure 3.3). For the correction functions, the maximum energy deposition is at 600 keV from 0.73 MeV protons. When the proton energy falls below 0.73 MeV, the energy deposition decreases and consequently the correction functions also decrease, resulting in large errors for proton energies below 0.73 MeV. By using the 12.0 μm tissue correction function, protons with energy near 0.73 MeV is corrected with little error, but the error increases rapidly below 0.73 MeV. By using a tissue correction function for a slightly larger tissue SV, the error is higher for protons near 0.73 MeV, but is reduced for protons below 0.73 MeV compared to the 12.0 μm tissue correction function. Consequently, the integral error for protons below 1 MeV might be lower for the 12.5 or 13.0 μm correction function compared to the 12.0 μm function. The three correction functions are assessed for a low energy beamline presented in section 8.2.3.

This method has similarities to the one presented in section 3.3.2 Tissue Equivalence using equation (3.5) by Bolst, Guatelli, et al. (2017). Both methods compare the simulated lineal energy in a silicon SV and a slightly larger tissue SV to find an equivalent size, but Bolst, Guatelli, et al. (2017) found a best fitted constant correction factor instead of a function. The study showed that a correction factor 0.57 gave best results for a 290 MeV/u ^{12}C beam at several depths in a water phantom. The study showed that the correction factor of 0.57 yielded very good results except near the BP. At the BP, the tissue corrected $\overline{y_F}$ was approximately 20% lower than that from tissue composed SVs, while results for $\overline{y_D}$ were not shown. Several other studies using this method have found that a correction factor of 0.58 is the best fit in medical proton and ^{12}C beamlines as well as high energy ^{14}N and ^{16}O beamlines (Bolst, Tran, et al., 2017; Debrot et al., 2018; L. T. Tran, Bolst, et al., 2018; L. T. Tran, Chartier, Bolst, et al., 2018; Linh T. Tran et al., 2017). However, these studies did not show the relative difference between the simulated tissue corrected lineal energy from silicon SVs and from tissue composed SVs which makes it difficult to assess the accuracy of the tissue correction factor. An optimal constant correction factor of 0.57-0.58 agrees well with the functions created here as all three functions are between 0.555 and 0.600 for energy depositions below 90 keV from proton energies above ~7 MeV. As the maximum of the functions is approximately 0.78, which is 34% higher than 0.58, the correction in the mentioned work, the correction error is expected to be large at the BP and in the DDF.

Since an optimal correction function should be based on the proton energy, two protons with the same energy should be corrected equally. However, the two protons will deposit a different amount of energy due to path length variations through the SV and energy straggling. This creates a significant error for a single measurement but is expected to even out for many events and produce spectra with little error. This effect is expected to widen the spectra slightly as the proton that deposits the most energy will get a slightly larger correction than the proton depositing the least.

The correction functions for higher proton energies is unbalanced with respect to generated delta electrons. The simulation takes into account that the protons transfers energy to delta electrons in an SV that leave the SV, but it does not take into account that the same proton would also generate delta electrons prior to entering the SV that would enter the SV alongside the proton. This could be fixed by having a tissue equivalent absorber in front of the slab used in the simulations that would generate a field of secondaries. The slab must then be changed to a cylindrical SV like those in the microdosimeter since the delta electrons generated prior to the SV has a probability of missing it.

As more than 70% of the dose is deposited by electrons from a 160 MeV proton in water (Liamsuwan, Uehara, Emfietzoglou, & Nikjoo, 2011), it is important that the electrons also are corrected with little error. The maximum electron energy from 200 MeV protons is approximately 450 keV and represents the upper electron energy that will be corrected by the function. The electron stopping power ratio in tissue over silicon from 450 keV electrons is 0.55 according to ESTAR data (Berger et al., 2017). A 450 keV electron will on average deposit 3.5 keV in in 9.1 µm of silicon, according to ESTAR data, and the tissue correction function results in a 0.56 correction for a 3.5 keV energy deposition. A 30 keV electron has a CSDA range of approximately 9.1 µm and is thus regarded as the lowest electron energy that can cross the silicon volume. The stopping power ratio in tissue over silicon for a 30 keV electron is 0.57 and the tissue correction function also results in 0.57 for an energy deposition of 30 keV. Thus, the correction function is assumed to work accurately for electrons as well.

The functions presented here are created for protons but can be created for any ion. However, when the particle momentum increases, the cross sections for nuclear interactions also increase, creating a more varied field of electrons and ions. This was shown by Liamsuwan, Hultqvist, Lindborg, Uehara, and Nikjoo (2014), where a simulated ^{12}C beam creates a much more varied field of secondaries, and the secondary ions deposit a much larger fraction of the dose compared to a proton beam. Thus, a correction function for ions heavier than protons must not produce too large error for the secondary ions. A solution might be to create a correction function for each ion species which is valid in a specific energy interval, like:

$$\kappa(\epsilon_T) = \begin{cases} \kappa(\epsilon_{Si,proton}), & \epsilon_{Si} < E_1 \\ \kappa(\epsilon_{Si,^4He}), & E_2 > \epsilon_{Si} \geq E_1 \\ \kappa(\epsilon_{Si,^7Li}), & E_4 > \epsilon_{Si} \geq E_3 \\ \ldots \end{cases} \tag{7.2}$$

This might be complicated but should produce better results than a constant factor. It might also be possible to simplify and merge several ions into a group as ^{12}C and ^{16}O likely have similar correction factors for a wide range of energies.

7.4 Summary

Since silicon is not a tissue equivalent material the lineal energy in a silicon SV must be corrected to be equivalent to the lineal energy in a tissue composed SV. Previous work has corrected the measurements in silicon by simply lowering the measured lineal energy or energy deposition by a constant factor. To increase the accuracy of the correction, a tissue correction function was developed that depends on the energy deposition in the silicon volume. Three correction functions for protons were developed by comparing the lineal energy in a 9.1 µm thick silicon volume to the lineal energies in 12.0, 12.5 and 13.0 µm thick tissue composed volumes. The function is valid for protons energies up to 200 MeV and is expected to produce valid results for secondary electrons as well.

The three correction functions are compared in the simulation of a 15 MeV proton beamline described in chapter 8 to see which performs the best, and to compare them to a constant correction factor as used in previous work.

8. Measurrements in a low energy proton beamline

An extensive review of proton RBE in vitro as a function of the dose averaged LET was conducted by Paganetti (2014) and the results showed a large spread in the experimental data. Similarly, a comparison of proton RBE-models by Rørvik et al. (2018) found large differences between these models, showing the need to reduce uncertainties. The uncertainties are likely due to variations in both biological and experimental conditions, and by using accurate and standardized measurement equipment the experimental uncertainties might be reduced. In the study by Paganetti (2014), the reported LET of the underlying studies were not calculated in a consistent manner, and for the studies that did not report the LET, it was estimated from a generic MC model. By measuring the beam quality at the precise location of the cells in radiobiological cell experiments used for RBE modelling, the uncertainties in RBE as a function of beam quality might be reduced. Silicon microdosimeters are good candidates for such measurements, as they have excellent spatial resolution and can handle much higher beam intensities than traditional TEPCs without suffering from pile-up.

The L_{st} microdosimeter in chapter 5 was used to measure the microdosimetric spectra along the Bragg curve in a polyamide absorber of a 15 MeV proton beamline used for radiobiological experiments. The beamline was originally set up for irradiation of electronic components (Røed, 2009) and previously investigated in a FLUKA based MC model to determine the LET (Dahle et al., 2017). The measurements from the current work were supplemented by GATE simulations of the microdosimeter in the beamline and had four aims:

- Investigate how well the simulation model reproduced the measurements.
- Evaluate the tissue correction functions from chapter 7
- Investigate how the relative depth dose distribution from the microdosimeter compared to a commercial ionization chamber (IC) for radiation therapy.
- Conduct a microdosimetric characterization of the beamline used for radiobiological experiments.

8.1 Setup & method

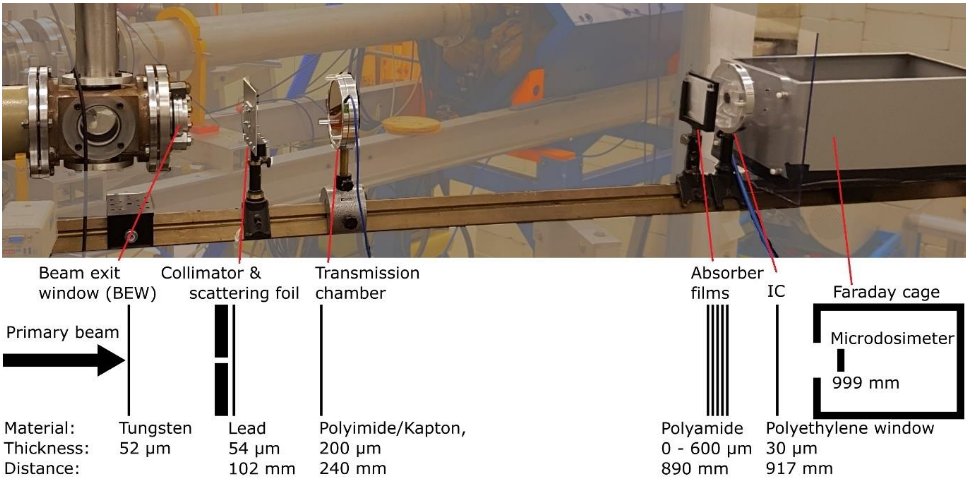

Figure 8.1: Image and schematic of the experimental setup. The thickness, material, and distance from the BEW for all the objects in the beam is shown below them in the schematic.

The experiment was performed in a proton beamline at the Oslo Cyclotron Laboratory (OCL) which was operated at approximately 15 MeV. The experimental setup is shown in Figure 8.1 where the material, thickness, and distance from the beam exit window (BEW) for all objects in the beam are shown. The lowest possible beam flux at the BEW was approximately 10^{10} protons/s which would result in pile-up events, and many events during detector dead time. This would increase the errors in the energy deposition spectra and depth dose distributions. The intensity at the position of the microdosimeter was lowered by placing a collimator and scattering foil 10 cm after the BEW, shown in Figure 8.2. The collimator had a 1 mm diameter opening, and the lead scattering foil was 54 µm thick. The beam flux behind the collimator and scattering foil was monitored by a transmission chamber from PTW (Type 7862) which was read out by a Unidos E Universal Dosemeter, also provided by PTW.

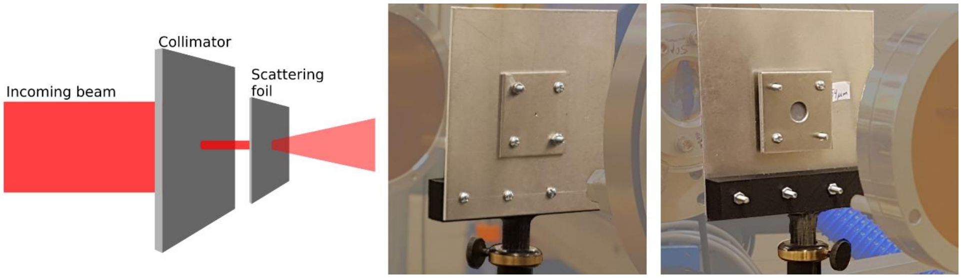

Figure 8.2: Collimator and scattering foil placed 10 cm after the BEW to reduce the beam flux at the microdosimeter surface. The collimator is a 1 mm diameter hole in a 2 mm thick aluminium, and the scattering foil is a 54 µm thick lead.

Layers of polyamide (nylon6) films with a density of 1.13 g/cm^3 were used as absorbers and were held by a plastic frame with a 70 x 70 mm^2 opening. According to the vendor the films had a thickness of 15 µm with 20% uncertainty. The uncertainty was lowered by measuring 5 points on each film with a Filmetrics F10-RT thin-film analyser, and the centre of each film was measured with a Mitutoyo Series 293 QuantuMike Micrometer for verification. The measurements gave an average film thickness of 16.4 µm, which is equivalent to 19.2 µm of water. The standard deviation of the 5 measured point on each film was calculated, and the mean standard deviation was 0.2 µm. This indicates that the film thickness was near homogenous.

Measurements with the IC and microdosimeter were conducted at 13 depths of the absorber and single films were added between measurements near the BP and in the DDF. Measurements with the IC and microdosimeter were performed alternately at every depth, and the IC was removed when using the microdosimeter. The IC was a PTW type 34045 Advance Markus Chamber and was read out by a Standard Imaging MAX-4000 electrometer.

The microdosimeter was placed inside a 1 mm thick steel box that served as both a light tight box and a Faraday cage. The beam was let through a 6 mm hole and the microdosimeter was fixed to the box 2 cm from the beam opening. The readout electronics used for single event measurements was as described in section 5.1.2, except that the shaping amplifier used for this experiment was a Tennelec 244 with a 1 µs shaping time.

When the lineal energy was calculated, the mean chord length, $\bar{l}$, was assumed to be equal to 9.1 µm, the height of the SVs as measured by L. T. Tran, Chartier, Prokopovich, et al. (2018). This was assumed since the beam was perpendicular onto the microdosimeter surface and the distance between the absorbers and microdosimeter was relatively long.

Calibration was conducted by measuring an ^{241}Am alpha spectrum with the microdosimeter in air. The source was fixed in a frame that was mounted on the microdosimeter PCB (Figure 3.10) directly above the microdosimeter to get accurate measurements. The distance between the source and the microdosimeter was 14 mm and a MC simulation was used to determine the energy deposition in the microdosimeter.

8.1.1 Simulation setup

The experimental setup shown in the schematic of Figure 8.1 was modelled in a GATE MC simulation, where the model shown in Figure 4.1 was used for the microdosimeter. The energy deposited in the SVs for each event was written to file and one simulation was run for every thickness of the absorber used in the experiment. The production cuts for electrons in the SV, the aluminium and oxide layer above the SVs were 250 eV, while it was 1 keV in the 30 mm of air in front of the microdosimeter.

The microdosimeter was also simulated as composed of tissue, and the results were compared to the tissue corrected results from the silicon microdosimeter. The three correction functions, $\kappa(\epsilon_{\mathrm{Si}})$, from chapter 7 were used to correct the lineal energy from a simulated silicon microdosimeter. The tissue corrected dose-mean lineal energy, $\overline{y_D}$, from the three functions were compared to $\overline{y_D}$ from the simulated tissue composed microdosimeter with equivalent SV heights of 12.0, 12.5 and 13.0 µm. The radius of the tissue composed SVs were increased such that height to radius ratio was equal to that of the silicon SVs. The tissue composed microdosimeter were also simulated with 1 µm high SVs to investigate the significance of SV size.

8.1.2 Depth dose and beam energy estimation

The relative dose rate at every depth of the absorber was calculated from the microdosimeter and transmission chamber by:

$$D_{rel} = \frac{\bar{\epsilon} * m}{M_T} * C_{dead} \tag{8.1}$$

where $\bar{\epsilon}$ is the average energy deposited at that depth, m is the recorded events rate and M_T is the transmission chamber reading used for normalization. C_{dead} is a correction factor which necessary to correct for events that occur during the detector dead time after an event, and it is calculated by (Knoll, 2010, p. 120):

$$C_{dead} = \frac{n}{m} = \frac{1}{1 - m\tau} \tag{8.2}$$

where n is the true event rate and τ is the dead time after each event, which was measured to be 450 µs. The highest count rate recorded was 170 Hz and resulted in a correction of 1.083.

The beam energy prior to the BEW was approximately 15 MeV, but not accurately known. The initial beam energy and energy spread were determined by comparing the measured and simulated relative depth dose distribution from the microdosimeter, and the method of least squares was used to determine the best fit. The simulated beam energy was increased by steps of 0.01 MeV, and each energy step was simulated with a range of standard deviations separated by 0.02 MeV.

The thickness of all the materials in front of the microdosimeter was converted into Water Equivalent Thickness (WET) as follows:

$$WET_X = t_X * \frac{\rho_X}{\rho_W} \frac{\bar{S}_X}{\bar{S}_W}, \tag{8.3}$$

where ρ_X and ρ_W is the mass density of material X and water, respectively; $\bar{S}_X$ and $\bar{S}_W$ are the mean mass stopping power for material X and water, respectively; while t_X is the thickness of material X. The mean stopping power ratio used for each object was calculated from the range of proton energies that pass through that object. Thus, the proton energy range that pass through the BEW, scattering foil and transmission chamber is narrow, while it is a broad range of energies that pass through the absorbers and the air between the objects. The stopping powers were taken from PSTAR data (Berger et al., 2017).

8.2 Results

8.2.1 OCL Beam energy estimation

The simulated depth dose distribution that gave the best fit to the microdosimeter measurements is shown in Figure 8.3. The initial beam energy was 15.23 MeV with 0.04 MeV standard deviation just prior to the BEW. These beam properties were used for all simulation results shown here. The initial beam size had no visible effect on the energy spectrum at the absorber surface, and thus the beam was defined as a point source in all simulations. This is not surprising since the 52 μm thick tungsten BEW scatters the beam considerably, and there is a 1 mm collimator opening with a scattering foil 10 cm from the BEW.

The largest deviation between the experimental and simulated depth dose distribution is at the entrance at 1.98 mm WET. The experimental curve also falls slightly faster than the simulated just beyond the BP, but below 80% dose in the DDF the two curves match well.

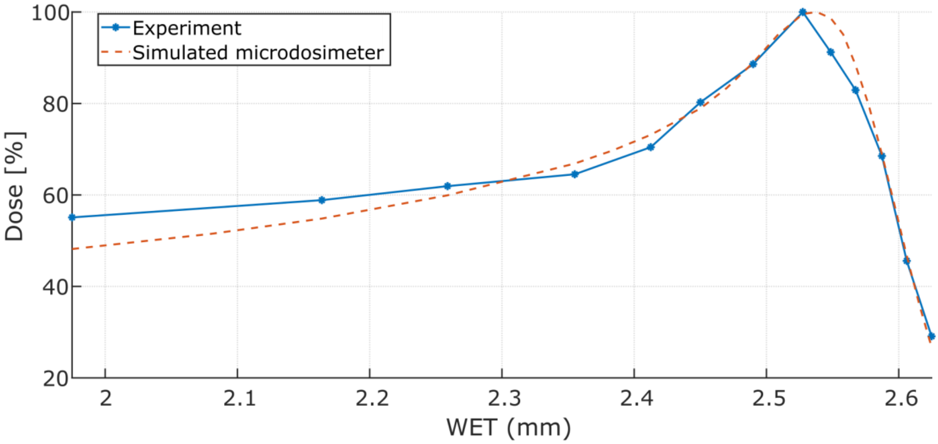

Figure 8.3: Experimental and simulated depth dose distribution. The simulation has a mean initial beam energy of 15.23 MeV with 0.04 MeV standard deviation and is the best fit to the experimental curve. The x-axis starts at 1.98 mm WET, as this includes WETs of all objects apart from the absorbers, such as the beam exit window, scattering foil, transmission chamber and 999 mm of air (Figure 8.1). The maximum relative uncertainty is calculated to be 1.8% through uncertainty propagation.

8.2.2 Energy deposition comparison with simulation

The RMS noise in the experiment was 1.8 keV, equivalent to 500 electrons, and the detection threshold was 11 keV. The measured and simulated energy deposition at four depths are shown in Figure 8.4. The mean energy deposition and spread increases with depth as expected and the distribution is Gaussian like and quite narrow at the entrance and just prior to the BP. However, at the BP and at larger depths the distribution becomes increasingly less Gaussian like. The measured peak at the entrance and just prior to the BP increases from approximately 100 keV to 180 keV, and reaches 240 keV at the BP before increasing further to a maximum of 330 keV at 50% of dose maximum in the DDF (50%DDF).

The measured and simulated spectra in Figure 8.4 show an overall good agreement, except for a very large number of low energy events and the band of low energy events to the left of the main peak. This was also seen in the alpha experiment in section 5.2.3.

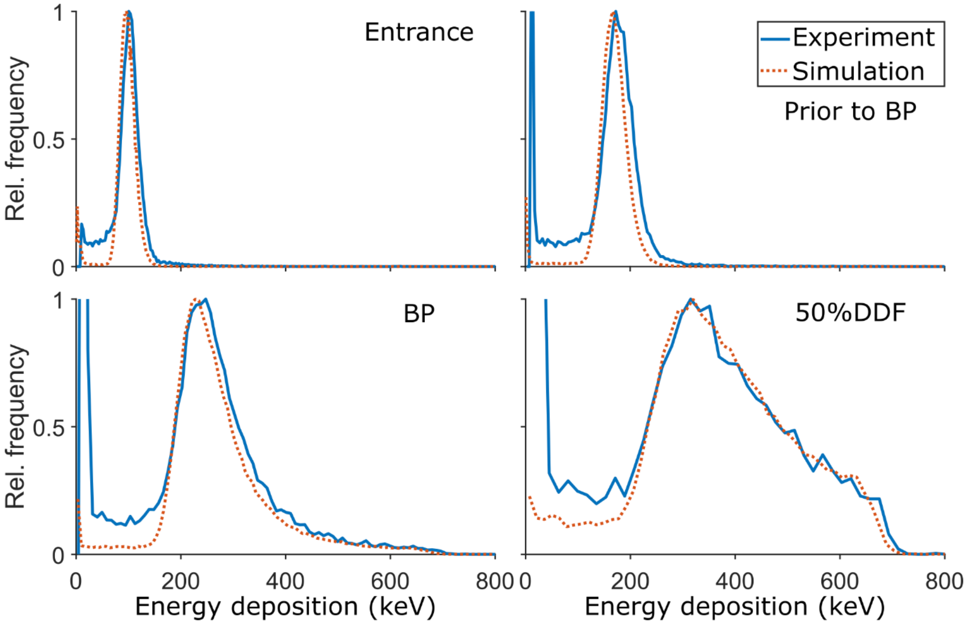

Figure 8.4: Measured and simulated energy deposition spectra at four depths. The depths are marked in Figure 8.5.

The two first plots in Figure 8.4 show that the peak and falling edge of the measured energy deposition is shifted slightly towards higher energies when compared to the simulation results. This is not seen at the BP and in the DDF, where there is a better overall agreement between measurements and simulations. This can be explained by a larger fraction of low energy protons in the experiment than in the simulations. These would give larger energy deposition at the entrance, but would stop before the BP. This is also in line with the depth dose distribution in Figure 8.3, where the measured dose is higher than the simulation.

The measured and simulated mean energy deposition at all depths are shown in Figure 8.5, where a 25 keV threshold was applied to both the measurements and simulations to remove the large fraction of low energy events. The overall shape of the two distributions are similar where the mean energy deposition at the entrance is approximately 100 keV, and the experiment is 2.8% higher than the simulation.

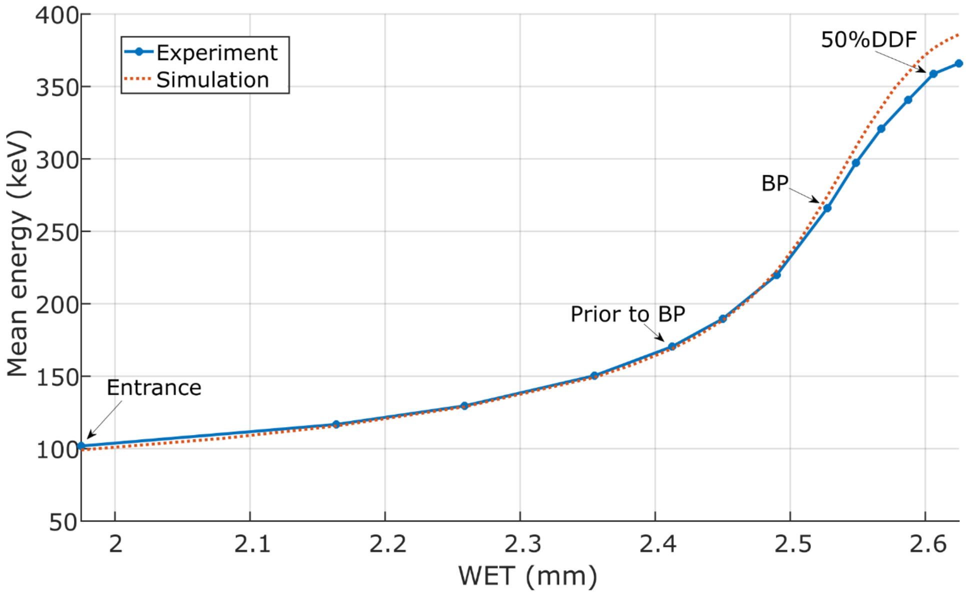

Figure 8.5: Measured and simulated mean energy deposition at all depths. The mean energy deposition is shown without error bars due to little statistical uncertainties as the largest relative standard error of the mean was 0.6%.

The relative difference between the two increases with depth beyond 2.5 mm WET, and the maximum is 366 keV for the experiment and 386 keV for the simulation, a 5.2% relative difference.

Since the low energy band to the left of the peaks shown in Figure 8.4 is assumed to be mainly due to detector characteristics, the mean energy deposition at all depths was replotted with a threshold that removed the tail in both the experiment and simulation. The result is shown in Figure 8.6, and the maximum mean energy deposition is now increased to 415 keV, with only 0.7% difference between the measurement and the simulation. However, the difference at the entrance is increased to 8.0%, which is the same as the difference in peak position seen in Figure 8.4.

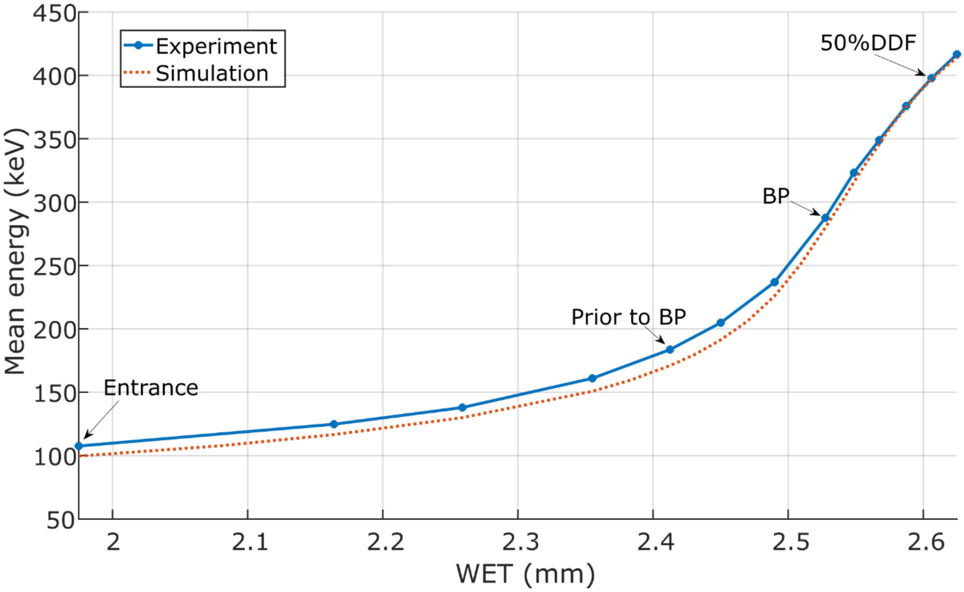

Figure 8.6: Measured and simulated mean energy deposition at all depths with a threshold that removed the low energy band seen in Figure 8.4. The threshold increases with depth such that this band is removed at all depths.

8.2.3 Tissue conversion functions, simulation comparison

The lineal energy from the simulated microdosimeter was tissue corrected with the three functions from chapter 7, and three tissue composed microdosimeters with SV heights of 12.0, 12.5 and 13.0 µm were simulated for comparison. The dose-mean lineal energy, $\overline{y_D}$ for the corrected and tissue composed microdosimeter at all simulated depths is shown in Figure 8.7.

The results from the three tissue composed microdosimeters are shown with dashed lines in Figure 8.7 and are nearly indistinguishable at the entrance with less than 0.5% difference, but the relative difference increased to ~2.6% in the DDF between the 12.0 and 13.0 µm tissue SVs. The three tissue conversion functions are also nearly identical in the entrance region, but the difference between the 12.0 and 13.0 µm function is ~5% in the DDF. It is also clearly seen that the 12.5 µm tissue correction and 12.5 µm tissue compose SV are the best fit. This correction function gives 1.1% higher $\overline{y_D}$ at the entrance compared to the 12.5 µm tissue SVs and the difference is below 0.5% in the DDF.

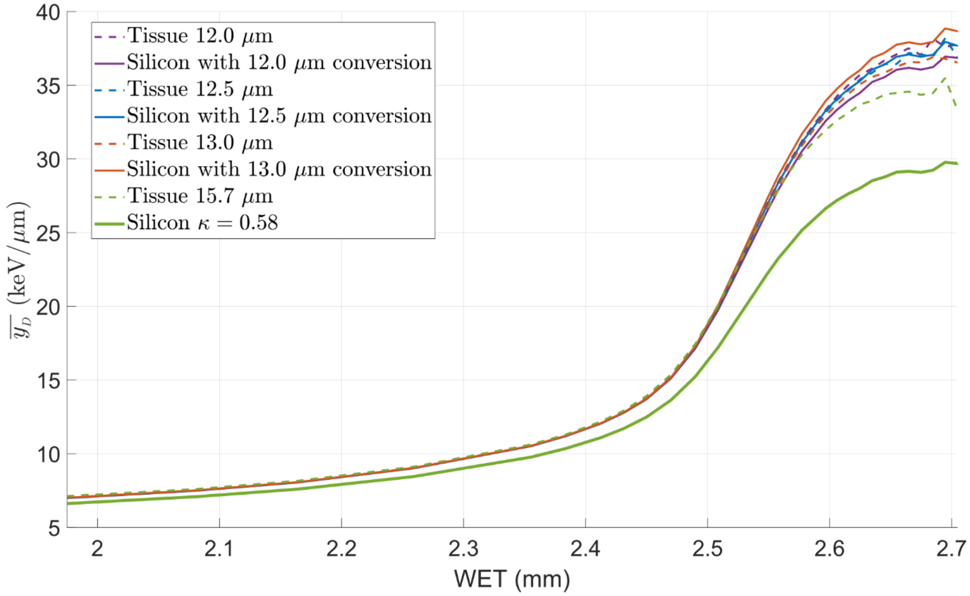

Figure 8.7: Simulation results of the silicon microdosimeter converted to tissue by the three conversion functions and a constant factor of 0.58. Simulation results from issue composed microdosimeters are also shown with SV heights of 12.0, 12.5, 13.0 and 15.7 µm for comparison with the conversion functions.

The constant conversion factor of 0.58, which is equivalent to a 9.1 µm/0.58 = 15.7 µm high tissue SV, has been used in several other studies with similar and identical microdosimeters, as mentioned in chapter 7. Figure 8.7 shows that the 0.58 correction factor gives a -7.2% and -15% deviation from the 15.7 µm tissue SVs at the entrance and in the DDF, respectively.

All the tissue corrected results shown hereafter uses the 12.5 µm tissue correction function, and when compared to a simulated tissue composed microdosimeter the SVs have a height of 12.5 µm.

8.2.4 Depth dose distribution from IC and microdosimeter

The measured and simulated relative depth dose distributions from the microdosimeter and IC are shown in Figure 8.8 a. The measured depth dose distribution with microdosimeter deviated most from the simulation at the entrance, while for the IC the deviation is mostly seen in the DDF.

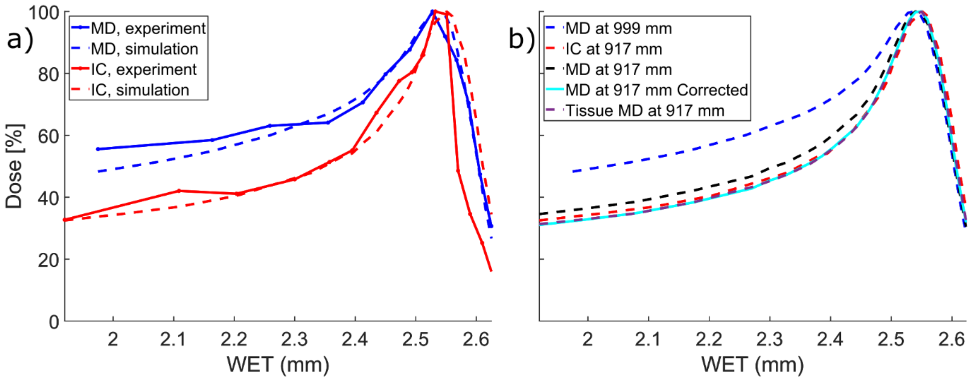

Figure 8.8: a) Measured and simulated depth dose distribution for the microdosimeter (MD) and IC. b) Simulated depth dose distribution for the microdosimeter and IC. The microdosimeter was simulated at its experimental position (999 mm from the BEW) and at the IC position (917 mm from the BEW). Results where the microdosimeter was tissue corrected is also shown, and results from a tissue composed microdosimeter at 917 mm is shown.

The microdosimeter has much higher relative dose at the entrance than the IC in both the simulation and measurement. This is most likely due to the position difference. The IC was positioned 27 mm from the absorber films, while the microdosimeter was 109 mm from them. Due to scattering in the absorber, the microdosimeter received a lower intensity and thus lower dose than the IC. This effect increased as the absorber got thicker, and thus the intensity at the microdosimeter dropped faster than at the IC.

For better comparison between the IC and microdosimeter, they were both simulated at the IC position (917 mm from BEW), shown in Figure 8.8 b. The microdosimeter still had a slightly higher relative dose at the entrance, 6.3% higher than the IC. This is expected, because the stopping power increases more rapidly for air (IC) than for silicon in this energy range (Berger et al., 2017), causing a larger dose difference between the BP and entrance for the IC. The depth dose distribution from the silicon microdosimeter was recalculated with the tissue correction function which is also shown in Figure 8.8 b along with the depth dose distribution from a tissue composed microdosimeter. The results show that the tissue corrected depth dose distribution matches the tissue composed microdosimeter very well. It also shows that the tissue corrected relative dose at the entrance was 4.2% lower than that of the IC, which is because the stopping power increases slightly faster for tissue than for air, as the proton energy falls.

8.2.5 Lineal energy

The microdosimetric spectra at four depths from the experiment and simulation is shown in Figure 8.9. A 25 keV threshold was added to both experiment and simulation to remove the large amount of low energy events, but not the low energy band to the left of the peak (Figure 8.4). The experimental results have been tissue corrected with the function $\kappa(\epsilon_{\mathrm{Si}})$, and the simulation is from a tissue composed microdosimeter. The positions of the spectra are the same as those in Figure 8.5 (energy deposition) and are marked in Figure 8.10, which shows the $\overline{y_D}$ at all depths of the experiment.

The shape of the spectra is generally similar to the energy deposition spectra in Figure 8.5, Gaussian like prior to the BP, and progressively less Gaussian at the BP and in the DDF. Like the energy deposition, the measured microdosimetric spectra at the entrance and prior to the BP are shifted towards higher energies when compared to the simulation. The measured spectra are also wider than the simulated at the entrance.

At the BP and 50%DDF the measured and simulated spectra match very well, but the simulated spectra fall off slightly before the measured, just like the energy deposition spectra in Figure 8.5. The low energy band seen in the energy deposition spectra has been supressed by the dose weighting in all the microdosimetric spectra.

The width of the spectra increases with depth, and the majority of events (full width at 5% of maximum yd(y)) were between 4.1 and 10.5 keV/µm at the entrance and between 7.6 to 21 keV/µm prior to the BP. However, events up to 65 keV/µm were measured at both positions. The majority of events at the BP were between 9.5 and 60 keV/µm, while they were between 12 and 61 keV/µm at 50%DDF.

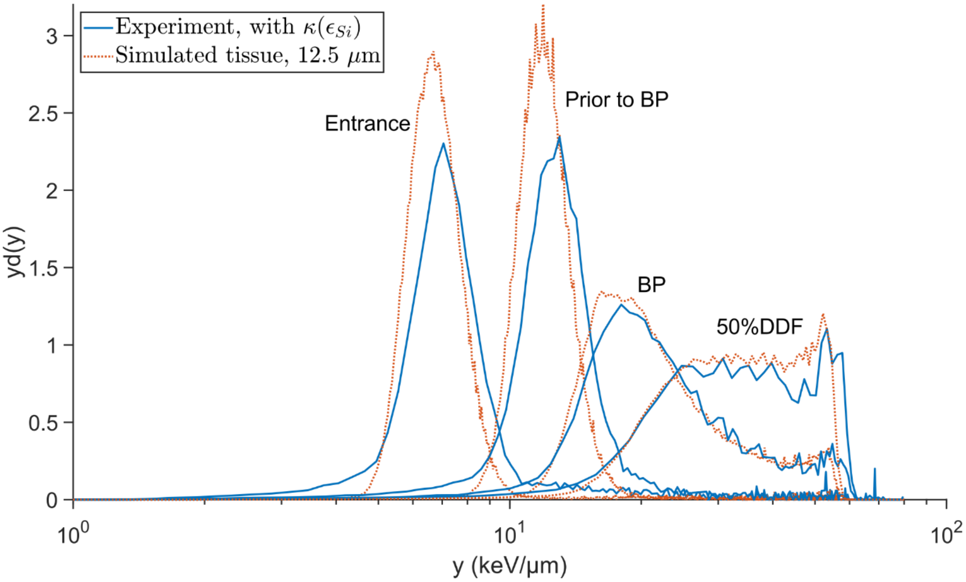

Figure 8.9: Microdosimetric spectra from tissue corrected measurements and simulations of a tissue composed microdosimeter at four depths. A 25 keV threshold was applied to remove the large fraction of low energy events.

$\overline{y_D}$ at all depths is shown in Figure 8.10 from the experiment and simulation. The measured $\overline{y_D}$ at the entrance was 8.0 keV/µm, approximately 13 keV/µm just prior to the BP, and reached 24 keV/µm at the BP before rising to the highest measured $\overline{y_D}$ of 35 keV/µm in the DDF. The measured $\overline{y_D}$ was 12% higher than the simulated at the entrance, but the difference was reduced to 2% at the BP and to 1% at the maximum in the DDF.

This is similar to the mean energy deposition at all depths when a threshold was added to remove the low energy band shown in Figure 8.6. However, the relative difference between the measured and simulated $\overline{y_D}$ at the entrance is larger than the mean energy deposition at the entrance due to the weighting of the higher energy events in $\overline{y_D}$.

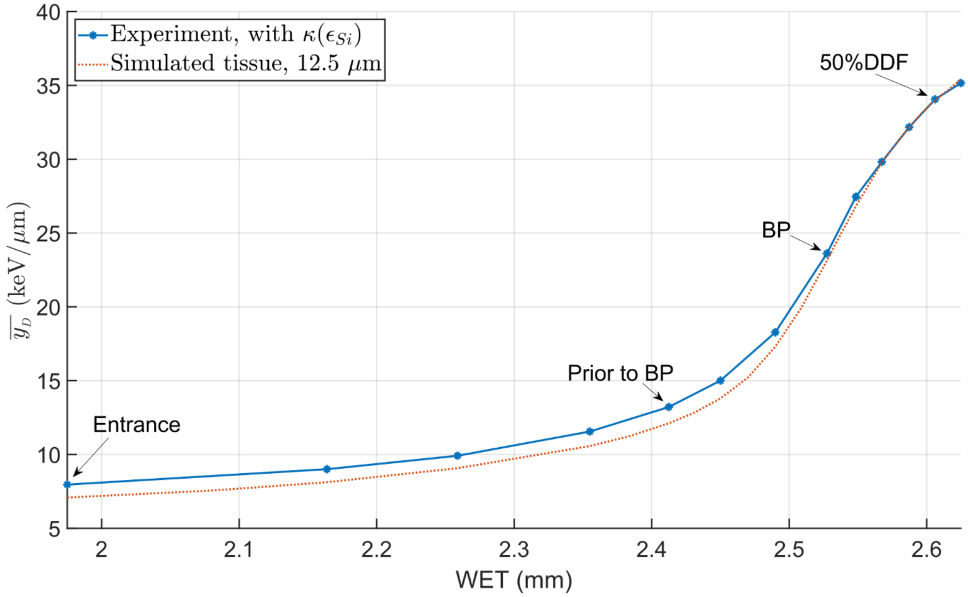

Figure 8.10: $\overline{y_D}$ at all depths from the tissue corrected measurements and simulations of a tissue composed microdosimeter.

All the 13 measured and corrected microdosimetric spectra are shown in Figure 8.11, where the binning increases with depth as the count rate decreases and the spectrum width generally increases with depth. The last six spectra are separated by single polyamide films with a WET of approximately 19 µm each, and the rising edges are clearly distinguishable between the spectra. For the last six spectra, which covers the BP and DDF, the falling edges were approximately equal at 60 keV/µm, corresponding to the proton energy of exact stoppers in silicon.

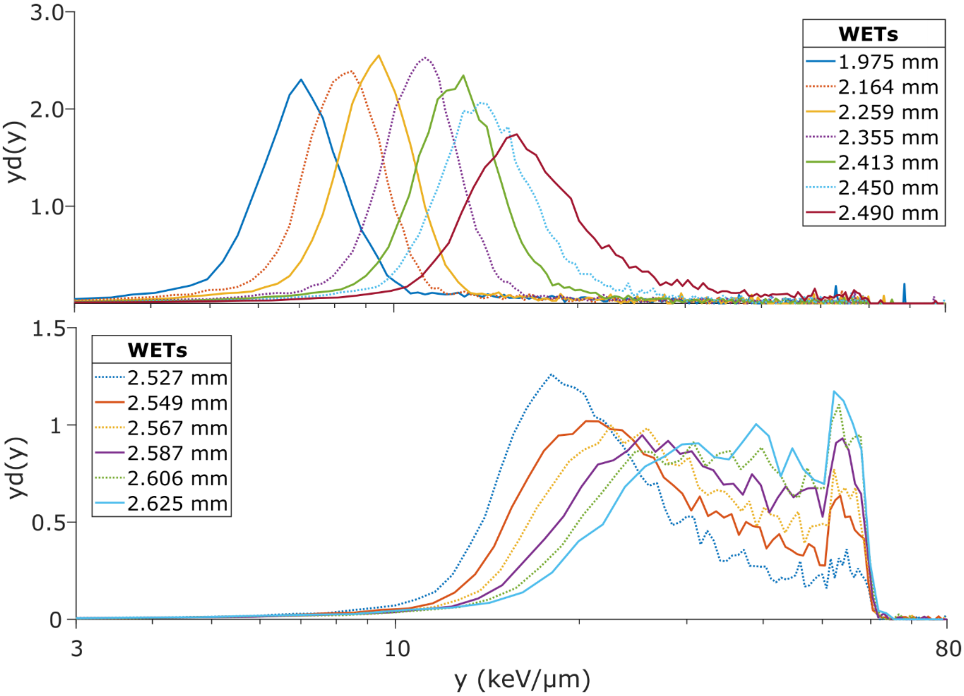

Figure 8.11: Measured tissue corrected microdosimetric spectra at all 13 measured depths. The legend gives the depth in water equivalent thickness (WET).

8.2.6 Significance of SV size

Simulations of the muscle composed microdosimeter were also conducted with 1 µm high SVs and compared to the 12.5 µm high simulations to investigate effects SVs' size. Figure 8.12 shows the microdosimetric spectra at four depth and Figure 8.13 shows $\overline{y_D}$ at all simulated depths. The spectra from the 1 µm high SVs generally have much wider distributions than the 12.5 µm SVs. The 1 µm high SVs also achieve much higher lineal energies as the falling edge of the distributions are slightly above 100 keV/µm, while it is between 50 and 60 keV for the 12.5 µm high SVs. $\overline{y_D}$ is similar for the two prior to the BP, although it is slightly larger for the 1 µm SVs at the entrance. In the DDF the difference between the two sizes increases with depth and the 1 µm high SVs has a maximum $\overline{y_D}$ of 57 keV/µm while it is 37 keV/µm for the 12.5 µm SVs.

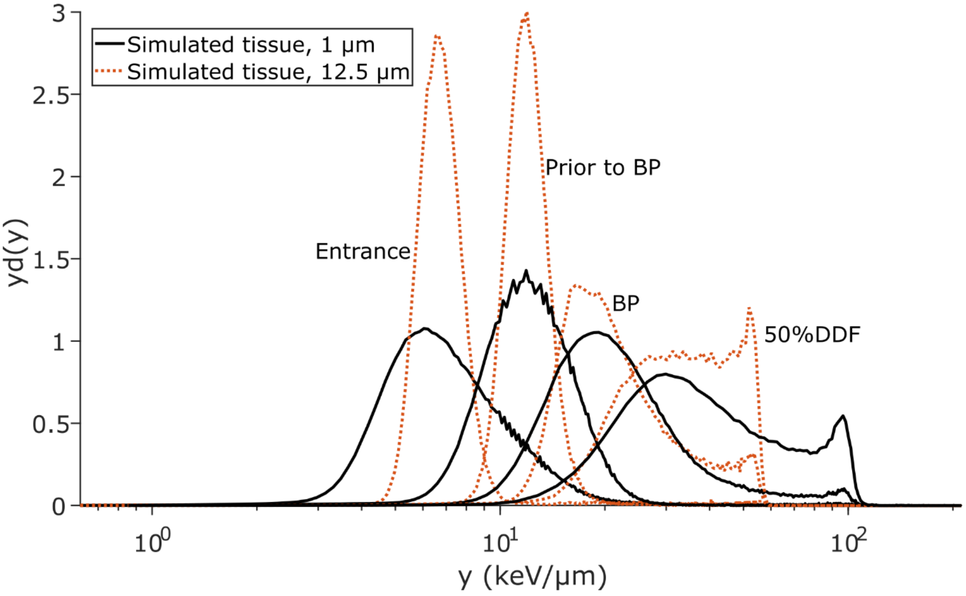

Figure 8.12: Microdosimetric spectra from simulated 1 and 12.5 μm high tissue composed SVs at four depths.

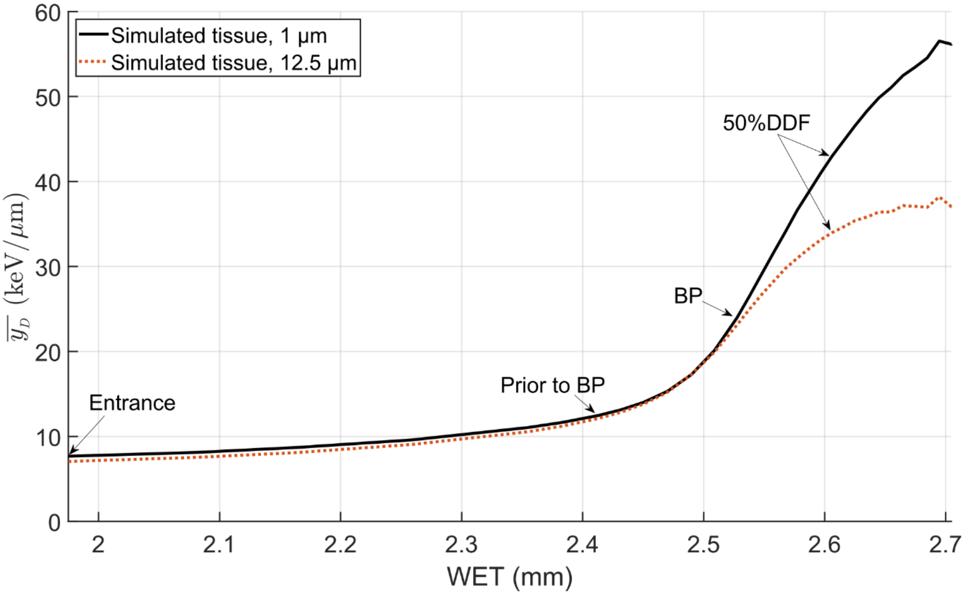

Figure 8.13: $\overline{y_D}$ at all depth from simulated 1 and 12.5 μm high tissue composed SVs.

8.3 Discussion

The large standard microdosimeter was used to measure energy depositions at 13 depths of a polyamide absorber from a ~15 MeV proton beam. The read-out electronics had a relative long dead time (450 μs) and the experiment had a stringent criterion that no more than 10% of the events should occur during detector dead time. If the relative dose were not important this criterion could be disregarded, and the intensity could be increased. A collimator and scattering foil were used to reduce the beam intensity enough to avoid pile-up and a large fraction of events during detector dead time. By using a faster shaping time and a microdosimeter with fewer SVs, much higher intensities would be tolerated.

The measurements were compared to simulations and dose measurements from an IC. The measured energy deposition and dose were higher at the entrance in the experiment than in the simulation. This could imply that there was a larger fraction of low energy protons in the experiment compared to the simulation which would deposit more energy at the entrance, but would stop before the BP. The results showed that the energy deposition and dose changed quickly with depth, such that lower energy protons might be a result of unforeseen and inhomogeneous materials in the path of the beam. This could come from a slight unevenness or a burred edge in the hole of the collimator or in the steel faraday cage around the microdosimeter. Such material unevenness is generally not noticed in beams with higher energy and larger energy spreads. A more accurate proton energy spectrum could have been acquired by measuring the total beam energy at the position of the microdosimeter with a 500 μm thick PIN diode that stopped the protons. At the BP and DDF the measured and simulated energy deposition spectra and dose depth agreed well.

Simulation results from the tissue correction functions, $\kappa(\epsilon_{Si})$, were compared to their equivalently sized tissue composed microdosimeters and showed that the 12.5 μm correction function gave a very good fit at all depths. The correction factor of 0.58 was also compared to its equivalently sized tissue microdosimeter and showed large errors. Any constant factors would produce errors at either the entrance, DDF or both, and are thus not suitable for low energy beamlines. The simulation comparison of the microdosimeter and IC showed that the relative depth dose distribution for the tissue corrected microdosimeter matched the IC very well, while larger deviations were seen without the correction function. The tissue correction function should also be tested and compared to the constant factor for higher proton energies at all depths, which is more relevant for proton therapy.

The microdosimetric spectra in Figure 8.9 showed how the dose weighting effectively supressed the low energy deposition tail seen in Figure 8.4. This shows that the dose weighting reduces the error from the areas of the microdosimeter with lower sensitivity. However, the dose weighting also increased the differences between the measurements and simulation results at the entrance. By removing the low energy tail, the difference between the measured and simulated mean energy deposition at the entrance was 8.0% (Figure 8.6), while the difference in $\overline{y_D}$ was 12% without removal of the low energy tail (Figure 8.9). At the BP and in the DDF the microdosimetric spectra from the measurements and simulations matched well.

The measured $\overline{y_D}$ ranged from 8 to 35 keV/µm, which is higher than what is achievable in a medical beamline with similarly sized SVs due to range straggling. In comparison, a similar microdosimeter was used in a 131 MeV medical proton pencil beam and measured tissue corrected $\overline{y_D}$ between 2 to 10 keV/µm in a water phantom (Linh T. Tran et al., 2017). This shows that the low energy beamlines can be used to compare the RBE as a function of $\overline{y_D}$ for different particle species since low energy protons can produce lineal energies similar to higher energies of heavier ions such as helium and carbon. However, the simulation results with 1 µm high tissue composed SVs showed that much higher lineal energies are obtainable with smaller SVs. Dahle et al. (2017) simulated LET to water in the same beamline and found a maximum LET_D of 50 keV/µm, which is similar to the maximum $\overline{y_D}$ to tissue of 56 keV/µm found with the 1 µm high SVs. Again, this raises the question of what SV size is the most biological relevant.

At the BP and DDF the measured microdosimetric spectra are clearly distinguishable from each other when only separated by 19 µm WET, demonstrating the excellent spatial resolution obtainable with these microdosimeters. At the BP, $\overline{y_D}$ changes rapidly with approximately 0.15 keV/µm per µm of water. This shows how sensitive such experiments and simulations are to uncertainties in absorber thicknesses, initial beam parameters and other uncertainties in the experimental setup. This can give rise to large systemic uncertainties in both $\overline{y_D}$ and LET and shows the necessity for accurate measuring tools. The large variability in the published proton RBE data, as discussed by Paganetti (2014), might be reduced with relatively inexpensive and accurate measuring tools as presented here.

8.4 Summary

A large standard microdosimeter was used to measure the energy depositions of a 15 MeV proton beam at several depths of a polyamide absorber by stacking thin films of polyamide in front of the microdosimeter. The results were compared to MC simulations and the relative depth dose distribution from a commercial IC. The simulation setup was used to test the tissue correction functions, and the measured microdosimetric spectra were used as microdosimetric characterization of the beamline which is used for radiobiological experiments.

The measured energy depositions, microdosimetric spectra and depth dose profile agreed very well with simulations and the IC measurements at the BP and in the DDF. The energy deposition and depth dose distribution showed slightly higher values at the entrance. This could be explained by a higher fraction of low energy protons than were simulated.

The tissue correction function which is equivalent to a 12.5 µm high tissue SV where found to be the most accurate of the three correction functions with a maximum error of 1.1%. The tissue correction function also improved the relative depth dose distribution with respect to the measurements from an IC.

The measured lineal spectra generally became wider with depth and the measured tissue corrected $\overline{y_D}$ ranged from 8 keV at the entrance to 35 keV in the DDF. The experiment demonstrated the excellent spatial resolution in the depth direction as spectra separated by only 19 μm WET are clearly distinguishable.

The simulations also show that the microdosimetric spectra change significantly when the tissue equivalent thickness is reduced from 12.5 to 1 μm.

The microdosimeter is a cheap and easy to use tool to measure microdosimetric spectra for radiobiological experiments with excellent spatial resolution. It can also be used to benchmark simulations of experiments such that the lineal energy to SVs with different shapes and sizes can be found.

9. Tracking “sandwich” microdosimeter

A new form of experimental microdosimetry is proposed here, where a stack of high granularity Monolithic Active Pixel Sensors (MAPS) such as the ALPIDE is used to track all particles entering and generated within the detector. A tracking “sandwich” microdosimeter. This demands a new form of microdosimetry unlike regional microdosimetry where the energy deposition from single events are measured in a well-defined micrometric volume. In regional microdosimetry, the kind of particle(s) that deposit the energy and their track structure is not regarded. By stacking several high granularity pixel detectors close together, it is possible to track all particles entering and generated within the detector. Figure 9.1 shows a GATE simulation of the track from a C-12 ion with 200 MeV/u energy passing through 3 detector layers (active layers) with dimensions like the ALPIDE.

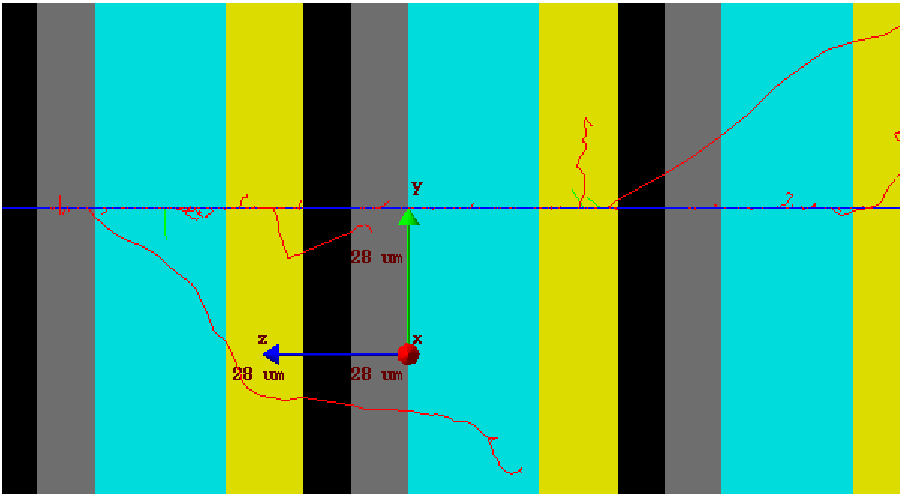

Figure 9.1: Simulated track from a 200 MeV/u C-12 ion through three active layers with dimensions similar to the ALPIDE. The tracks are from the C-12 ion (blue), electrons (red) and photons (green). The active layers consist of circuitry (grey), epitaxial silicon (cyan) and bulk silicon (yellow), with 9 µm of air between the layers (black). The ALPIDE pixel pitch is illustrated by the 28 µm long axes.

Each of the active layers has the possibility to coarsely measure the energy deposition, giving a rough dE/dx measurement for every active layer. The track length, range, track structure and dE/dx in every active layer can then be used to identify all the primary and secondary particles as well as their energy at every position along its track. Such a tracking “sandwich” microdosimeter can give a detailed image of a radiation field with information about every particle present. By performing such measurements of the radiation field in conjunction with radiobiological experiments, more advanced and accurate models might be created of radiation induced biological effects where more parameters than dose and radiation quality (LET or microdosimetry) are taken into consideration.

It might also be possible to extract microdosimetric spectra by seeing how the tracks intersect virtual sites when both particle ID and energy is known. It would then be possible to see how the spectra change with site geometry for a given radiation field as it would be easy to change the geometry of a virtual site. The tracking volume can also be voxelated and the LET and dose can be calculated for each voxel from the tracks, as is commonly done in medical MC simulations. The detector can then be used to benchmark MC simulations and thereby lower the systematic uncertainties.

This chapter discusses specifications for such a sandwich tracking microdosimeter and the possibility of using the ALPIDE detector for such a purpose. However, the MAPS technology is still quite young, and it is expected that future MAPS will have much more favourable specifications than the ALPIDE.

9.1 Energy resolution

When energy is deposited in the sensitive epitaxial layer of the ALPIDE, the free electrons drift towards the collection nodes and triggers a hit. Each of these nodes has an address, and by looking up which nodes are hit, it is possible to create a map of where the energy has been deposited. As these nodes sit in a common sensitive epitaxial layer (Figure 3.11), it is possible to trigger several of them from a single event as some charge will drift towards one node while some drift towards another.

This can happen when a small amount of energy is deposited near the middle of two to four nodes and the charge is distributed among the neighbouring nodes and triggers all of them. It can also occur when a large amount of energy is deposited and a dense cloud of liberated charge drifts far away from where the energy was deposited. The electric field from the collection node normally collects all the charge near it, but as the node's field is relatively weak without bias voltage, it may be distorted from a dense charge cloud's electric field due to plasma effects (Seibt, Sundström, & Tove, 1973). The liberated charge can thus trigger several nodes in both directions as the charge drifts by them. Whenever more than one neighbouring node or pixel is triggered from a single event, it is called a cluster, and the number of pixels triggered by a single event is called the cluster size.

Figure 9.2 shows how the deposited energy and LET in the sensitive layer of the ALPIDE is correlated with the resulting cluster size without detector bias voltage. The energy deposition is found through GATE simulations, and the LET is the mean deposited energy divided by the sensitive epitaxial layer thickness of 20 µm. The uncertainty in the plot is the standard deviation in the cluster size distribution of each experiment. The cluster sizes clearly increase with increasing energy deposition, but the correlation is not proportional, and the cluster size seems to have an asymptotic limit of ~30. Given the large spread in the cluster sizes for each experiment and the asymptotic limit, it does not seem possible to reliably measure LET values above 50 keV/µm.

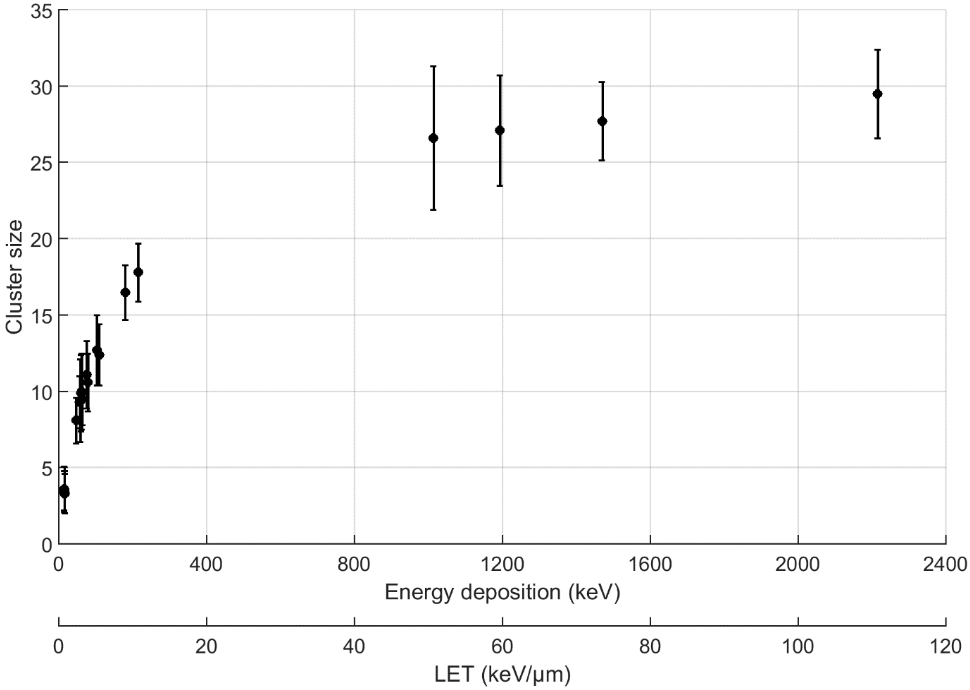

Figure 9.2: The cluster size from single events in the ALPIDE as a function of deposited energy and LET across several experiments. Data is taken from Tambave et al. (2019) with additional data from more recent C-12 ion experiments taken under the same conditions. The energy deposition is found through GATE simulations, and the LET is the average deposited energy divided by the thickness of the SV.

The ALPIDE chip was investigated using the IBICC technique at ANSTO with a 10 MeV ^{4}He microbeam that has a range of 70 µm in silicon (Berger et al., 2017). The result was used to create a map that shows the average cluster size produced at every position of the beam (Figure 9.3). The map and distribution in Figure 9.3 clearly show that a monoenergetic beam creates a very wide distribution of cluster sizes and that the cluster size depends on the position of the energy deposition. This position sensitivity is also seen in Figure 9.4 where the cluster size is plotted as a function of event number (time). Since the microbeam scanned the surface of ALPIDE, column by column, from left to right, the oscillation shows how the cluster sizes depends on the position of the beam along the x-axis. The scanned area was 128 x 128 µm^2, equivalent of 4.5 pixels in both directions. The oscillations seen in both the map in Figure 9.3 and plot in Figure 9.4 also show a period of ~4.5. However, from the map in Figure 9.3, the oscillation is just seen along the x-direction and not along the y-direction.

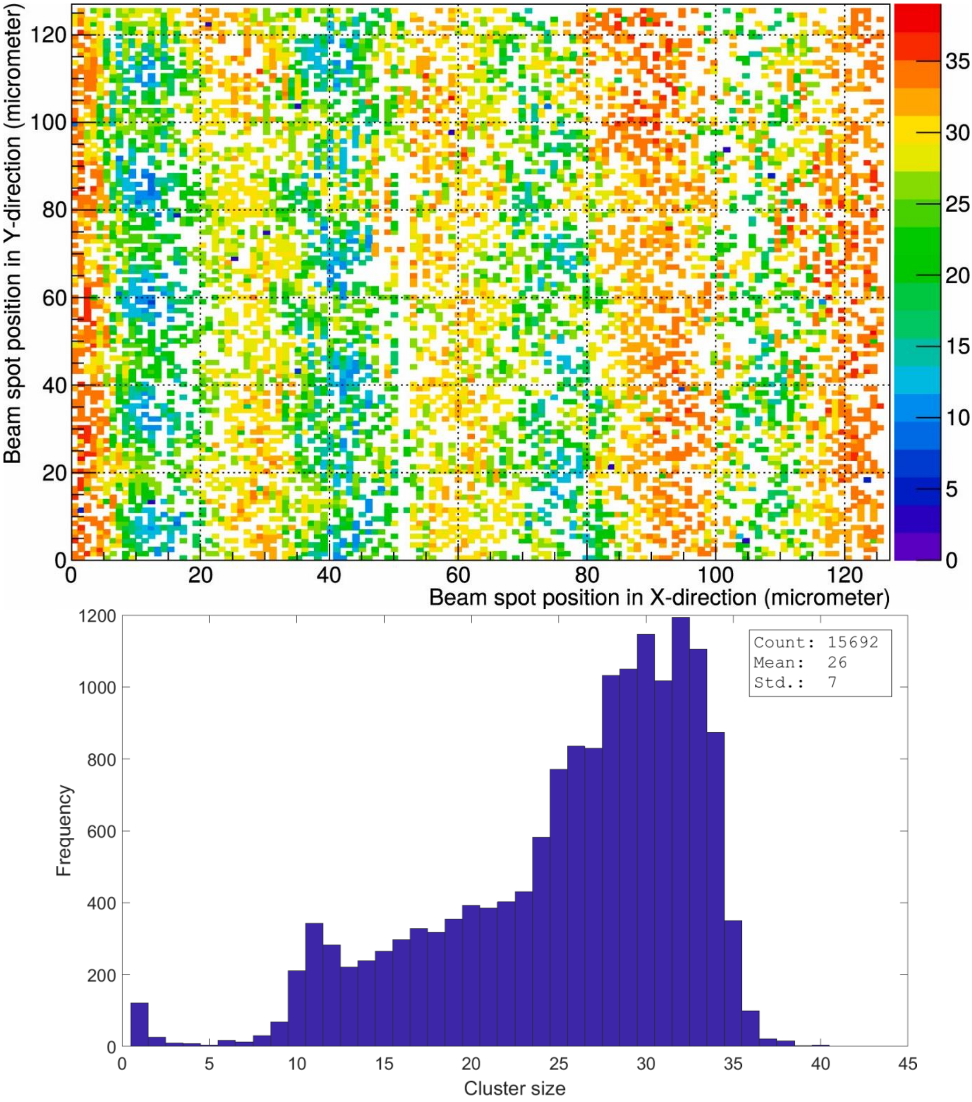

Figure 9.3: Cluster size map (top) and distribution (bottom) of a microbeam scan of the ALPIDE. Each coloured pixel in the map represents the position of the beam and the colour represents the average cluster size at that point. Taken from Tambave et al. (2019) and Huiberts (2018) with permission.

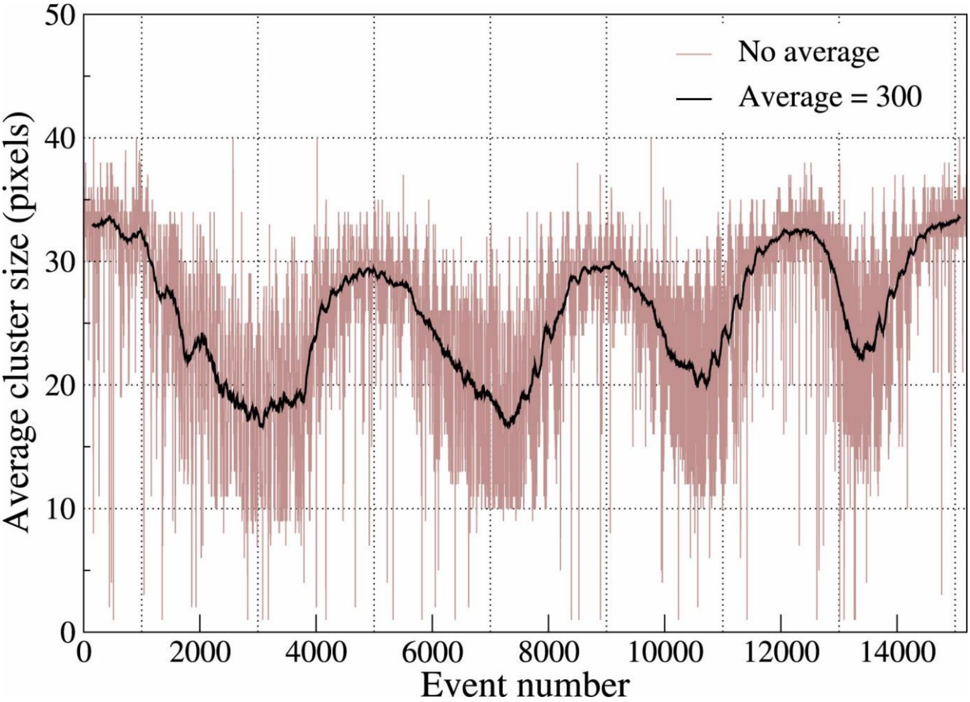

Figure 9.4: Plot of the cluster size as the time (event number) progresses. A running average filter is added on top of the data. The microbeam was scanning column by column from left to right such that the event number is increasing with increasing X-position in Figure 9.3. The plot is taken from Tambave et al. (2019) with permission.

The position sensitivity should be possible to limit or remove completely as the ALPIDE outputs both cluster size and position of the hit pixels. Thus, it might be possible to consider this cluster size oscillation along the rows when calculating the deposited energy from cluster size. Another way to correct for the wide cluster distribution is to average the cluster size over several active layers, like a running average filter. This should work well for high velocity particles where the LET changes slowly but will give higher error towards the end of their tracks. If the active layers are stacked close enough together, and the averaging is performed only from the previous, present, and next layer, this might yield usable results at the BP as well.

9.2 Spatial Resolution

To effectively track a particle, it must either cross several active layers when it has a direction perpendicular to the active layers or cross several pixels in a single active layer if going along the active layer plane. Furthermore, the track reconstruction will generally be easier if scattering is kept to a minimum. Thus, high momentum particles will be the easiest to track precisely, as they will scatter little and cross many active layers and pixels. In a beamline, the highest momentum particles are generally the primary particles, and a tracking sandwich microdosimeter must as a minimum be able to reconstruct the tracks with good enough resolution to determine how many of the primary particle tracks intersects biologically relevant sites.

The ALPIDE has a pixel pitch of ~28 x 28 μm^2 and a position resolution of 5 µm in both directions of the ALPIDE plane (Aglieri Rinella, 2017; Šuljić, 2016). The thickness of the ALPIDE is approximately 50 µm, where ~13 µm is bulk material that might be possible to reduce. Some of the bulk is necessary to allow for detector biasing, and thus a minimum thickness of approximately 40 µm is plausible for the current ALPIDE. The minimum pixel pitch is thus 28 x 28 x 40 μm^3 for a tight stack of thinned down ALPIDE detectors. The position resolution in the z-direction is calculated as the standard deviation of a uniform distribution:

$$\sigma_Z = \frac{40\ \mu\text{m}}{\sqrt{12}} = 11.5\ \mu\text{m}. \tag{9.1}$$

The result from a tracking microdosimeter is used to reconstruct the tracks and the resolution gives a probability distribution of how far the actual track was from the reconstructed track. In a tightly stacked ALPIDE, the position resolution is approximately 5 x 5 x 12 μm^3 which is comparable to the 3D SOI microdosimeter SV. However, an ALPIDE based tracking microdosimeter cannot distinctly count the number of tracks that cross a virtual 10 µm diameter spherical site. Since the position resolution is comparable to the site in question it can give a probable estimate of how many crossed the sphere, from which angle, the probable path length, particle type and probable energy of the particle. These estimates will have lower uncertainties for large sites, and larger uncertainties for small sites. This is contrary to traditional experimental regional microdosimetry, where the definitive number of events above an energy threshold in a site is known, and their energy deposition is known with little uncertainty. However, the particle type, particle energy, track structure and actual path length through the site is unknown in regional microdosimetry.

Secondary electrons

Electrons are the most produced secondary particles when a charged particle traverse matter and a large fraction of the energy is deposited by these electrons. A detailed MC code built to track every produced delta electron from protons in water with therapeutic energies was presented by Liamsuwan et al. (2011). The protons and electrons were followed down to 1 keV and 7.6 eV, respectively, and the simulations showed that more than 70% of the dose from 160 MeV protons was deposited by secondary electrons. It is therefore desirable to be able to track as many as possible of the secondary electrons in a tracking microdosimeter, as biological relevant sites might be intersected solely by electrons. The electron energy distribution generated by 300 MeV protons slowing down to 1 keV is shown in Figure 9.5.

Electrons that have a trajectory along the primary particle are not seen as it is impossible to distinguish between the primary and secondary track if a single pixel fire in every layer along its track. In principle, the secondary track must thus have a transverse path of at least one pixel pitch (~28 µm) with respect to the primary path to be detected. By allowing large cluster sizes through low or no bias voltage, the secondaries must have a transverse path longer than the cluster radius. Even with a strong bias applied, the primary particle will make a cluster size between one and four when it passes through the middle of several collection nodes. To distinguish a secondary particle from a cluster size between 1 and 4, at least 3 adjacent pixels have to fire, as seen in Appendix A. To know the direction of the secondary, at least 4 pixels must fire.

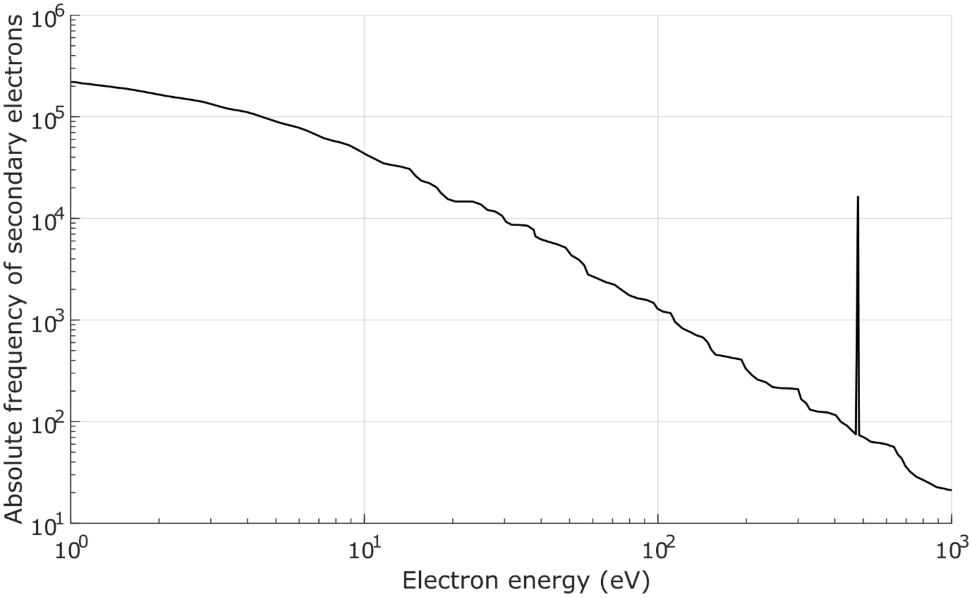

Figure 9.5: Simulated delta electrons distribution from 300 MeV protons slowing down to 1 keV in water. The peak at 514.46 eV is the emittance of auger electrons from the oxygen atoms and make up 0.7% of all emitted electrons. The figure is recreated from (Liamsuwan et al., 2011).

Table 9-1 lists LET and CSDA range for electrons with different relevant energies in silicon and tissue from the ESTAR database (Berger et al., 2017). To identify a secondary electron in the ALPIDE detector, it must travel at least 25 μm in the transverse direction, corresponding to approximately 50 keV in silicon, the building material of the ALPIDE. To know the direction of the electron it must travel at least 50 μm in the transverse direction, corresponding to 80 keV. Since electrons are light and scatter easily, their track is rarely straight. The minimum found energies here are truly minimum, as they assume straight lines in a perfectly transverse direction.

The maximum amount of energy transferred to an atomic electron (T_e) from a traversing ion with energy, E, and atomic nucleon number, A, is found through momentum conservation:

$$T_e = \frac{4}{1823} * \frac{E}{A} * \cos^2 \theta \,, \tag{9.2}$$

Table 9-1: LET and CSDA range of electrons in silicon and tissue with energy from 10 to 70 keV. Unrestricted LET is used, same as dE/dx. Data is from ESTAR (Berger et al., 2017).

	Silicon		Tissue	
Energy (keV)	LET (keV/µm)	CSDA range (µm)	LET (keV/µm)	CSDA range (µm)
10	3.9	1.5	2.2	2.5
20	2.4	4.9	1.3	8.6
30	1.7	9.9	1.0	17.7
40	1.4	16.3	0.8	29.5
50	1.2	24.0	0.7	43.6
60	1.1	32.9	0.6	60.0
70	1.0	42.8	0.5	78.4
80	0.9	53.7	0.5	98.7
90	0.8	65.5	0.4	120.7
100	0.8	78.2	0.4	144.4
200	0.5	242.4	0.3	453.0
300	0.4	452.6	0.2	850.2
400	0.4	689.6	0.2	1300.0

where θ is the scattering angle with respect to the ion's trajectory. Thus, the minimum primary ion energy necessary to produce a detectable secondary electron is about 25 MeV/u, while the minimum energy to determine the direction of the delta electron is about 40 MeV/u. However, there are two problems with these minimums. The majority of secondary electrons are emitted with θ near 90°, yielding low electron energies (Schmidt-Böcking et al., 1992), also seen in Figure 9.5. Secondly, to achieve maximum energy transferal, θ must be 0, meaning that the electron direction will initially be along the primary. It could still be detected, but to do so it must first scatter to a very high angle before losing to much energy. Furthermore, when an electron scatters on another electron to high angles, it also transfers a large fraction of its energy to the target electron. The electron can only maintain its energy and deflect when scattering of a nucleus. Thus, the primary must have significantly higher energy than 25 MeV/u to produce a significant amount of detectable delta electrons. This means that delta electrons will rarely be visible near the BP in charged particle therapy.

So far, the ability to detect secondary electrons has only been discussed with high bias voltage, yielding cluster sizes between one and four for even high LET particles.

If the bias voltage is decreased to gain a coarse energy measurement, then the delta electrons must have an even longer transverse path to become visible. The bias voltage is thus a double-edged sword, where the user must choose between energy measurement and the ability to track some of the delta electrons. A possible solution is to have every second active layer with and without bias. This could give good results if the active layers are positioned close together, and the LET of the beam does not change significantly between layers.

9.3 Tissue equivalence

Silicon is not tissue equivalent, and with both a higher Z number and a higher density, the radiation field in silicon will differ significantly compared to that in tissue. The energy loss is higher in silicon, giving shorter path lengths. The cross section for Coulomb scattering is also higher in silicon which affects the track structure, and the secondary particles from nuclear reactions will also differ. Thus, a tracking detector made solely by silicon, silicon-dioxide, and aluminium, which are the most common detector materials, will produce and track a radiation field different from that in tissue.

A solution to this is to insert a tissue equivalent (TE) material such as plastic between every active layer. By making the tissue equivalent layer thicker than the active detector layer, most of the produced secondaries, most of the energy loss and scattering will be in the TE material. However, by increasing the tissue equivalent layer the spatial resolution in the depth direction is worsened.

To achieve good TE with a silicon composed active layer, the ratio of TE layer thickness to that of silicon should be as high as possible. To allow for this while still maintaining good spatial resolution in the depth direction, the active silicon layer must be made as thin as possible. As discussed in section 9.2, the current ALPIDE cannot be thinned down much below 40 µm.

9.4 Alternative setup for measuring secondaries in tissue

An alternative MAPS sandwich microdosimeters that can be used to study the secondary particles from a beam in a TE material is shown in Figure 9.6. The beam is incident downwards in the drawing where the two top horizontal MAPS detectors is used to measure the position and angle of every primary particle incident on the stack of vertical MAPS. The vertical MAPS have a layer of TE material between them, and by selecting the primary tracks that are contained within the TE plastic the secondaries that are injected into the MAPS epitaxial layer can be studied.

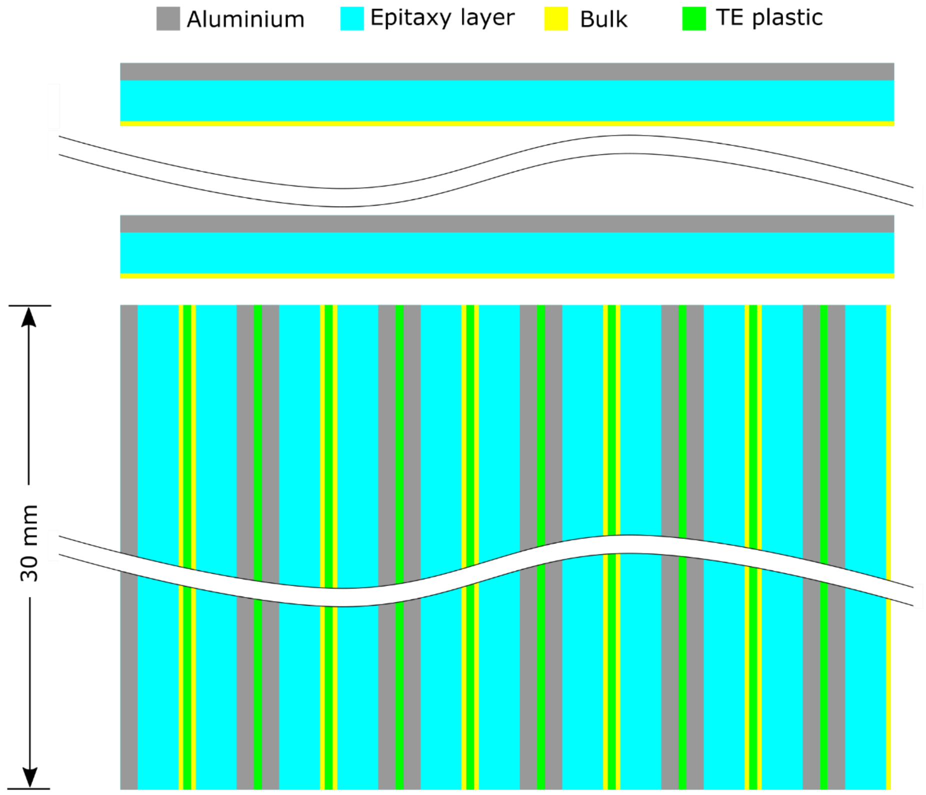

Figure 9.6: Detector setup with MAPS detector for measuring the secondary particles produced in a TE plastic from a beam. The beam is incident downwards in the drawing from the top. The setup can be used to study the secondary particles that are ejected from the TE plastics from primary track that are contained within the TE plastic. The first two horizontal MAPS is used for measuring position and angle of the incident particles. The dimensions used are that of the ALPIDE detector and they are scalable, but with its bulk thinned down to 3 µm. The TE layer shown is 5 µm thick.

The primary particles that pass along the epitaxial layer are easily seen since their high energy deposition creates clusters along their track, producing a “fat” track. Thus, the primary particles that are contained between two epitaxial layers is seen by the absence of a fat continuous cluster track. However, the primary particles that are contained between two epitaxial layers are visible by the randomly generate secondary particles that are injected into the epitaxial layer of the MAPS.

The aim of the setup is to track secondary particles from a TE material. Since the setup can only discriminate between the primary particles that are either inside or outside of the sensitive epitaxial layer, the volume between the epitaxial layers should mainly consist of a TE material. The ALPIDE detector has an aluminium layer on top which is part of the circuitry, and a silicon bulk layer at the bottom which is used for biasing and mechanical support. The aluminium layer cannot be thinned down without disrupting the function of the detector, but the silicon bulk can be thinned. Figure 9.6 shows a MAPS with a 3 µm thick bulk and 5 µm thick TE layer. Every other ALPIDE in the figure is flipped, such that the bulk from two adjacent ALPIDES face the same TE layer, and the aluminium layer from two adjacent ALPIDE detectors also faces the same TE layer. Since the aluminium layer is approximately 11 µm thick a large fraction of secondaries will come from this layer and not the TE material. Thus, only measured secondaries coming from the TE materials between two bulks can be used, and the bulk should be thinned as much as possible.

9.5 Development in MAPS technology

The development of new MAPS takes advantage of the rapid development of CMOS imaging sensors for mobile cameras for the consumer marked (Garcia-Sciveres & Wermes, 2018). This makes the MAPS affordable, and the technology is expected to develop quickly, making it possible to reduce the pixel pitch and have more advanced circuitry.

MAPS was proposed by S. Parker (1989) and the first prototype was developed in the early 1990s (Kenney et al., 1994). The first MAPS that were used for particle physics was the ULTIMA sensor developed for the STAR experiment at RHIC (Valin et al., 2012). The ULTIMA sensor was built using a 350 nm CMOS process and had a pixel pitch of 20.7 µm. The ALPIDE chip presented in chapter 3.4 is the most advanced MAPS to date with a 180 nm CMOS process, and will be used in the upgrade of the ALICE ITS in 2020. A new generation of MAPS is planned for the proposed NA60+ experiment at CERN, using a 65 nm CMOS process to create a sensor with a ~10 µm pixel pitch (Usai, 2019).

The MAPS are generally produced by altering mature CMOS imaging process. While the state of the art MAPS has a pixel pitch in the 20 to 30 µm range, the newest imaging sensor from Samsung Electronics has a pixel pitch of 0.7 µm ("S5KGH1 - ISOCELL Slim GH1," 2020). Thus, it is expected that the coming generations of MAPS will have a growing pixel density as well.

Compared to CMOS imaging sensors, MAPS created for particle physics demand a much higher read-out rate, better timing resolution and must be radiation tolerant (Garcia-Sciveres & Wermes, 2018). However, the stringent criteria of particle physics can likely be relaxed for a microdosimeter with MAPS, such that newer CMOS imaging technology might be used to create a thin MAPS specifically for microdosimetry with a low pixel pitch.

9.6 Summary and future work

In this chapter a tracking sandwich microdosimeter has been proposed and the feasibility of using a stack of ALPIDE detectors for such a microdosimeter has been discussed.

The ALPIDE can measure the energy deposition in each layer through cluster sizes, although the energy granularity is poor due to the distinct cluster sizes between 1 and ~30. The cluster size is not proportional to the energy deposition, such that a non-linear calibration function must be created. Furthermore, the cluster sizes are position sensitive, and further characterization work must be conducted if the position sensitivity is to be incorporated in the calibration function. The cluster sizes also seem to reach an asymptotic limit of about 30 for the current ALPIDE such that energy depositions from particles with LET above 50 keV/µm cannot be measured.

The spatial resolution is decided from pixel pitch (X- and Y-direction) and the distance between the active layers (Z-direction). The spatial resolution is likely good enough in the X- and Y-direction to see how many primary tracks cross different forms of geometries with thickness or diameter in the order of 10 µm. Most secondary electron tracks will not be possible to see as they need to separate more than one pixel pitch from the primary track in the transverse direction. The delta electrons emitted with high energies are few and are emitted along the primary track. Lowering the bias voltage to increase cluster sizes will make it even harder to see delta electrons as they need transverse tracks that extends beyond the cluster radius.

The easiest solution to increasing the TE of the detector is to insert TE materials between the active silicon composed layers. A high ratio of TE material thickness to active silicon layer thickness will ensure good TE properties but reduce the spatial resolution in the depth direction. The alternative setup to study secondaries from a TE material (Figure 9.6) ensures that most secondaries come from a TE material while maintaining a maximum position resolution. However, this setup can only utilize the measurements where the primary is kept within the TE material, which is a small fraction of the events.

The MAPS technology is still young, and the fast development in the imaging industry gives expectations of MAPS with sub-micron resolution in the future. If a MAPS optimized for a tracking microdosimeter were to be designed, it could relax some of the stringent requirements concerning read out rate, timing information and radiation hardness, and optimize pixel density and thickness.

The proposed sandwich microdosimeter increases complexity compared to the current experimental regional microdosimetry. A theoretical framework for such a tracking microdosimeter should be developed to specify the value such measurements can bring to radiobiology and the requirements of such a detector.

A detailed simulation model of a generic tracking sandwich microdosimeter should be built to define the necessary specifications. A generic model should be able to vary the:

- Pixel pitch
- Active layer thickness
- TE/plastic layer thickness
- TE/plastic layer composition
- Cluster size as function of energy deposition (biasing effects)

The simulated detector output should then be used to reconstruct the tracks, identify the particles, and the particles' energies at all positions for different beams. The reconstruction should then be compared to the actual simulated tracks to estimate the error and to optimize the design. The reconstructed tracks should also be compared to simulated tracks in pure tissue or water to find the optimal thickness ratio between TE and active layers.

10. Conclusions and outlook

This thesis has mainly been devoted to a new generation of 3D SOI microdosimeters. The microdosimeters have been tested in various conditions to investigate their characteristics, and a detailed MC model was created for comparison. A novel tissue correction function for protons has also been developed and applied when a microdosimeter was used for a microdosimetric characterization of a low energy proton beamline.

The microdosimeter measured a range of spectra from soft photon sources accurately, and the MC model also produced accurate results. The soft photon sources can be used as a low energy calibration and the results also demonstrated how the fraction of insider events decreased with increasing photon energy. This shows that the microdosimeters are not suitable for assessing the beam quality for soft x-rays as the microdosimetric spectra depend heavily on the SVs' size due to the large fraction of insider, beginner, and stopper events.

The soft photons also showed that the microdosimeters has 100% CCE. The alpha experiments also show approximately 100% CCE, but with slightly larger uncertainty due to the uncertainty in the height of the cylindrical SVs. The CCE for the L_{Poly} and S_{Poly} could not be estimated with the alpha sources due to an unknown thickness of polyimide above. However, the results showed that the thickness of the polyimide layer is homogenous above the SVs.

The main energy deposition peak in the spectra from the alpha and proton beam experiments matched well with the MC simulations. The IBICC experiment also showed a homogeneous CCE at the central part of the SVs. The central part of the SVs thus behaves as an ideal cylindrically shaped detector.

The trenched planar microdosimeters has a relatively large area with low sensitivity outside of the trench, which results in low energy events from high LET particles. This was visible in the alpha source and the proton beam experiments. This is due to the missing p-stop layer outside the SVs, and has been corrected in a newer design of the microdosimeter (James et al., 2020). The p-stop layer in the new design is also connected to the P^+ doping at the trenches which removes the problem with surface damage seen in the ^{12}C IBICC experiments as the charges under oxide layer is collected by the P^+ trench electrode.

The microdosimeter has a sensitivity gradient near the P^+ trenches of the SV due to the dopant concentration. This results in spectra with an almost constant band of energy depositions with energy from the main peak down to the detection threshold when irradiated by a monoenergetic beam. The volume of the gradient is significant as approximately 44% of events in the SV from a perpendicular incident beam will lose its energy in this gradient.

The novel tissue correction function for protons, $\kappa(\epsilon_{Si})$, gave substantially less error then the previously used correction factor of 0.58 when applied to the measurements in the low energy proton beam experiment. In future work, the tissue correction function should be tested in simulation environment for higher proton energies and compared to the conventional 0.58 correction factor to see if it would lower the errors also for beamlines with therapeutic energies as well. A new correction function should also be explored for heavier ions where the secondary ions are more varied.

In the low energy proton beam experiment at OCL the measured and simulated microdosimetric spectra matched very well, both at the BP and DDF, with less than 2% deviation in $\overline{y_D}$. The measured spectra prior the BP and the depth dose distributions indicated that the experiment could have had a larger fraction of low energy protons than were simulated. The clear change in microdosimetric spectra for each layer of 19 μm WET demonstrate the microdosimeters' excellent spatial resolution along the depth of the beam. By simulating a microdosimeter with smaller SVs it was demonstrated that the lineal energy depends heavily on the SV size, especially in the DDF.

If the characteristics of the low energy regions and gradients at the trenches is accurately incorporated in a new version of the MC model, the microdosimeter can be an excellent tool for benchmarking MC simulations. The benchmarked simulations can then be used to simulate microdosimetric spectra in sites with a variety of shapes and sizes.

Smaller SVs should also be investigated where a small group or single SVs situated close to the readout electronics through wire or bump bonding, or through a monolithic design. This can achieve very good SNR even in small volumes such that low LET events are detectable in small volumes. This would also increase the spatial resolution and the ability to handle even higher beam intensities.

A tracking sandwich microdosimeter using a stack of MAPS detectors was presented and discussed. The current ALPIDE detector is likely to coarse, especially in the depth direction due to its thickness and the necessity for a TE material between detector layers. However, the rapid development in CMOS imaging technology might make this a promising concept in the not too far future. The concept should also be further explored from a radiobiological standpoint and a MC model should be created to investigate the necessary specifications.

References

Aglieri Rinella, G. (2017). The ALPIDE pixel sensor chip for the upgrade of the ALICE Inner Tracking System. *Nuclear Instruments and Methods in Physics Research Section A: Accelerators, Spectrometers, Detectors and Associated Equipment, 845*, 583-587. doi:10.1016/j.nima.2016.05.016

Agosteo, S., Cirrone, G. A. P., Colautti, P., Cuttone, G., D'Angelo, G., Fazzi, A., . . . Varoli, V. (2010). Study of a silicon telescope for solid state microdosimetry: Preliminary measurements at the therapeutic proton beam line of CATANA. *Radiation Measurements, 45*(10), 1284-1289. doi:https://doi.org/10.1016/j.radmeas.2010.06.051

Agosteo, S., Fallica, P. G., Fazzi, A., Introini, M. V., Pola, A., & Valvo, G. (2008). A pixelated silicon telescope for solid state microdosimetry. *Radiation Measurements, 43*(2), 585-589. doi:https://doi.org/10.1016/j.radmeas.2007.12.053

Agosteo, S., Fazzi, A., D'Angelo, G., Introini, M. V., Pola, A., Pirovano, C., & Varoli, V. (2009). Study of a Solid-State Microdosimeter Based on Micrometric-Size Diodes Coupled to a Residual Energy Measurement Stage. *Nuclear Technology, 168*(1), 185-190. doi:10.13182/NT09-A9123

Barendsen, G. W., Walter, H. M. D., Fowler, J. F., & Bewley, D. K. (1963). Effects of Different Ionizing Radiations on Human Cells in Tissue Culture: III. Experiments with Cyclotron-Accelerated Alpha-Particles and Deuterons. *Radiation Research, 18*(1), 106-119. doi:10.2307/3571430

Berger, M. J., Coursey, J. S., Zucker, M. A., & Chang, J. (2017). Stopping-Power & Range Tables for Electrons, Protons, and Helium Ions. Retrieved from https://www.nist.gov/pml/stopping-power-range-tables-electrons-protons-and-helium-ions

Bolst, D., Guatelli, S., Tran, L. T., Chartier, L., Lerch, M. L., Matsufuji, N., & Rosenfeld, A. B. (2017). Correction factors to convert microdosimetry measurements in silicon to tissue in (12)C ion therapy. *Phys Med Biol, 62*(6), 2055-2069. doi:10.1088/1361-6560/aa5de5

Bolst, D., Tran, L. T., Chartier, L., Prokopovich, D. A., Pogossov, A., Guatelli, S., . . . Rosenfeld, A. B. (2017). RBE study using solid state microdosimetry in heavy ion therapy. *Radiation Measurements, 106*, 512-518. doi:https://doi.org/10.1016/j.radmeas.2017.02.008

Bradley, P. D. (2000). *The Development of a Novel Silicon Microdosimeter for High LET Radiation Therapy.* (PhD thesis). University of Wollongong,

Bradley, P. D., & Rosenfeld, A. B. (1998). Tissue equivalence correction for silicon microdosimetry detectors in boron neutron capture therapy. *Medical Physics, 25*(11), 2220-2225. doi:10.1118/1.598421

Brenner, D. J. (2008). The Linear-Quadratic Model Is an Appropriate Methodology for Determining Isoeffective Doses at Large Doses Per Fraction. *Seminars in Radiation Oncology, 18*(4), 234-239. doi:https://doi.org/10.1016/j.semradonc.2008.04.004

Conte, V., Bianchi, A., Selva, A., Petringa, G., Cirrone, G. A. P., Parisi, A., . . . Colautti, P. (2019). Microdosimetry at the CATANA 62 MeV proton beam with a sealed miniaturized TEPC. *Physica Medica, 64*, 114-122. doi:https://doi.org/10.1016/j.ejmp.2019.06.011

Dahle, T. J., Rykkelid, A. M., Stokkevåg, C. H., Mairani, A., Görgen, A., Edin, N. J., . . . Ytre-Hauge, K. S. (2017). Monte Carlo simulations of a low energy proton beamline for radiobiological experiments. *Acta Oncologica, 56*(6), 779-786. doi:10.1080/0284186X.2017.1289239

De Nardo, L., Cesari, V., Donà, G., Magrin, G., Colautti, P., Conte, V., & Tornielli, G. (2004). Mini-TEPCs for radiation therapy. *Radiation Protection Dosimetry, 108*(4), 345-352. doi:10.1093/rpd/nch023

De Nardo, L., Moro, D., Colautti, P., Conte, V., Tornielli, G., & Cuttone, G. (2004). Microdosimetric investigation at the therapeutic proton beam facility of CATANA. *Radiation Protection Dosimetry, 110*(1-4), 681-686. doi:10.1093/rpd/nch111

Debrot, E., Tran, L., Chartier, L., Bolst, D., Guatelli, S., Vandevoorde, C., . . . Rosenfeld, A. B. (2018). SOI microdosimetry and modified MKM for evaluation of relative biological effectiveness for a passive proton therapy radiation field. *Physics in Medicine & Biology, 63*(23), 235007. Retrieved from http://stacks.iop.org/0031-9155/63/i=23/a=235007

Elsässer, T., Weyrather, W. K., Friedrich, T., Durante, M., Iancu, G., Krämer, M., . . . Scholz, M. (2010). Quantification of the Relative Biological Effectiveness for Ion Beam Radiotherapy: Direct Experimental Comparison of Proton and Carbon Ion Beams and a Novel Approach for Treatment Planning. *International Journal of Radiation Oncology*Biology*Physics, 78*(4), 1177-1183. doi:https://doi.org/10.1016/j.ijrobp.2010.05.014

Garcia-Sciveres, M., & Wermes, N. (2018). A review of advances in pixel detectors for experiments with high rate and radiation. *Reports on Progress in Physics, 81*(6), 066101. doi:10.1088/1361-6633/aab064

Geant4. (2020). Retrieved from https://geant4.web.cern.ch/

Gillmann, C., Jäkel, O., & Karger, C. P. (2019). RBE-weighted doses in target volumes of chordoma and chondrosarcoma patients treated with carbon ion radiotherapy: Comparison of local effect models I and IV. *Radiotherapy and Oncology, 141*, 234-238. doi:https://doi.org/10.1016/j.radonc.2019.08.006

Goodhead, D. T. (2007). Energy deposition stochastics and track structure: what about the target? *Radiation Protection Dosimetry, 122*(1-4), 3-15. doi:10.1093/rpd/ncl498

Goodhead, D. T., Thacker, J., Cox, R., & Wilkinson, R. E. (1979). Effectiveness of 0·3 keV Carbon Ultrasoft X-rays for the Inactivation and Mutation of Cultured Mammalian Cells. *International Journal of Radiation Biology and Related Studies in Physics, Chemistry and Medicine, 36*(2), 101-115. doi:10.1080/09553007914550861

Gray, P. R., Hurst, P. J., Lewis, S. H., & Meyer, R. G. (2009). *Analysis and design of analog in integrated circuits* John Wiley & Sons.

Hawkins, R. B. (1994). A Statistical Theory of Cell Killing by Radiation of Varying Linear Energy Transfer. *Radiation Research, 140*(3), 366-374. doi:10.2307/3579114

Hawkins, R. B. (1996). A microdosimetric-kinetic model of cell death from exposure to ionizing radiation of any LET, with experimental and clinical applications. *International Journal of Radiation Biology, 69*(6), 739-755. doi:10.1080/095530096145481

Hawkins, R. B. (1998). A microdosimetric-kinetic theory of the dependence of the RBE for cell death on LET. *Medical Physics, 25*(7), 1157-1170. doi:10.1118/1.598307

Hawkins, R. B. (2003). A Microdosimetric-Kinetic Model for the Effect of Non-Poisson Distribution of Lethal Lesions on the Variation of RBE with LET. *Radiation Research, 160*(1), 61-69, 69. Retrieved from https://doi.org/10.1667/RR3010

Hawkins, R. B. (2006). Mammalian Cell Killing by Ultrasoft X Rays and High-Energy Radiation: An Extension of the MK Model. *Radiation Research, 166*(2), 431-442, 412. Retrieved from https://doi.org/10.1667/RR3594.1

Hubbell, J. H., & Seltzer, S. M. (2004). Tables of X-Ray Mass Attenuation Coefficients and Mass Energy-Absorption Coefficients (version 1.4). Retrieved from https://www.nist.gov/pml/x-ray-mass-attenuation-coefficients

Huiberts, S. (2018). *Characterization of the ALPIDE chip with Helium-4 ions for Proton Computed Tomography.* (Master thesis). University of Bergen, Retrieved from http://bora.uib.no/handle/1956/18748

IAEA. (1995). *Atomic and Molecular Data for Radiotherapy and Radiation Research*. Vienna: INTERNATIONAL ATOMIC ENERGY AGENCY.

IAEA. (2005). *Radiation Oncology Physics*. Vienna: INTERNATIONAL ATOMIC ENERGY AGENCY.

IAEA. (2008). *Relative Biological Effectiveness in Ion Beam Therapy*. Vienna: INTERNATIONAL ATOMIC ENERGY AGENCY.

IAEA. (2010). *Implementation of the International Code of Practice on Dosimetry in Radiotherapy (TRS 398): Review of Testing Results*. Vienna: INTERNATIONAL ATOMIC ENERGY AGENCY.

ICRU. (1970). Linear Energy Transfer. In *Report 16*: International Commission on Radiation Units and Measurements.

ICRU. (1983). Microdosimetry. In *Report 36*: International Commission in Radiation Units and Measurements.

ICRU. (1989). Tissue Substitutes in Radiation Dosimetry and Measurement. In *Report 44*: International Commission in Radiation Units and Measurements.

Inaniwa, T., Kanematsu, N., Matsufuji, N., Kanai, T., Shirai, T., Noda, K., . . . Tsujii, H. (2015). Reformulation of a clinical-dose system for carbon-ion radiotherapy treatment planning at the National Institute of Radiological Sciences, Japan. *Physics in medicine and biology, 60*(8), 3271-3286. doi:10.1088/0031-9155/60/8/3271

James, B., Tran, L. T., Bolst, D., Peracchi, S., Davis, J. A., Prokopovich, D. A., . . . Rosenfeld, A. B. (2020). SOI Thin Microdosimeters for High LET Single-Event Upset Studies in Fe, O, Xe, and Cocktail Ion Beam Fields. *Ieee*

Transactions on Nuclear Science, 67(1), 146-153. doi:10.1109/TNS.2019.2939355

James, B., Tran, L. T., Vohradsky, J., Bolst, D., Pan, V., Carr, M., . . . Rosenfeld, A. B. (2018). SOI Thin Microdosimeter Detectors for Low Energy Ions and Radiation Damage Studies. *Ieee Transactions on Nuclear Science*, 1-1. doi:10.1109/TNS.2018.2885996

Jan, S., Benoit, D., Becheva, E., Carlier, T., Cassol, F., Descourt, P., . . . Buvat, I. (2011). GATE V6: a major enhancement of the GATE simulation platform enabling modelling of CT and radiotherapy. *Physics in medicine and biology, 56*(4), 881-901. doi:10.1088/0031-9155/56/4/001

Jan, S., Santin, G., Strul, D., Staelens, S., Assié, K., Autret, D., . . . Morel, C. (2004). GATE: a simulation toolkit for PET and SPECT. *Physics in medicine and biology, 49*(19), 4543-4561. doi:10.1088/0031-9155/49/19/007

Kase, Y., Kanai, T., Matsumoto, Y., Furusawa, Y., Okamoto, H., Asaba, T., . . . Shinoda, H. (2006). Microdosimetric Measurements and Estimation of Human Cell Survival for Heavy-Ion Beams. *Radiation Research, 166*(4), 629-638, 610. Retrieved from https://doi.org/10.1667/RR0536.1

Kellerer, A. M. (1971). Considerations on the Random Traversal of Convex Bodies and Solutions for General Cylinders. *Radiation Research, 47*(2), 359-376. doi:10.2307/3573243

Kellerer, A. M. (1981). Criteria for the Equivalence of Spherical and Cylindrical Proportional Counters in Microdosimetry. *Radiation Research, 86*(2), 277-286. doi:10.2307/3575505

Kellerer, A. M. (1985). *Fundamentals of Microdosimetry*: ACADEMI C PRESS , INC.

Kellerer, A. M., & Rossi, H. H. (1972). The theory of dual radiation action. *Current Topics in Radiation Research Quarterly*, 85-158.

Kenney, C. J., Parker, S. I., Peterson, V. Z., Snoeys, W. J., Plummer, J. D., & Chye Huat, A. (1994). A prototype monolithic pixel detector. *Nuclear Instruments and Methods in Physics Research Section A: Accelerators, Spectrometers, Detectors and Associated Equipment, 342*(1), 59-77. doi:https://doi.org/10.1016/0168-9002(94)91411-7

Kenney, C. J., Segal, J. D., Westbrook, E., Parker, S., Hasi, J., Da Via, C., . . . Morse, J. (2006). Active-edge planar radiation sensors. *Nuclear Instruments and Methods in Physics Research Section A: Accelerators, Spectrometers, Detectors and Associated Equipment, 565*(1), 272-277. doi:https://doi.org/10.1016/j.nima.2006.05.012

Kim, D., Rinella, G. A., Cavicchioli, C., Chanlek, N., Collu, A., Degerli, Y., . . . Yang, P. (2016). Front end optimization for the monolithic active pixel sensor of the ALICE Inner Tracking System upgrade. *Journal of Instrumentation, 11*(02), C02042-C02042. doi:10.1088/1748-0221/11/02/c02042

Klein, C. A. (1968). Bandgap Dependence and Related Features of Radiation Ionization Energies in Semiconductors. *Journal of Applied Physics, 39*(4), 2029-2038. doi:10.1063/1.1656484

Knoll, G. F. (2010). *Radiation detection and measurement*: John Wiley & Sons.

Kok, A., Hansen, T., Hansen, T., Jensen, G. U., Lietaer, N., Mielnik, M., & Storås, P. (2009, 24 Oct.-1 Nov. 2009). *High aspect ratio deep RIE for novel 3D radiation sensors in high energy physics applications.* Paper presented at the 2009 IEEE Nuclear Science Symposium Conference Record (NSS/MIC).

Lai, N. S., Lim, W. H., Ziebell, A. L., Reinhard, M. I., Rosenfeld, A. B., & Dzurak, A. S. (2008, 19-25 Oct. 2008). *Development and fabrication of cylindrical silicon-on-insulator microdosimeter arrays.* Paper presented at the 2008 IEEE Nuclear Science Symposium Conference Record.

Leo, W. R. (1994). *Techniques for nuclear and particle physics experiments: a how-to approach* (2 ed.): Springer Science & Business Media.

Liamsuwan, T., Hultqvist, M., Lindborg, L., Uehara, S., & Nikjoo, H. (2014). Microdosimetry of proton and carbon ions. *Medical Physics, 41*(8Part1), 081721. doi:10.1118/1.4888338

Liamsuwan, T., Uehara, S., Emfietzoglou, D., & Nikjoo, H. (2011). Physical and biophysical properties of proton tracks of energies 1 keV to 300 MeV in water. *International Journal of Radiation Biology, 87*(2), 141-160. doi:10.3109/09553002.2010.518204

Lindborg, L., & Waker, A. (2017). *Microdosimetry: Experimental Methods and Applications*: CRC Press.

Lindström, G. (2003). Radiation damage in silicon detectors. *Nuclear Instruments and Methods in Physics Research Section A: Accelerators, Spectrometers, Detectors and Associated Equipment, 512*(1), 30-43. doi:https://doi.org/10.1016/S0168-9002(03)01874-6

Lye, Ø. (2016). *Characterization of 3D Silicon Microdosimeters and corresponding Readout System.* (Master Thesis). University of Bergen,

M. Kellerer , A. (2002). Microdosimetry: Reflections on Harald Rossi. *Radiation Protection Dosimetry, 99*(1-4), 17-22. doi:10.1093/oxfordjournals.rpd.a006754

Mayles, P., Nahum, A., & Rosenwald, J.-C. (2007). *Handbook of radiotherapy physics*: CRC Press.

Moro, D., Colautti, P., Lollo, M., Esposito, J., Conte, V., De Nardo, L., . . . Ceballos, C. (2009). BNCT dosimetry performed with a mini twin tissue-equivalent proportional counters (TEPC). *Applied Radiation and Isotopes, 67*(7, Supplement), S171-S174. doi:https://doi.org/10.1016/j.apradiso.2009.03.042

Open Gate Collaboration. (2020). Retrieved from http://www.opengatecollaboration.org/

Paganetti, H. (2014). Relative biological effectiveness (RBE) values for proton beam therapy. Variations as a function of biological endpoint, dose, and linear energy transfer. *Physics in medicine and biology, 59*(22), R419-R472. doi:10.1088/0031-9155/59/22/r419

Parker, S. (1989). A proposed VLSI pixel device for particle detection. *Nuclear Instruments and Methods in Physics Research Section A: Accelerators, Spectrometers, Detectors and Associated Equipment, 275*(3), 494-516. doi:https://doi.org/10.1016/0168-9002(89)90736-5

Parker, S. I., Kenney, C. J., & Segal, J. (1997). 3D — A proposed new architecture for solid-state radiation detectors. *Nuclear Instruments and Methods in Physics*

Research Section A: Accelerators, Spectrometers, Detectors and Associated Equipment, 395(3), 328-343. doi:https://doi.org/10.1016/S0168-9002(97)00694-3

Pastuovic, Z., Button, D., Cohen, D., Fink, D., Garton, D., Hotchkis, M., . . . Wilcken, K. (2016). SIRIUS – A new 6MV accelerator system for IBA and AMS at ANSTO. *Nuclear Instruments and Methods in Physics Research Section B: Beam Interactions with Materials and Atoms, 371*, 142-147. doi:https://doi.org/10.1016/j.nimb.2015.09.047

Pastuovic, Z., Siegele, R., Cohen, D. D., Mann, M., Ionescu, M., Button, D., & Long, S. (2017). The new confocal heavy ion microprobe beamline at ANSTO: The first microprobe resolution tests and applications for elemental imaging and analysis. *Nuclear Instruments and Methods in Physics Research Section B: Beam Interactions with Materials and Atoms, 404*, 1-8. doi:https://doi.org/10.1016/j.nimb.2017.01.059

Pettersen, H. E. S. (2018). *A Digital Tracking Calorimeter for Proton Computed Tomography.* (PhD Thesis). University of Bergen, Retrieved from https://bora.uib.no/handle/1956/17757

Pettersen, H. E. S., Alme, J., Barnaföldi, G. G., Barthel, R., van den Brink, A., Chaar, M., . . . Röhrich, D. (2019). Design optimization of a pixel-based range telescope for proton computed tomography. *Physica Medica: European Journal of Medical Physics, 63*, 87-97. doi:10.1016/j.ejmp.2019.05.026

Pettersen, H. E. S., Alme, J., Biegun, A., van den Brink, A., Chaar, M., Fehlker, D., . . . Röhrich, D. (2017). Proton tracking in a high-granularity Digital Tracking Calorimeter for proton CT purposes. *Nuclear Instruments and Methods in Physics Research Section A: Accelerators, Spectrometers, Detectors and Associated Equipment, 860*, 51-61. doi:https://doi.org/10.1016/j.nima.2017.02.007

Rosenfeld, A. B. (2016). Novel detectors for silicon based microdosimetry, their concepts and applications. *Nuclear Instruments and Methods in Physics Research Section A: Accelerators, Spectrometers, Detectors and Associated Equipment, 809*, 156-170. doi:https://doi.org/10.1016/j.nima.2015.08.059

Rossi, H. H., & Rosenzweig, W. (1955). A Device for the Measurement of Dose as a Function of Specific Ionization. *Radiology, 64*(3), 404-411. doi:10.1148/64.3.404

Rossi, H. H., & Zaider, M. (1996). *Microdosimetry and its Applications*: Springer.

Rossi, L., Fischer, P., Rohe, T., & Wermes, N. (2006). *Pixel Detectors*: Springer-Verlag Berlin Heidelberg.

Rossi Tissue Equivalent Proportional Counter (ca. 1960). (2011, 05/10/2011). Retrieved from https://www.orau.org/ptp/collection/proportional%20counters/rossi.htm

Røed, K. (2009). *Single Event Upsets in SRAM FPGA based readout electronics for the Time Projection Chamber in the ALICE experiment.* (PhD Thesis). University of Bergen,

Rørvik, E., Fjæra, L. F., Dahle, T. J., Dale, J. E., Engeseth, G. M., Stokkevåg, C. H., . . . Ytre-Hauge, K. S. (2018). Exploration and application of phenomenological

RBE models for proton therapy. *Physics in Medicine & Biology, 63*(18), 185013. doi:10.1088/1361-6560/aad9db

S5KGH1 - ISOCELL Slim GH1. (2020). Retrieved from https://www.samsung.com/semiconductor/image-sensor/mobile-image-sensor/S5KGH1/

Samnøy, A. T. (2010). *Automated XY-table for the characterisation of arrays of pixel sensors for photons and charged particles.* (Master). University of Bergen,

Schmidt-Böcking, H., Ramm, U., Kraft, G., Ullrich, J., Berg, H., Kelbch, C., . . . Jiazhen, F. (1992). Delta-electron emission in fast heavy ion atom collisions. *Advances in Space Research, 12*(2), 7-15. doi:https://doi.org/10.1016/0273-1177(92)90084-B

Scholz, M., Kellerer, A. M., Kraft-Weyrather, W., & Kraft, G. (1997). Computation of cell survival in heavy ion beams for therapy. *Radiation and Environmental Biophysics, 36*(1), 59-66. doi:10.1007/s004110050055

Scholz, M., & Kraft, G. (1994). Calculation of Heavy Ion Inactivation Probabilities Based on Track Structure, X Ray Sensitivity and Target Size. *Radiation Protection Dosimetry, 52*(1-4), 29-33. doi:10.1093/oxfordjournals.rpd.a082156

Scholz, M., & Kraft, G. (1996). Track structure and the calculation of biological effects of heavy charged particles. *Advances in Space Research, 18*(1), 5-14. doi:https://doi.org/10.1016/0273-1177(95)00784-C

Seibt, W., Sundström, K. E., & Tove, P. A. (1973). Charge collection in silicon detectors for strongly ionizing particles. *Nuclear Instruments and Methods, 113*(3), 317-324. doi:https://doi.org/10.1016/0029-554X(73)90496-5

Seidel, S. (2001). A review of design considerations for the sensor matrix in semiconductor pixel detectors for tracking in particle physics experiments. *Nuclear Instruments and Methods in Physics Research Section A: Accelerators, Spectrometers, Detectors and Associated Equipment, 465*(2), 267-296. doi:https://doi.org/10.1016/S0168-9002(01)00695-7

Sjöstrand, N. G. (2002). What is the average chord length? *Annals of Nuclear Energy, 29*(13), 1607-1608. doi:https://doi.org/10.1016/S0306-4549(02)00003-8

Spieler, H. (2005). *Semiconductor Detector Systems*: Oxford University Press.

Strulab, D., Santin, G., Lazaro, D., Breton, V., & Morel, C. (2003). GATE (geant4 application for tomographic emission): a PET/SPECT general-purpose simulation platform. *Nuclear Physics B - Proceedings Supplements, 125*, 75-79. doi:https://doi.org/10.1016/S0920-5632(03)90969-8

Šuljić, M. (2016). ALPIDE: the Monolithic Active Pixel Sensor for the ALICE ITS upgrade. *Journal of Instrumentation, 11*(11), C11025-C11025. doi:10.1088/1748-0221/11/11/c11025

Tambave, G., Alme, J., Barnaföldi, G. G., Barthel, R., van den Brink, A., Brons, S., . . . Yang, S. (2019). Characterization of monolithic CMOS pixel sensor chip with ion beams for application in particle computed tomography. *Nuclear Instruments and Methods in Physics Research Section A: Accelerators, Spectrometers, Detectors and Associated Equipment*, 162626. doi:https://doi.org/10.1016/j.nima.2019.162626

Thompson, A., Attwood, D., Gullikson, E., Howells, M., Kim, K.-J., Kirz, J., . . . Winick, H. (2009). *X-ray data booklet* (3 ed.): Lawrence Berkeley National Laboratory, University of California Berkeley, CA.

Tran, L. T., Bolst, D., Guatelli, S., Pogossov, A., Petasecca, M., Lerch, M. L. F., . . . Rosenfeld, A. B. (2018). The relative biological effectiveness for carbon, nitrogen, and oxygen ion beams using passive and scanning techniques evaluated with fully 3D silicon microdosimeters. *Medical Physics, 45*(5), 2299-2308. doi:doi:10.1002/mp.12874

Tran, L. T., Chartier, L., Bolst, D., Davis, J., Prokopovich, D. A., Pogossov, A., . . . Rosenfeld, A. B. (2018). In-field and out-of-file application in 12C ion therapy using fully 3D silicon microdosimeters. *Radiation Measurements, 115*, 55-59. doi:https://doi.org/10.1016/j.radmeas.2018.06.015

Tran, L. T., Chartier, L., Bolst, D., Pogossov, A., Guatelli, S., Petasecca, M., . . . Rosenfeld, A. B. (2017). Characterization of proton pencil beam scanning and passive beam using a high spatial resolution solid-state microdosimeter. *Medical Physics, 44*(11), 6085-6095. doi:doi:10.1002/mp.12563

Tran, L. T., Chartier, L., Prokopovich, D. A., Bolst, D., Povoli, M., Summanwar, A., . . . Rosenfeld, A. B. (2018). Thin Silicon Microdosimeter Utilizing 3-D MEMS Fabrication Technology: Charge Collection Study and Its Application in Mixed Radiation Fields. *Ieee Transactions on Nuclear Science, 65*(1), 467-472. doi:10.1109/TNS.2017.2768062

Tran, L. T., Chartier, L., Prokopovich, D. A., Reinhard, M. I., Petasecca, M., Guatelli, S., . . . Rosenfeld, A. B. (2015). 3D-Mesa "Bridge" Silicon Microdosimeter: Charge Collection Study and Application to RBE Studies in C-12 Radiation Therapy. *Ieee Transactions on Nuclear Science, 62*(2), 504-511. doi:10.1109/TNS.2015.2391102

Usai, G. (2019). NA60+ status report.

Valin, I., Hu-Guo, C., Baudot, J., Bertolone, G., Besson, A., Colledani, C., . . . Winter, M. (2012). A reticle size CMOS pixel sensor dedicated to the STAR HFT. *Journal of Instrumentation, 7*(01), C01102-C01102. doi:10.1088/1748-0221/7/01/c01102

Appendix A

The illustrations in Figure A-1 shows five different events, where a primary ion track is coloured blue, and the delta electron tracks are red. The three dots represent the collection nodes in a monolithic pixel detector and the square around them represents the region where only a single pixel will fire when a track crosses within the square. If a track passes between the squares, the liberated charge will be shared between the neighbouring nodes, and both pixels will fire, even with applied bias voltage. In event a) and b) no delta electrons are produced but only pixel 1 fires in a), while 1 & 2 fires in event b).

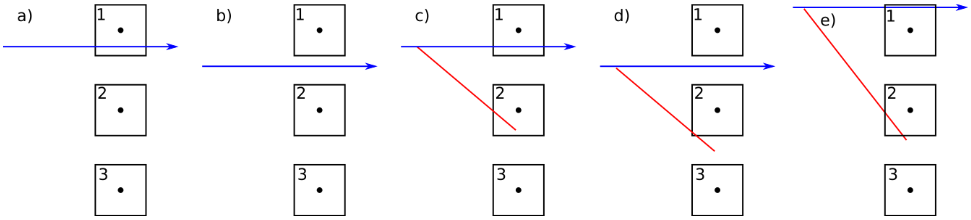

Figure A-1: Sketch of five different events, where a primary ion track (blue) and a delta electron tracks (red) are crossing the ALPIDE. The three dots represent the collection nodes in the ALPIDE detector, and the squares encompassing them represents the region where only a single pixel will be fired when a track crosses within the square. If a track passes between the squares, the liberated charge will be shared between the two nodes, and both pixels will fire, even at high bias voltage.

In event c) a delta electron is produced with transverse path length similar to a pixel pitch, but the result is indistinguishable from event b). In event d) the delta electron has the same track as in c), but as its initial position is different, this event fires all three pixels. Event e) also fires all three pixels but needs a much longer transvers path length to do so. Thus, to know if a secondary is present, at least three pixels along a line (not cluster shaped) needs to fire, and the transverse path length of the secondary must be about 1-2 pixel pitch distances.

Even though the presence of a delta electron is established when three pixels in a line fire, four pixels in a line is necessary to establish the direction of the secondary. In Figure A-2 two events show three pixels in a row firing, but the delta electron has opposite transverse direction. Thus, the secondary's transverse path must extend at least three pixels away from the primary track to know its direction, or more than about 50 µm in silicon for the current ALPIDE detector.

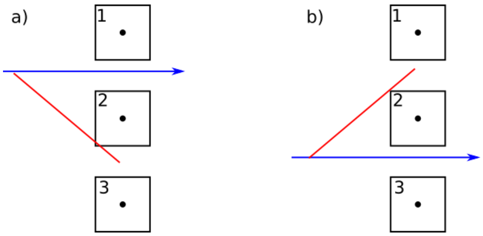

Figure A-2: Two events where a primary and a secondary fires the same three pixels, but the secondary has different directions.

Graphic design: Communication Division, UiB / Print: Skipnes Kommunikasjon AS

uib.no

ISBN: 9788230849774 (print)
9788230844090 (PDF)